University of Puerto Rico

Río Piedras Campus

Faculty of Natural Sciences

Department of Chemistry

Biologically Relevant Formulation and Expansion of Responsive Properties of Guanine Based Supramolecular Particles

By

Maxier Acosta-Santiago

A Thesis Presented and Submitted to the Department of Chemistry in Partial Fulfillment of the Requirement for the Degree of Doctor of Philosophy

January 2021

"This doctoral thesis has been examined by the student committee and accepted by the Department of Chemistry from the University of Puerto Rico".

José M. Rivera, Ph.D.

Thesis Advisor

Liz Díaz, Ph.D.

Interim Chairman

Department of Chemistry

January 2021

Mom, Thank you.

Acknowledgments

As I started my academic career, I was not sure what I wanted. As I battled with my own identity, I found my passion for research. My mental health and passion for science would not have been able to pursue if it were not for the people and staff surrounding me. So, I need to thank them all.

First, I want to thank my mother. Yolanda Santiago Ayala has been my number one cheerleader since day one. I have been a fortunate privileged person to be her son. Because of her, I have been able to progress as an adult and keep doing what I love. So thank you.

During this journey, I have been able to grow and keep my sanity. A big reason for this has been thanks to my siblings Zahíra Rodriguez Feliciano and Dr. Sergio A. Loza Rosas. Thank you for keeping me grounded through this process. Very few people have seen me in my worst, and you two have. Thank you for always picking me up every single time and being by my side no matter what.

In Dr. José M. Rivera's laboratory, I became part of an ongoing family where I grew as a scientist. For that reason, I want to thank my graduate colleagues and mentors for waking up my real life's passion. I want to thank Luis Prieto Costas, María del Carmen Rivera, Dr. Luxene Belfleur, Dr. Luis M. Negron, and Dr. Marilyn García. All of you have been essential for my bench training, idea development, and tantrum support system. I could not have been my true self in any other place. So thank you for letting me be, accepting me, and helping me grow. A lot of my work would not have been able without the support of many undergrads. For this, I want to thank Minelise Rivera De Jesus. Thanks to you, I became a better mentor, and in the process, we became friends. Thank you for letting me be your mentor. I also need to thank Diomedes Dieppa, whose support kickstarted the project when I was still starting graduate school. Other undergraduate colleagues as José Manuel Martínez Montes, Adriana Claudio, Andrea Maser, and Xavier Marrero for helping me expand these projects.

I want to thank Dr. José M. Rivera, my mentor and my advisor, for everything you did for me. Thank you for believing in me and for giving me the chance to become a scientist. Thank you for seeing the potential in me, putting me in line, and nourish my curiosity. Thanks to you, I am the scientist that I am today.

I need to thank my thesis committee, Dr. Athur Tinoco, Dr. Marvin Bayro, Dr. Nestor Carballeira, and Dr. Vilmalí López, for being honest and giving me constructive critiques. I need to thank Dr. Athur Tinoco for continually following up on my projects and becoming a close mentor and friend. I want to thanks José Martinez, José Hernandez, and Marvin Bayro for their assistance and support in the NMR facilities. I want to thank Lopez-Stelzer's lab for the immense and extensive support in using your UV-Vis spectrophotometer. I want to thank Bismark Madera for the confocal imaging facilities support of our projects. I also want to thank the RISE Program (5R25GM061151) for funding our projects and other financial aid.

I need to apologize because I am sure there are a lot of missing people in these acknowledgments. This has been a long and rough journey. Thank you all.

Biographical Sketch

Maxier Acosta-Santiago was born in San Juan, Puerto Rico, on October 31st, 1989. After graduating from Saint Francis School's high school in 2007, he decided to pursue a medical career. Yet he found his true passion for chemistry while researching at the University of Puerto Rico, Rio Piedras Campus, on the José M. Rivera research group. After achieving his bachelor's degree in chemistry in 2013, he decided to earn his Ph.D. He joined the chemistry graduate program in august 2013 but was not until after a tumultuous first two years of graduate school that he classified as a Ph.D. student. There he was able to grow as a scientist with his mentor José M. Rivera and his team of welcoming and nourishing students as Luis Prieto and Maria Rivera. As he followed his passion, he grew as a scientist and became a mentor. In November 2020, he completed his Ph.D. by expanding the fundamental knowledge of supramolecular chemistry and its applications.

Abstract

Colloidal particles ranging from the nano to the microscale show great promise in the delivery and enhancement of therapeutic agents. The formulation of many of these particles usually includes crosslinkers, non-biocompatible solvents, or lengthy procedures that are not cost-effective. We have developed particles termed Supramolecular Hacky Sacks (SHS) via thermo-responsive Supramolecular G-quadruplexes (SGQs) with lower critical solution temperature (LCST). SGQs are formed by the self-assembly of G-derivatives. SHS particles have served as HIV-1 vaccine adjuvants and encapsulate small molecules, proteins, and plasmid DNA. Here we are showing multiple strategies taken to expand the SHS particles' properties with the ultimate goal of making them suitable for more biocompatible environments. In chapter 2, we showcase the use of potassium thiocyanate to enhance the solubility of various G-derivatives, which enables modulation of the LCST phenomenon of the corresponding SGQ structures. We also highlight the role of such salt in the corresponding upper critical solution temperature (UCST). In chapter 3, we demonstrate the use of the thiol-Michael reaction between a G-derivative having an α,β-unsaturated enone with biothiols like cysteine and glutathione as a viable strategy to modulate the formation of the SGQs and the corresponding SHS particles. Furthermore, the addition of biothiols to SHS triggered the controlled release of encapsulated Rhodamine B. This provided proof of concept for longer term drug-delivery applications. Chapter 4 demonstrates the use of an alternative strategy to achieve an analogous responsive behavior towards cysteine. In chapter 4 we explored the

reaction of a formyl-containing G-derivative with cysteine to form a thiazolidine-carboxylate moiety. The thiazolidine-carboxylate enhanced hydrophilicity and greater steric bulk. The enhanced properties induced the disassembly of the SHS particles. Encapsulation and release studies using Rhodamine B showed similar behavior described in chapter 3, but with different kinetic and thermodynamic parameters. We expect these relatively simple strategies to enable the development of sophisticated supramolecular based particles for biomedical applications.

List of Abbreviations

%T: Percent Transmittance
^{13}C NMR: Carbon nuclear magnetic resonance
^{1}H NMR: Proton nuclear magnetic resonance
8ArG: 8-Aryl-2'-deoxyguanosine derivative
Cys: L-cysteine
dG: 2'-deoxyguanosine
DCR: Derived Count Rate
D_H: Hydrodynamic diameter.
DLS: Dynamic Light Scattering
DMSO-*d6*: Dimethyl sulfoxide-d6, deuterated
DNA: Deoxyribonucleic acid
DSC: Differential Scanning Calorimetry
eq, equiv: Equivalents
ESI MS: Electrospray ionization mass spectra
EtOH: Ethanol
f-SHS: fixed-Supramolecular Hacky Sacks
GSH: Glutathione
HCy: Homocysteine
IR: Infrared
K: Kelvil
kcps: kilo counts per second
$[KSCN]_{min}$: the minimum amount of KSCN needed for the dG to solubilize.
LCST: Lower Critical Solution Temperature
LSCM: Laser Scanning Confocal Microscopy
M: Molar
ME: Mercaptoethanol
MeOH: Methanol
MHz: Megahertz
Min: Minutes
mM: milimilar

m/z: Mass to charge ratio

MSRC: Molecular Sciences Research Center

NIEF: Neuroimaging and Electrophysiology Facility

NMR: Nuclear magnetic resonance

nm: Nanometer

PBS: Phosphate buffer solution

ppm: Parts per million

RhoB: Rhodamine B

f-SHS-dG@RhoB: dG derivative based fixed-Supramolecular Hacky Sacks encapsulating Rhodamine B

SGQ: Supramolecular Guanine Quadruplex

SGQ-dG: Supramolecular Guanine Quadruplex based on a specific dG derivative

SHS: Supramolecular Hacky Sacks

SHS-dG: Supramolecular Hacky Sacksbased on a specific dG derivative

$t_{1/2}$: Half-time

T_{cp}: Clouding temperature, taken at the lowest transmittance seen at the minimum

TLC: Thin layer chromatography

T_{LCST}: taken from the inflection point of turbidity.

UCST: upper critical solution temperature

UV-Vis: Ultraviolet-Visible

µm: Micrometer

List of Tables

List of Images

Table of Contents

Chapter 1. Introduction

To begin exploring the world of particles and how it works for biologically relevant applications, we need to understand their composition and how these are organized. So far, there have been reported particles made from silica, silver, gold, small molecules, lipids, polymers made from simple organic molecules to other complex entities such as amino acids or oligonucleotide chains.[1–3] These are mainly studied depending on composition, stability, size, morphology, charge, among other properties, to determine their specific application.[4,5] To look into their applications, a vast amount of effort has been focused on developing novel materials.

1.1. Self-assembly and supramolecular chemistry: Supramolecular Hacky Sacks building blocks

A large number of particles use elements of supramolecular chemistry.[6] Supramolecular chemistry studies how covalently built molecules organize via electrostatic interactions and how these work as a completely new single entity.[7] Supramolecular systems, or supramolecules, have been studied for over two centuries because of their complexity in nature.[7] Nature has taken advantage of non-covalent interactions such as H-bonds, hydrophobicity, van der Waals forces, and metal-ligand coordination to build complex yet efficient systems.[7,8] These natural systems range from proteins, enzymes, DNA, complete cellular organelles to viruses.[9] So, it is no surprise that scientists have tried to replicate elements of supramolecular system assembly to engineer novel tools and diverse particles.

The process which predominates the assembly of supramolecules is self-assembly.[7]

Self-assembly itself is the spontaneous process by which monomeric subunits form ordered supramolecular aggregates. Self-assembly allows scientists to encode information on each subunit to recognize each other, so the final structure builds by itself. At a molecular level, the information encoded on the subunit molecule entails H-bond donors or acceptors, hydrophobic areas, charges, among others. This process exists in a thermodynamic equilibrium where repulsive and attractive interactions balance out. So far, self-assembly has been used to form structures such as cubes, cages, spheres, shells, planar structures, rods, and tubular structures.[10] Yet as the process is reversible, it allows designing particles by simple changes in the self-assembling subunits.[9]

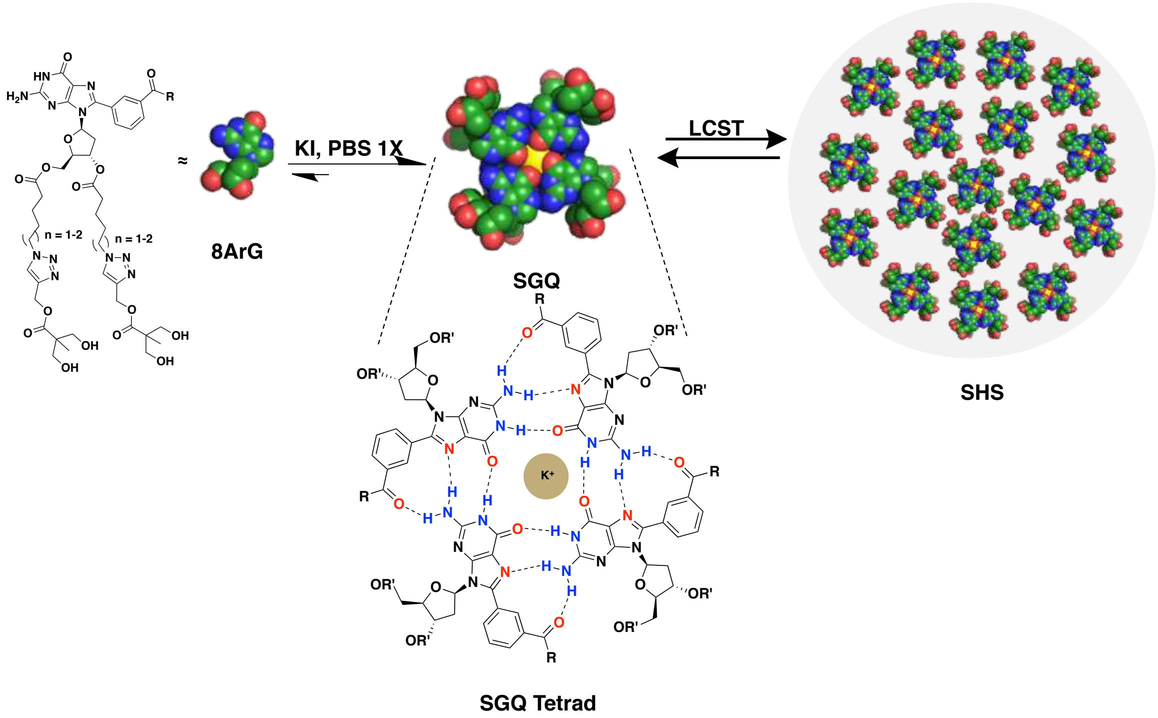

Figure 1.1. Schematic representation of the self-assembly of G-derivatives into SGQs and SHS particles. SGQ tetrad identifies N1H and NH_2 as H-bond donors (blue) and the Hoogsteen edge H-bond acceptors (red).

Supramolecular guanine quadruplexes (SGQ) are some of the structures emulating nature. These are based on DNA G-quadruplex (G4-DNA) structures found throughout the genome of all organisms ranging from bacteria to humans, where G4-DNA is prominent in chromosome regions like the telomeres. SGQ are developed without the DNA backbone and has been studied for DNA stabilization and the development of self-assembled gels and anti-cancer treatments.[11,12] Researchers have developed these by taking advantage of the guanosine self-assembly via H-bond.

SGQs take into consideration the said G assembly motif. As the Hoogsteen edge provides H-bonding acceptors, the Watson-Crick edge provides its H-bonding donors forming tetrameric structures.[12] These tetrads can stack via $\pi - \pi$

interactions with the help of a cation between these. The acetyl groups at the Hoogsteen edge of the nucleobase are directed into the tetrad center (Figure 1.1). This conformation creates high electron density in the center of the tetrad. Cations such as K^+ interact within the SGQs by locating themselves between two tetrads in the center region. These attractive interactions lock the tetrads in position (Figure 1.1).[12] Our research group has been able to extend the Hoogsteen edge, resulting in the formation of precise SGQs of specific molecularities (e.g., number of subunits), the most common of which are octamers followed by hexadecamers, and less commonly dodecamers.[13,14] Intrinsic (e.g., structural) modifications to G-derivatives like attachments of different aryl groups at the guanine's C8 enable their self-assembly into these discrete and precise structures. Many of the most stable systems contain a *meta*-carbonyl moiety, which provides an additional H-bond acceptor to the NH_2 group of adjacent G-subunits (Figure 1.1).[14] These initial studies of precise SGQ structures were developed in organic media in the presence of potassium iodide, and opened the door to similar studies in aqueous media.[15]

As the Rivera research team achieved stable SGQs in water, it was discovered that these had a thermal response. SGQs are formed via a salting-in manner in the presence of potassium at low temperatures of 2 °C. Yet as the solution temperatures are increased, these SGQs show thermal sensitivity.[16] This behavior was achieved by the esterification of the 3'' and 5'' hydroxyl groups. These esters include a 4 - 5 hydrocarbon chain with hydroxyl groups containing dendrons. When the SGQ is in solution, the hydroxyl groups interaction with water is aided with the already chaotropic iodide, which serves as an interactive bridge between hydrophobic fractions and water. As the temperature is increased these SGQs form particles termed Supramolecular Hacky Sacks (SHS). This thermal behavior is termed lower critical solution temperature (LCST).[17] These SHS particles have been shown to serve as flexible cargo encapsulators. These have been able to encapsulate small molecules, proteins, and plasmid DNA.[18] These meso globular particles have also been used for vaccine adjuvants.[19]

1.2. Goals

The long-term goal of our project is to develop functional biocompatible particles for immune system modulation applications. Yet biological systems provide very specific constraints, and studies of the immune system have shown to be sensitive to seemingly minor changes.[20–23] For these reasons, we are fine-tuning the development of the SHS particles and expanding its responsive properties. The further modifications of the SHS particles can be achieved by adjusting intrinsic and extrinsic parameters.

Our research team has modulated the SGQ's LCST by intrinsic changes on the guanosine derivative. By modulating the G-derivative intrinsic changes, we can generate hydrophobic patches in the supramolecular structures. These patches affect its hydrophilic-hydrophobic balance in solution.[18] Moreover, previously published data have shown the introduction of Hofmeister anion series.[16] Here we will be exploring a more detailed approach to understand how the Hofmeister anion thiocyanate affects a library of G-derivatives supramolecular structures. As we explored the fundamental understandings of a library of SGQ and SHS, we looked into more detail on some with biological relevant thiol responsive potential. As biothiols as L-cysteine (Cys), homocysteine (HCy), or glutathione (GSH) play roles in varying biomedical afflictions, these have been the subject of interest by researchers working on responsive materials.[24–28]

1.3. Responsive properties for the development of particles.

Particles have been developed to be used in environmental chemistry, electronics, energy, and biochemistry.[6] The potential on biomedical applications ranges from serving as drug delivery agents in cancer research, currently used in the clinic as a biomedical imaging tool with further promise to be used as theragnostic tools, and in vaccine development as immune system modulators, or gene delivery agents.[3,29–32] As delivery systems, these protect the cargo from being exposed to complex biological environments that may degrade the cargo before reaching its desired destination.[2,29] These particles achieved the already mentioned goals via responsive moieties in their structures. The motifs react to changes in pH, magnetic fields, irradiation, change in temperature, redox, among others.[29,30,33,34] In this thesis, the discussion will focus on how dG derivative intrinsic and self-assembly extrinsic changes affect thermal responsive properties and thiol-responsiveness.

1.3.1. Lower and upper critical solution temperature and its modulation

One of the main precursors to particle assembly is the lower critical solution temperature (LCST), primarily seen in water. LCST is an entropically-driven process in which water-solute hydrations shells are broken down. This happens as the solution temperature is increased.[35–39] As individual solutes maintain a hydrophilic-hydrophobic balance favoring the solute's solubility, only one phase is seen in solution. As the solution temperature is increased, the hydrophilic-hydrophobic balance is shifted. The increase of temperature disturbs the water-solute interaction, making the solute hydrophobic nature overtake such interactions. The distortion of the non-covalent interaction with water molecules forces the association of the solute's hydrophobic fractions. The conglomeration of the solute leads to a phase separation that decreases the transmittance of the solution making it look cloudy making water molecules have higher degree of freedom (Figure 1.2).[40]

Materials that have been extensively developed for LCST are polymers. The LCST in polymers is usually seen as soluble polymers collapsing onto themselves and on each other.[40] Intrinsic (i.e., structural) changes in the polymers can be achieved in a straight forward manner by modifying their structure to have a combination of hydrophilic and hydrophobic elements in their sequence. The more the hydrophilic regions the polymer contains, the higher the LCST will be.[41] Another mechanism used to do this is the mixing of different polymers. Depending on the hydrophobicity of the backbone, the LCST can be increased or decreased.[42] The most utilized one by increasing the molecular weight of the polymer. For example, in related polymers, those with higher molecular weight tend to have lower LCST.[42] These methods are useful to produce a polymer with LCST and modulate said LCST to the application's needs.

In contrast to LCST, the upper critical solution temperature (UCST) is dominated by enthalpic contributions. As the temperature is increased in a two-phase solution, the USCT result in a single-phase solution.[36,43,44] The single-phase is achieved due to the solute's nature to engage in greater interactions between its hydrophilic elements and water molecules.[38] If a material exhibits both phenomena it is common for these to have a UCST lower than its LCST.[45,46] The UCST can be modified by changing intrinsic parameters of the solute.[47,48]

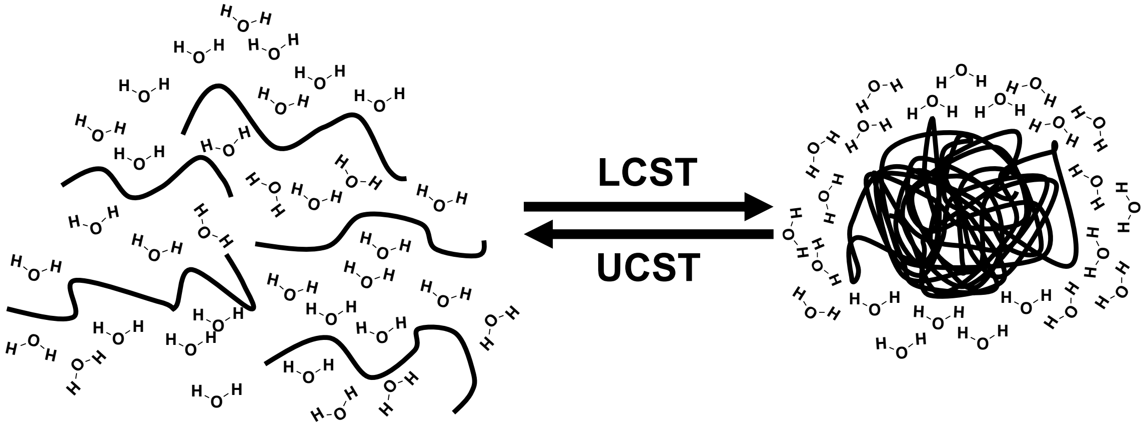

Figure 1.2. Cartoon representation of solubilized polymers conglomerating after solution temperature passed LCST changing the solution from a single phase one to a two-phase solution. The opposite behavior is seen in a two-phase solution when the solution reaches its UCST. After the UCST, a two-phase solution transitions into a single-phase solution.

Similar to LCST, UCST modulation is primarily seen in polymers. The techniques to modulate a polymers' UCST rely mostly on adding hydrophilic moieties to the system.[43] The addition of zwitterionic and hydroxyl groups has become one of the most utilized approaches to include H-bonding moieties. Counterions for the ionic groups in polymers often result in critical changes in the UCST.[43] Mono- or multivalent ions (i.e., Na^+, Cu^{2+}, Cl^-, I^-, BF_4^-, ciannamate, trifluoromethanesulfonate, hexacyanochromate, -ferrate, or -cobaltate) can induce UCST in polymers (i.e., poly(acrylic acid), poly(dimethylaminoethyl methacrylate), poly(2 - methacryloyloxyethyltrimethylammonium), poly(3-methyl-1-(4-

vinylbenzyl)imidazolium), protonated poly(ethylene oxide)-b-poly(2-vinyl pyridine)). The concentration, polarizability and hydration of ions in solution help modulate de UCST.[43]

The presence of counterions produce a change in extrinsic parameters (i.e., experimental conditions like solvent, temperature, etc.). These changes can also modulate the LCST and UCST phenomena. The presence of counterions can inhibit or facilitate the formation of H-bonds between the polymer and water when ionic moieties are present in the polymer.[43] It is important to highlight the essential role that ions play in the solvation of structures like proteins and synthetic polymers.

Ions can be categorized within what's commonly known as the Hofmeister series (Figure 1.3).[49] Here Ions could be organized in a range between opposite extremes ranging from 'kosmotropic' to 'chaotropic', which refer to how these ions organize their hydration shells. Kosmotropic ions have a higher hydration shell as they organize water molecules. These tend to be associated with protein stability as they are not as prone to denaturalize these. These can isolate proteins from the solvent at high concentrations. This isolation produces a salting-out effect by dehydrating proteins (Figure 1.4.a).[50] On the other hand, chaotropic ions are not as prone to organize water molecules. Therefore, chaotropic ions tend to have a higher affinity with solutes and their hydrocarbons. The ion's solute affinity may produce salting-in effect as it serves as a bridge between the solute water molecules.[50,51] High concentrations of chaotropic ions can produce a denaturation of proteins as they interfere with the protein's hydrophobic interactions (Figure 1.4.a).[50,51]

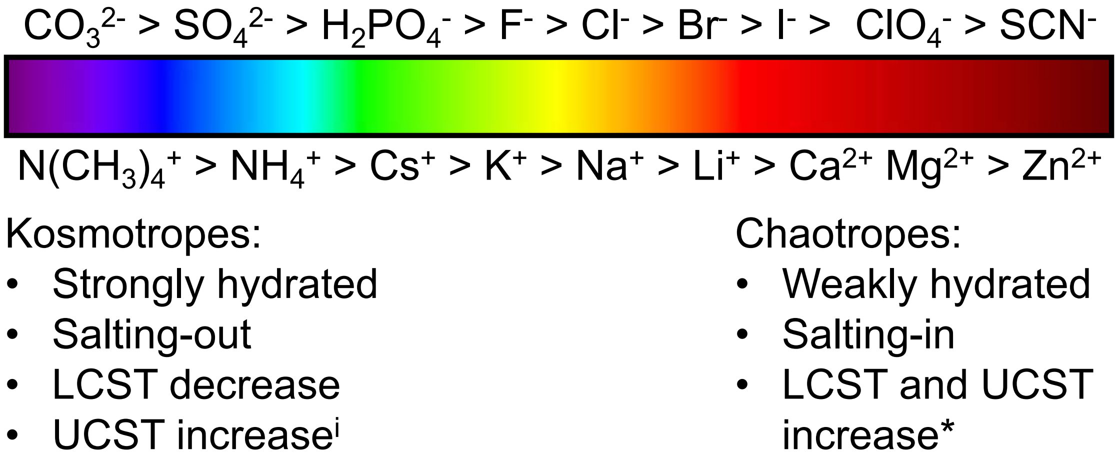

Figure 1.3. The Hofmeister series for anions and cations.[i] UCST behavior can be modified depending on polymer composition such as the introduction of zwitterions.[52] * Chaotropic ions decrease the LCST and UCST once the polymer is saturated. Image adapted from ref [53]

As polymers show thermally-induced responses of LCST and UCST, the chaotropic and kosmotropic ions affect these phenomena. In polymers, these ionic behaviors can be used to stabilize and modulate the LCST and UCST. The action of the resulting thermal response is dependent on the solute and ion concentrations. We can still explain the modulation behaviors to the hydration or dehydration produced by the ions to the solute's different structural domains.[54] Polymers as PNIPAM and NMA show a decrease in LCST when kosmotropic anions are in the solution if compared to chaotropic anions (Figure 1.4.a).[50] Kosmotropic ions dehydration lowers the LCST of polymers in comparison with chaotropic ions. This decrease in LCST can be made even lower by increasing the salt concentration.

As previously mentioned, chaotropic anions produce higher LCST on polymers when compared to kosmotropic anions. The increase in LCST is because as these are weakly hydrated anions, these interact with the solute at a higher probability than kosmotropes. These anions result in interaction bridges between solute and water molecules. As chaotropic anion concentration increases, these lower the LCST of polymers. As the polymer core prone to interact with the weakly hydrated anions, more hydrophobic regions of the polymer are exposed to the solvent. As we already understand that the LCST is an entropically-driven process promoted by the solute's hydrophobicity, it is expected that the polymer collapse within itself in the described environments with a less temperature change as the chaotropic anion concentration increases. This linear behavior is reversed when the polymer becomes saturated with the anions. As the polymer's core is saturated with the weakly hydrated anion, the LCST increases.[50] At this stage, the hydrophobic domains are less likely to collapse into each other as the temperature increases. The chaotropic anion becomes a barrier to said behaviors, so higher temperatures need to be reached to displace said anions. This behavior is seen in PNIPAM and ELP.[50,54]

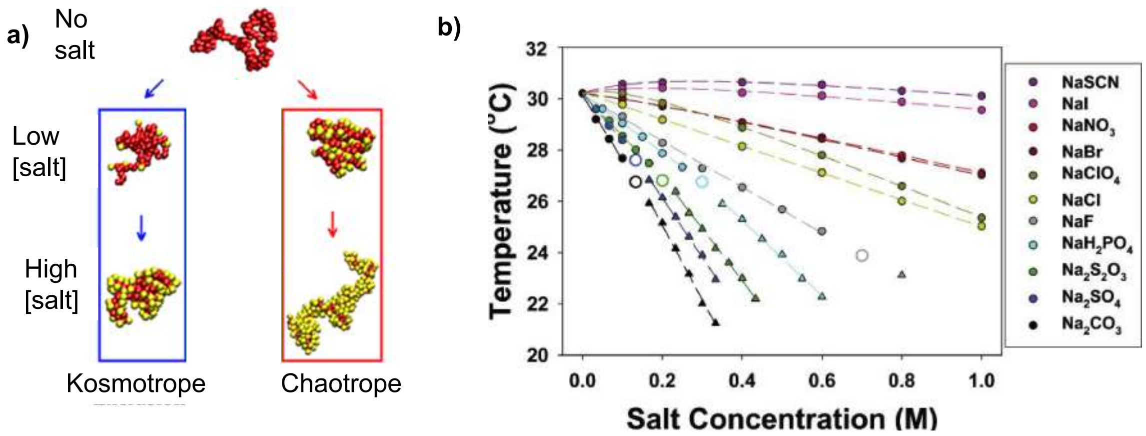

Figure 1.4. a) Schematic depiction of polymers (red) with different concentrations on kormotropic or chaotropic salt (yellow). Image adapted from ref [55] with permission from American Chemical Society, Copyright © 2017, American Chemical Society b) Effects on PNPAM LCST depending on salt concentration. Image reprinted form ref [56] with permission from American Chemical Society, Copyright © 2005, American Chemical Society.

The UCST of a polymer changes in the presence of chaotropic and kosmotropic anions. Still, the UCST change trends can be explained in the same manner as LCST changes. As kosmotropic anions serve as salting-out ions by secluding the solute from the solvent, the UCST increases. Yet this behavior can be different in cases where zwitterion fractions are dominant in a polymer's composition.[52] As chaotropic anions have more favorable interactions with hydrocarbons than kosmotropes, these serve as better interactions between the water molecules and polymers. As a result, the presence of chaotropic anions in solution lowers the UCST.[57] And as already explained for LCST, at higher concentration of the chaotropic salt, the UCST is increased due to polymer saturation.[52] A summary diagram is seen in Figure 1.3.

As previously mentioned, the LCST and UCST modulation by extrinsic parameters as ions in solution can be achieved. Yet this is an undoubtedly delicate balance. Thermal responsive properties take into consideration the hydrophilic-hydrophobic interactions of intrinsic parameters of the solute-solute interactions and extrinsic interactions of water–water, water–ions, water–solutes, ions–solutes, and cations–anions.[52,57,58] *In silico* techniques give us an insight into these.[42] But this is a field that still needs growth for experimental understanding.[52,59]

1.3.2 Biothiols reactive species as a redox response

The redox environment has also been of interest for particle responsive properties. Redox environments can produce a bond cleavage, usually used for drug release.[29] A significant attraction within this field are biothiol response because biothiols as Cys, HCy, or GSH play roles in HIV, cancer, Alzheimer's disease among other afflictions.[26–28] Scientists study the microenvironments of biothiols of Cys in the cells (30 - 500 µM) or glutathione (1 – 5 mM).[60] Making biothiol-responsive particles attractive for treatment or vaccine development. Here we will be discussing the thiol-Michael addition click reaction and the thiazolidine formation in the presence of formyl groups.[61]

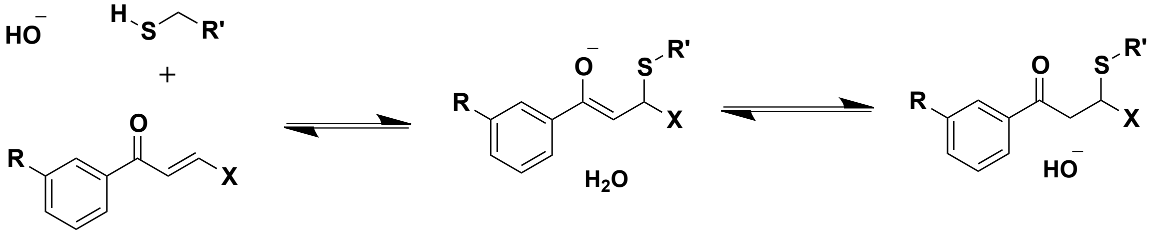

Figure 1.5. Base-catalyzed thiol-Michael reaction including the enolate intermediates.

The thiol-Michael reaction reversibility can be achieved by reacting the thiol moiety with a α,β-unsaturated carbonyl. As the thiol or thiolate performs a nucleophilic attack on the β-carbon, it results in a negatively-charged enolate intermediate that yields the Michael adduct (Figure 1.5).[61,62] The reaction's kinetics depends on thiol's pK_a, *e*lectron-deficiency of the β carbon, and other factors such as a catalyst, its concentration, polarity of the solvent, and solution's pH.[61,63,64] The lower the solution's pH, the faster the reaction due to a more significant proportion of the more nucleophilic thiolate species being present.[63]

The more electron-deficient the Michael acceptor, the greater the reaction rate due to a more electrophilic β-carbon. The addition of thiols to Michael acceptors is practically irreversible when using substrates such as maleimides, acrylates, and acrylamides. These substrates are highly electron-deficient but are reversible with less electron-deficient substrates.[65,66] The thiol-Michael addition has been exploited in reaction-based probes for detecting glutathione.[67,68]

Limited stability at physiological pH and complex synthesis make the thiazolidine formation not suitable for GSH detection.[69] The construction of thiazolidines is ideal for the detection of Cys. In the presence of formyl groups, the building of thiazolidines usually has fast kinetics (within 5 minutes), easily modulated by changes in pH.[69] As in the thio-Michael, thiols and thiolates serve as nucleophiles. These push their electrons towards the formyl carbonyl. As the carbonyl electrons are pushed into the oxygen, it becomes protonated. As the resulting carbon becomes a better electrophile, the amino group serves as its nucleophile. This results in a cyclization reaction. The hydroxy group acts as the leaving group protonated by the amino group and resulting as a water molecule. This reaction results in a thiazolidine group or thiazine in HCy detection.[53,70] As this reaction is easily modulated and in equilibrium, it becomes attractive for developing materials biological sensors and antibody-drug combinations.[71,72]

1.4. Responsive particle development challenges

Particles have been developed using a large variety of materials.[1–3] Researchers consider intrinsic and extrinsic parameters to create the thermal or thiol-responsive particles as previously discussed. The changes in parameters range from polymers synthesis to the environment of its assemblies. But the implementation is not a trivial task. Polymer synthesis and particle formulations require delicate or elaborate steps such as coatings and cross-linkers, which usually employ non-biocompatible environments.[22,73] This results in poor quality control to determine the size, polydispersity, morphology, purity, and stability.[21] For this reason, self-assembly and supramolecular chemistry can help.

1.5. Overview

In this study we stand on the shoulder of giants and decided to explore more biocompatible extrinsic parameters for the formulation of the SGQ. To achieve this we turned to the more chaotropic anion of thiocyanate. The change in extrinsic parameters resulted in the modulation of LCST and the detailed study of UCST of SHS particles. These expansion of SHS resulted in a more in depth understanding on the delicate balance between hydrophilic-hydrophobic interactions. From there, to expand on the intrinsic modifications of SHS particles to introduce an effective biothiol responsive particles. The chalcone containing derivative resulted in a thiol-responsive particle. With molecular characterization of the monomer, we were able to elucidate kinetic information as to how the derivative is reacting with each biothiol. This characterization gave us the understanding of further studies in which we were able to introduce controlled cargo release. Another developed guanine derivative resulted in a formyl-containing SHS particles. The formyl-containing particles were further explored as a biothiol-responsive system via thiazolidine formation using Cys. This Cys responsive particle proved to be effective for cargo encapsulation and release. The results helped expand further the library of thiol-responsive properties of SHS. Both instances of thiol-responsive particles gave us fundamental knowledge that may be used for further development later on. This helps the research team get closer to the overarching goal of developing biocompatible immune system modulation for possible vaccine development.

1.6. References

(1) Tang, L.; Cheng, J. Nonporous Silica Nanoparticles for Nanomedicine Application. *Nano Today* **2013**, *8* (3), 290–312. https://doi.org/https://doi.org/10.1016/j.nantod.2013.04.007.

(2) McNamara, K.; Tofail, S. A. M. Nanoparticles in Biomedical Applications. *Adv. Phys. X* **2017**, *2* (1), 54–88. https://doi.org/10.1080/23746149.2016.1254570.

(3) Vargas, K. M.; Shon, Y.-S. Hybrid Lipid–Nanoparticle Complexes for Biomedical Applications. *J. Mater. Chem. B* **2019**, *7* (5), 695–708. https://doi.org/10.1039/C8TB03084G.

(4) Cristina, F.; Conxita, S. Characterization of Polymeric Nanoparticle Dispersions for Biomedical Applications: Size, Surface Charge and Stability. *Pharm. Nanotechnol.* **2018**, *6* (3), 147–164. https://doi.org/http://dx.doi.org/10.2174/2211738506666180706121515.

(5) McClements, J.; McClements, D. J. Standardization of Nanoparticle Characterization: Methods for Testing Properties, Stability, and Functionality of Edible Nanoparticles. *Crit. Rev. Food Sci. Nutr.* **2016**, *56* (8), 1334–1362. https://doi.org/10.1080/10408398.2014.970267.

(6) Khan, I.; Saeed, K.; Khan, I. Nanoparticles: Properties, Applications and Toxicities. *Arab. J. Chem.* **2019**, *12* (7), 908–931. https://doi.org/https://doi.org/10.1016/j.arabjc.2017.05.011.

(7) Lehn, J.-M. From Supramolecular Chemistry towards Constitutional Dynamic Chemistry and Adaptive Chemistry. *Chem. Soc. Rev.* **2007**, *36* (2), 151–160. https://doi.org/10.1039/B616752G.

(8) Whitesides, G. M.; Boncheva, M. Beyond Molecules: Self-Assembly of Mesoscopic and Macroscopic Components. *Proc. Natl. Acad. Sci.* **2002**, *99* (8), 4769. https://doi.org/10.1073/pnas.082065899.

(9) Mattia, E.; Otto, S. Supramolecular Systems Chemistry. *Nat. Nanotechnol.* **2015**, *10* (2), 111–119. https://doi.org/10.1038/nnano.2014.337.

(10) Jiang, X. C.; Zeng, Q. H.; Chen, C. Y.; Yu, A. B. Self-Assembly of Particles: Some Thoughts and Comments. *J. Mater. Chem.* **2011**, *21* (42), 16797. https://doi.org/10.1039/c1jm12213d.

(11) Rivera-Sánchez, M. del C.; García-Arriaga, M.; Hobley, G.; Morales-de-Echegaray, A. V; Rivera, J. M. Small-Molecule-Based Self-Assembled Ligands for G-Quadruplex DNA Surface Recognition. *ACS Omega* **2017**, *2* (10), 6619–6627. https://doi.org/10.1021/acsomega.7b01255.

(12) Stefan, L.; Monchaud, D. Applications of Guanine Quartets in Nanotechnology and Chemical Biology. *Nat. Rev. Chem.* **2019**, *3* (11), 650–668. https://doi.org/10.1038/s41570-019-0132-0.

(13) Gubala, V.; Betancourt, J. E.; Rivera, J. M. Expanding the Hoogsteen Edge of 2‘-Deoxyguanosine: Consequences for G-Quadruplex Formation. *Org. Lett.* **2004**, *6* (25), 4735–4738. https://doi.org/10.1021/ol048013v.

(14) García-Arriaga, M.; Acosta-Santiago, M.; Cruz, A.; Rivera-Rivera, J. M.; López, G. E.; Rivera, J. M. Probing the Limits of Supramolecular G-Quadruplexes Using Atomistic Molecular Dynamics Simulations. *Inorganica Chim. Acta* **2017**, *468* (Supplement C), 209–222. https://doi.org/https://doi.org/10.1016/j.ica.2017.08.051.

(15) Betancourt, J. E.; Martín-Hidalgo, M.; Gubala, V.; Rivera, J. M. Solvent-Induced High Fidelity Switching Between Two Discrete Supramolecules. *J. Am. Chem. Soc.* **2009**, *131* (9), 3186–3188. https://doi.org/10.1021/ja809612d.

(16) Betancourt, J. E.; Rivera, J. M. Tuning Thermoresponsive Supramolecular G-Quadruplexes. *Langmuir* **2015**, *31* (7), 2095–2103. https://doi.org/10.1021/la504446k.

(17) Betancourt, J. E.; Subramani, C.; Serrano-Velez, J. L.; Rosa-Molinar, E.; Rotello, V. M.; Rivera, J. M. Drug Encapsulation within Self-Assembled Microglobules Formed by Thermoresponsive Supramolecules. *Chem. Commun.* **2010**, *46* (45), 8537. https://doi.org/10.1039/c0cc04063k.

(18) Negrón, L. M.; Meléndez-Contés, Y.; Rivera, J. M. Patchy Supramolecules as Versatile Tools To Probe Hydrophobicity in Nanoglobular Systems. *J. Am. Chem. Soc.* **2013**, *135* (10), 3815–3817. https://doi.org/10.1021/ja401373h.

(19) Santos, S.; Ramírez, M.; Miranda, E.; Reyes, N.; Martínez, O.; Acosta-Santiago, M.; Rivera, J.; Otero, M. Enhancement of Immune Responses by Guanosine-Based Particles in DNA Plasmid Formulations against Infectious Diseases. *J. Immunol. Res.* **2019**, *2019*, 15. https://doi.org/10.1155/2019/3409371.

(20) Anselmo, A. C.; Mitragotri, S. Nanoparticles in the Clinic. *Bioeng. Transl. Med.* **2016**, *1* (1), 10–29. https://doi.org/10.1002/btm2.10003.

(21) Hua, S.; de Matos, M. B. C.; Metselaar, J. M.; Storm, G. Current Trends and Challenges in the Clinical Translation of Nanoparticulate Nanomedicines: Pathways for Translational Development and Commercialization. *Front. Pharmacol.* **2018**, *9*. https://doi.org/10.3389/fphar.2018.00790.

(22) Wolfram, J.; Zhu, M.; Yang, Y.; Shen, J.; Gentile, E.; Paolino, D.; Fresta, M.; Nie, G.; Chen, C.; Shen, H.; Zhao, M. F. and Y. Safety of Nanoparticles in Medicine. *Current Drug Targets*. 2015, pp 1671–1681. https://doi.org/http://dx.doi.org/10.2174/1389450115666140804124808.

(23) Smith, D. M.; Simon, J. K.; Baker Jr, J. R. Applications of Nanotechnology for Immunology. *Nat. Rev. Immunol.* **2013**, *13* (8), 592–605. https://doi.org/10.1038/nri3488.

(24) Tedja, R.; Soeriyadi, A. H.; Whittaker, M. R.; Lim, M.; Marquis, C.; Boyer, C.; Davis, T. P.; Amal, R. Effect of TiO2 Nanoparticle Surface Functionalization on Protein Adsorption, Cellular Uptake and Cytotoxicity: The Attachment of PEG Comb Polymers Using Catalytic Chain Transfer and Thiol–Ene Chemistry. *Polym. Chem.* **2012**, *3* (10), 2743. https://doi.org/10.1039/c2py20450a.

(25) Stuart, M. A. C.; Huck, W. T. S.; Genzer, J.; Müller, M.; Ober, C.; Stamm, M.; Sukhorukov, G. B.; Szleifer, I.; Tsukruk, V. V; Urban, M.; Winnik, F.; Zauscher, S.; Luzinov, I.; Minko, S. Emerging Applications of Stimuli-Responsive Polymer Materials. *Nat. Mater.* **2010**, *9* (2), 101–113. https://doi.org/10.1038/nmat2614.

(26) Isokawa, M.; Kanamori, T.; Funatsu, T.; Tsunoda, M. Analytical Methods Involving Separation Techniques for Determination of Low-Molecular-Weight Biothiols in Human Plasma and Blood. *J. Chromatogr. B* **2014**, *964*, 103–115. https://doi.org/https://doi.org/10.1016/j.jchromb.2013.12.041.

(27) Hamley, I. W. The Amyloid Beta Peptide: A Chemist's Perspective. Role in Alzheimer's and Fibrillization. *Chem. Rev.* **2012**, *112* (10), 5147–5192. https://doi.org/10.1021/cr3000994.

(28) Borges-Santos, M. D.; Moreto, F.; Pereira, P. C. M.; Ming-Yu, Y.; Burini, R. C. Plasma Glutathione of HIV+ Patients Responded Positively and Differently to Dietary Supplementation with Cysteine or Glutamine. *Nutrition* **2012**, *28* (7), 753–756. https://doi.org/https://doi.org/10.1016/j.nut.2011.10.014.

(29) Li, F.; Lu, J.; Kong, X.; Hyeon, T.; Ling, D. Dynamic Nanoparticle Assemblies for Biomedical Applications. *Adv. Mater.* **2017**, *29* (14), 1605897. https://doi.org/10.1002/adma.201605897.

(30) Wilson, J. T.; Keller, S.; Manganiello, M. J.; Cheng, C.; Lee, C.-C.; Opara, C.; Convertine, A.; Stayton, P. S. PH-Responsive Nanoparticle Vaccines for Dual-Delivery of Antigens and Immunostimulatory Oligonucleotides. *ACS Nano* **2013**, *7* (5), 3912–3925. https://doi.org/10.1021/nn305466z.

(31) Chen, W.; Li, F.; Tang, Y.; Yang, S.; Li, J.; Yuan, Z.; Liu, Y.; Zhou, X.; Liu, C.; Zhang, X. Stepwise PH-Responsive Nanoparticles for Enhanced Cellular Uptake and on-Demand Intracellular Release of Doxorubicin. *Int. J. Nanomedicine* **2017**, *Volume 12*, 4241–4256. https://doi.org/10.2147/IJN.S129748.

(32) Roux, R.; Ladavière, C.; Montembault, A.; Delair, T. Particle Assemblies: Toward New Tools for Regenerative Medicine. *Mater. Sci. Eng. C* **2013**, *33* (3), 997–1007. https://doi.org/https://doi.org/10.1016/j.msec.2012.12.002.

(33) Schattling, P.; Jochum, F. D.; Theato, P. Multi-Stimuli Responsive Polymers - the All-in-One Talents. *Polym. Chem.* **2014**, *5* (1), 25–36. https://doi.org/10.1039/C3PY00880K.

(34) Gao, W.; M. Chan, J.; C. Farokhzad, O. PH-Responsive Nanoparticles for Drug Delivery. *Mol. Pharm.* **2010**, *7* (6), 1913–1920. https://doi.org/10.1021/mp100253e.

(35) Scherzinger, C.; Schwarz, A.; Bardow, A.; Leonhard, K.; Richtering, W. Cononsolvency of Poly-N-Isopropyl Acrylamide (PNIPAM): Microgels versus Linear Chains and Macrogels. *Curr. Opin. Colloid Interface Sci.* **2014**, *19* (2), 84–94. https://doi.org/https://doi.org/10.1016/j.cocis.2014.03.011.

(36) Seuring, J.; Agarwal, S. Polymers with Upper Critical Solution Temperature in Aqueous Solution. *Macromol. Rapid Commun.* **2012**, *33* (22), 1898–1920. https://doi.org/10.1002/marc.201200433.

(37) Pietsch, C.; Hoogenboom, R.; Schubert, U. S. PMMA Based Soluble Polymeric Temperature Sensors Based on UCST Transition and Solvatochromic Dyes. *Polym. Chem.* **2010**. https://doi.org/10.1039/c0py00162g.

(38) Ougizawa, T.; Inoue, T. UCST and LCST Behavior in Polymer Blends and Its Thermodynamic Interpretation. *Polym. J.* **1986**, *18* (7), 521–527. https://doi.org/10.1295/polymj.18.521.

(39) Martin, E. W.; Mittag, T. Relationship of Sequence and Phase Separation in Protein Low-Complexity Regions. *Biochemistry* **2018**, *57* (17), 2478–2487. https://doi.org/10.1021/acs.biochem.8b00008.

(40) Zhang, Q.; Weber, C.; Schubert, U. S.; Hoogenboom, R. Thermoresponsive Polymers with Lower Critical Solution Temperature: From Fundamental Aspects and Measuring Techniques to Recommended Turbidimetry Conditions. *Materials Horizons*. 2017. https://doi.org/10.1039/c7mh00016b.

(41) Schild, H. G. Poly(N-Isopropylacrylamide): Experiment, Theory and Application. *Prog. Polym. Sci.* **1992**, *17* (2), 163–249. https://doi.org/10.1016/0079-6700(92)90023-R.

(42) Dalgakiran, E.; Tatlipinar, H. The Role of Hydrophobic Hydration in the LCST Behaviour of POEGMA300 by All-Atom Molecular Dynamics Simulations. *Phys. Chem. Chem. Phys.* **2018**, *20* (22), 15389–15399. https://doi.org/10.1039/C8CP02026D.

(43) Niskanen, J.; Tenhu, H. How to Manipulate the Upper Critical Solution Temperature (UCST)? *Polym. Chem.* **2017**, *8* (1), 220–232. https://doi.org/10.1039/C6PY01612J.

(44) Kanta Sharker, K.; Ohara, Y.; Shigeta, Y.; Ozoe, S.; Yusa, S. Upper Critical Solution Temperature (UCST) Behavior of Polystyrene-Based Polyampholytes in Aqueous Solution. *Polymers (Basel).* **2019**, *11* (2), 265. https://doi.org/10.3390/polym11020265.

(45) Yin, J.; Hu, J.; Zhang, G.; Liu, S. Schizophrenic Core–Shell Microgels: Thermoregulated Core and Shell Swelling/Collapse by Combining UCST and LCST Phase Transitions. *Langmuir* **2014**, *30* (9), 2551–2558. https://doi.org/10.1021/la500133y.

(46) Mäkinen, L.; Varadharajan, D.; Tenhu, H.; Hietala, S. Triple Hydrophilic UCST–LCST Block Copolymers. *Macromolecules* **2016**, *49* (3), 986–993. https://doi.org/10.1021/acs.macromol.5b02543.

(47) Kreuzer, L. P.; Widmann, T.; Bießmann, L.; Hohn, N.; Pantle, J.; Märkl, R.; Moulin, J.-F.; Hildebrand, V.; Laschewsky, A.; Papadakis, C. M.; Müller-Buschbaum, P. Phase Transition Kinetics of Doubly Thermoresponsive Poly(Sulfobetaine)-Based Diblock Copolymer Thin Films. *Macromolecules* **2020**, *53* (8), 2841–2855. https://doi.org/10.1021/acs.macromol.0c00046.

(48) Xing, C.; Shi, Z.; Tian, J.; Sun, J.; Li, Z. Charge-Determined LCST/UCST Behavior in Ionic Polypeptoids. *Biomacromolecules* **2018**, *19* (6), 2109–2116. https://doi.org/10.1021/acs.biomac.8b00240.

(49) Tian, R.; Yang, G.; Tang, Y.; Liu, X.; Li, R.; Zhu, H.; Li, H. Origin of Hofmeister Effects for Complex Systems. *PLoS One* **2015**, *10* (7), e0128602.

(50) Okur, H. I.; Hladílková, J.; Rembert, K. B.; Cho, Y.; Heyda, J.; Dzubiella, J.; Cremer, P. S.; Jungwirth, P. Beyond the Hofmeister Series: Ion-Specific Effects on Proteins and Their Biological Functions. *J. Phys. Chem. B* **2017**, *121* (9), 1997–2014. https://doi.org/10.1021/acs.jpcb.6b10797.

(51) Zangi, R. Can Salting-In/Salting-Out Ions Be Classified as Chaotropes/Kosmotropes? *J. Phys. Chem. B* **2009**, *114* (1), 643–650. https://doi.org/10.1021/jp909034c.

(52) Hildebrand, V.; Laschewsky, A.; Päch, M.; Müller-Buschbaum, P.; Papadakis, C. M. Effect of the Zwitterion Structure on the Thermo-Responsive Behaviour of Poly(Sulfobetaine Methacrylates). *Polym. Chem.* **2017**, *8* (1), 310–322. https://doi.org/10.1039/C6PY01220E.

(53) Esterbauer, H.; Ertl, A.; Scholz, N. The Reaction of Cysteine with α,β-Unsaturated Aldehydes. *Tetrahedron* **1976**, *32* (2), 285–289. https://doi.org/10.1016/0040-4020(76)87015-9.

(54) Zhang, Y.; Furyk, S.; Sagle, L. B.; Cho, Y.; Bergbreiter, D. E.; Cremer, P. S. Effects of Hofmeister Anions on the LCST of PNIPAM as a Function of Molecular Weight. *J. Phys. Chem. C* **2007**, *111* (25), 8916–8924. https://doi.org/10.1021/jp0690603.

(55) Heyda, J.; I. Okur, H.; Hladílková, J.; B. Rembert, K.; Hunn, W.; Yang, T.; Dzubiella, J.; Jungwirth, P.; S. Cremer, P. Guanidinium Can Both Cause and Prevent the Hydrophobic Collapse of Biomacromolecules. *J. Am. Chem. Soc.* **2017**, *139* (2), 863–870. https://doi.org/10.1021/jacs.6b11082.

(56) Zhang, Y.; Furyk, S.; Bergbreiter, D. E.; Cremer, P. S. Specific Ion Effects on the Water Solubility of Macromolecules: PNIPAM and the Hofmeister Series. *J. Am. Chem. Soc.* **2005**, *127* (41), 14505–14510. https://doi.org/10.1021/ja0546424.

(57) Kang, B.; Tang, H.; Zhao, Z.; Song, S. Hofmeister Series: Insights of Ion Specificity from Amphiphilic Assembly and Interface Property. *ACS Omega* **2020**, *5* (12), 6229–6239. https://doi.org/10.1021/acsomega.0c00237.

(58) Kurzbach, D.; Hassouneh, W.; McDaniel, J. R.; Jaumann, E. A.; Chilkoti, A.; Hinderberger, D. Hydration Layer Coupling and Cooperativity in Phase Behavior of Stimulus Responsive Peptide Polymers. *J. Am. Chem. Soc.* **2013**, *135* (30), 11299–11308. https://doi.org/10.1021/ja4047872.

(59) Kim, H.; Jeon, B. jin; Kim, S.; Jho, Y. S.; Hwang, D. S. Upper Critical Solution Temperature (UCST) Behavior of Coacervate of Cationic Protamine and Multivalent Anions. *Polymers (Basel).* **2019**. https://doi.org/10.3390/polym11040691.

(60) Tian, M.; Guo, F.; Sun, Y.; Zhang, W.; Miao, F.; Liu, Y.; Song, G.; Ho, C.-L.; Yu, X.; Sun, J. Z.; Wong, W.-Y. A Fluorescent Probe for Intracellular Cysteine Overcoming the Interference by Glutathione. *Org. Biomol. Chem.* **2014**, *12* (32), 6128–6133. https://doi.org/10.1039/C4OB00382A.

(61) Nair, D. P.; Podgórski, M.; Chatani, S.; Gong, T.; Xi, W.; Fenoli, C. R.; Bowman, C. N. The Thiol-Michael Addition Click Reaction: A Powerful and Widely Used Tool in Materials Chemistry. *Chem. Mater.* **2014**, *26* (1), 724–744. https://doi.org/10.1021/cm402180t.

(62) Boutureira, O.; Bernardes, G. J. L. Advances in Chemical Protein Modification. *Chem. Rev.* **2015**, *115* (5), 2174–2195. https://doi.org/10.1021/cr500399p.

(63) Krenske, E. H.; Petter, R. C.; Houk, K. N. Kinetics and Thermodynamics of Reversible Thiol Additions to Mono- and Diactivated Michael Acceptors: Implications for the Design of Drugs That Bind Covalently to Cysteines. *J. Org. Chem.* **2016**, *81* (23), 11726–11733. https://doi.org/10.1021/acs.joc.6b02188.

(64) Chan, J. W.; Hoyle, C. E.; Lowe, A. B.; Bowman, M. Nucleophile-Initiated Thiol-Michael Reactions: Effect of Organocatalyst, Thiol, and Ene. *Macromolecules* **2010**, *43* (15), 6381–6388. https://doi.org/10.1021/ma101069c.

(65) Chen, J.; Jiang, X.; Carroll, S. L.; Huang, J.; Wang, J. Theoretical and Experimental Investigation of Thermodynamics and Kinetics of Thiol-Michael Addition Reactions: A Case Study of Reversible Fluorescent Probes for Glutathione Imaging in Single Cells. *Org. Lett.* **2015**, *17* (24), 5978–5981. https://doi.org/10.1021/acs.orglett.5b02910.

(66) Shi, B.; Greaney, M. F. Reversible Michael Addition of Thiols as a New Tool for Dynamic Combinatorial Chemistry. *Chem. Commun.* **2005**, No. 7, 886–888. https://doi.org/10.1039/B414300K.

(67) Kim, G.-J.; Lee, K.; Kwon, H.; Kim, H.-J. Ratiometric Fluorescence Imaging of Cellular Glutathione. *Org. Lett.* **2011**, *13* (11), 2799–2801. https://doi.org/10.1021/ol200967w.

(68) Jiang, X.; Yu, Y.; Chen, J.; Zhao, M.; Chen, H.; Song, X.; Matzuk, A. J.; Carroll, S. L.; Tan, X.; Sizovs, A.; Cheng, N.; Wang, M. C.; Wang, J. Quantitative Imaging of Glutathione in Live Cells Using a Reversible Reaction-Based Ratiometric Fluorescent Probe. *ACS Chem. Biol.* **2015**, *10* (3), 864–874. https://doi.org/10.1021/cb500986w.

(69) Bermejo-Velasco, D.; Nawale, G. N.; Oommen, O. P.; Hilborn, J.; Varghese, O. P. Thiazolidine Chemistry Revisited: A Fast, Efficient and Stable Click-Type Reaction at Physiological PH. *Chem. Commun.* **2018**, *54* (88), 12507–12510. https://doi.org/10.1039/C8CC05405C.

(70) Ratner, S.; Clarke, H. T. The Action of Formaldehyde upon Cysteine. *J. Am. Chem. Soc.* **1937**, *59* (1), 200–206. https://doi.org/10.1021/ja01280a050.

(71) Casi, G.; Huguenin-Dezot, N.; Zuberbühler, K.; Scheuermann, J.; Neri, D. Site-Specific Traceless Coupling of Potent Cytotoxic Drugs to Recombinant Antibodies for Pharmacodelivery. *J. Am. Chem. Soc.* **2012**, *134* (13), 5887–5892. https://doi.org/10.1021/ja211589m.

(72) Cai, Y.; Zhang, Y.; Yuan, W.; Yao, J.; Yan, G.; Lu, H. A Thiazolidine Formation-Based Approach for Ultrafast and Highly Efficient Solid-Phase Extraction of N-Glycoproteome. *Anal. Chim. Acta* **2020**, *1100*, 174–181. https://doi.org/https://doi.org/10.1016/j.aca.2019.12.001.

(73) Crucho, C. I. C.; Barros, M. T. Polymeric Nanoparticles: A Study on the Preparation Variables and Characterization Methods. *Mater. Sci. Eng. C* **2017**, *80*, 771–784. https://doi.org/https://doi.org/10.1016/j.msec.2017.06.004.

Chapter 2. Expanding the Library of Supramolecular Particles Based on G-derivatives

2.1. Abstract

Colloidal particles ranging from the nano to the microscale show great promise in the delivery and enhancement of therapeutic agents. The formulation of these particles usually includes crosslinkers, no biocompatible solvents or lengthy procedures that are not cost-effective. We have developed particles termed Supramolecular Hacky Sacks (SHS) via thermoresponsive Supramolecular G-quadruplexes (SGQs) with lower critical solution temperature (LCST). SGQs being themselves the salting-in result of G-derivatives. Although the preparation of the SHS particles is a simple formulation, for G-derivatives to proceed in the salting-in process there currently needs to be a high concentration of KI (2M). Such high salt concentrations often interfere with the biomedical applications of the resulting particles. In this chapter we show a systematic study of self-assembly and thermoresponsive properties with KSCN over a range of concentrations. The use of thiocyanate anions greatly enhances the solubility of the G-derivatives, also enabling modulation of the LCST. Salting-in experiments with KSCN show up to a 20-fold decrease of minimum salt needed to self-assemble on some species when compared to KI. These experiments also revealed these systems have an upper critical solution temperature (UCST) for each sample. Both, the LCST and UCST are modulated with the presence of KSCN. A phase diagram of SHS particles as a function of the concentration of KSCN reveals which G-derivatives can produce SHS particles under

biocompatible environments. Dynamic light scattering experiments allowed us to determine the size and distribution of the SHS particles, and their relative abundance as a function of temperature and other extrinsic parameters. The spherical morphology of the SHS particles and their encapsulation complexes was confirmed with confocal microscopy experiments. We were able to prevent the reversibility between SGQ and SHS particles by reducing ionic strength in solution in a process termed ‘fixing’. This reduction of salt concentration of the solution results in a potentially more biocompatible system. The simplification of SHS particle formulation for a more biocompatible one opens the door to further *in vitro* studies serving as drug-delivery agents in cancer research, and in vaccine development, as immune system modulators or gene delivery agents.

2.2. Introduction

As the research on particles has become more popular since the early 1990s, the interest in them being responsive has become a significant focus.[1–4] Researchers develop particles with a wide variety of stimuli from pH changes, magnetic fields, photosensitive, molecular recognition, and thermal responsiveness are just a few to mention.[5–9] Biorelevant applications for responsive properties have emerged of great interest to researchers. Thermal-responsive properties have been fundamental in the development of this field. The lower critical solution temperature (LCST) phenomenon is a process whereby many developed particles rely on for formulation and bio-relevant applications.[9,10] When the temperature of a system is below the LCST it exists as a single phase. A second phase is formed above the LCST, commonly making the solution look cloudy.[11] This is primarily due to the formation of colloidal particles, or gels.[9,12,13] This phenomenon can be explained by the hydrophobic interactions of the solute with its medium. As the temperature increases, the hydration shells are interrupted, so the solutes collapse into themselves or each other to form said structures.[11] The reverse behavior is termed upper critical solution temperature (UCST).[14,15] As LCST is an entropic behavior, UCST is an enthalpic process resulting in the solvation of a phase into another.[16–18]

Polymers dominate the field of particles for bio-relevant applications.[4,19,20] Polymer particle formulations usually involve employing cumbersome or elaborate steps, coatings, cross-linkers, and non-biocompatible environments.[2,21] This leads to complications in quality control to determine the size, polydispersity, morphology, purity, and stability.[22] Taking into consideration that biological systems provide very specific constraints, these are not trivial matters to address.[3,21,22] Supramolecular chemistry can address some of these issues by leveraging the power of non-covalent interactions in combination with covalent chemistry.

Supramolecular self-assembly provides a convenient tool to synthesize small molecules and develop responsive particles.[23,24] In this endeavor, we are using 2'-deoxyguanosine (G) derivatives that can self-recognize into tetrads via H-bonding.[25] While in the presence of K^+, these tetrads stack. We previously modified these to include a H-bond acceptor like a *meta*-carbonyl at the C8 of the guanine moiety, which leads to the formation of Supramolecular Guanine Quadruplexes (SGQ) with enhanced fidelity and stability.[25,26] As we have previously reported, dendron containing modifications at the sugar of the G-derivatives can produce an array of SGQ showing the LCST phenomenon, which in turn leads to the formation of colloidal particles termed Supramolecular Hacky Sacks (SHS).[27]

To this date, the formation of SHS particles require the use of high ionic strength usually obtained by the addition of 2 M KI to a PBS buffer. A synergistic relationship between the two counter ions leads to the potassium cation stabilizing the G-tetramers while the iodide anion helps solubilize the SGQ structures. Nevertheless, this concentration of KI is not biocompatible when we take into consideration that blood plasma contains between 3.2 - 5.2 mM of potassium.[28] In the search for finding biocompatible environments for particle formulations, we decided to evaluate the Hofmeister anion series to find alternatives to iodide. As the iodide serves to solubilize the SGQ, we evaluate another chaotropic anion, thiocyanate ($^{-}$SCN).[29,30] We hypothesized that this change for a slightly more chaotropic anion (an extrinsic parameter) would reveal conditions requiring minimal salt concentrations to dissolve the SGQ structures while preserving the LCST phenomenon. The latter is critical since in a previous article we have reported that KSCN does indeed enhance the solubility of SGQs, however, at the relatively high concentrations tested (i.e., 2 M) the resulting structures showed no LCST at temperatures below those corresponding to the thermal dissociation (e.g., T_m) of the SGQs.[27]

Changing extrinsic parameters use to promote the self-assembly of G-derivatives into SGQs is expected to produce fundamental changes in corresponding SHS particles such as their size, and stability among others. Thus, in this study we started by synthesizing a small library of G-derivatives having a variety different *meta*-carbonyphenyl moieties attached to the C8 of the guanine group. The developed G-derivatives are compared with a previously studied G-derivative, which have longer alkyl chains in the esters modified attached to the 3'- and 5'- positions at the 2'-deoxyribose group (Scheme 2.1).[27] These changes are expected to enable a library of formulations for their corresponding SHS particles. After the synthesis and structural characterization, we performed salting-in studies with KSCN, followed by structural and stability characterization of the resulting SGQ structures. These studies were in turn followed by determination of the corresponding LCST and UCST and concluding with measurements of the SHS particles characterization and stabilization. Similar to polymeric systems, the properties of these SHS particles result from the balance between hydrophobic and hydrophilic groups in the SGQs and their constituent G-derivatives. These efforts should facilitate the production of libraries of SHS particles suitable for biological applications.

2.3. Results and Discussion

2.3.1. G Derivative

2.3.1.1. Synthesis

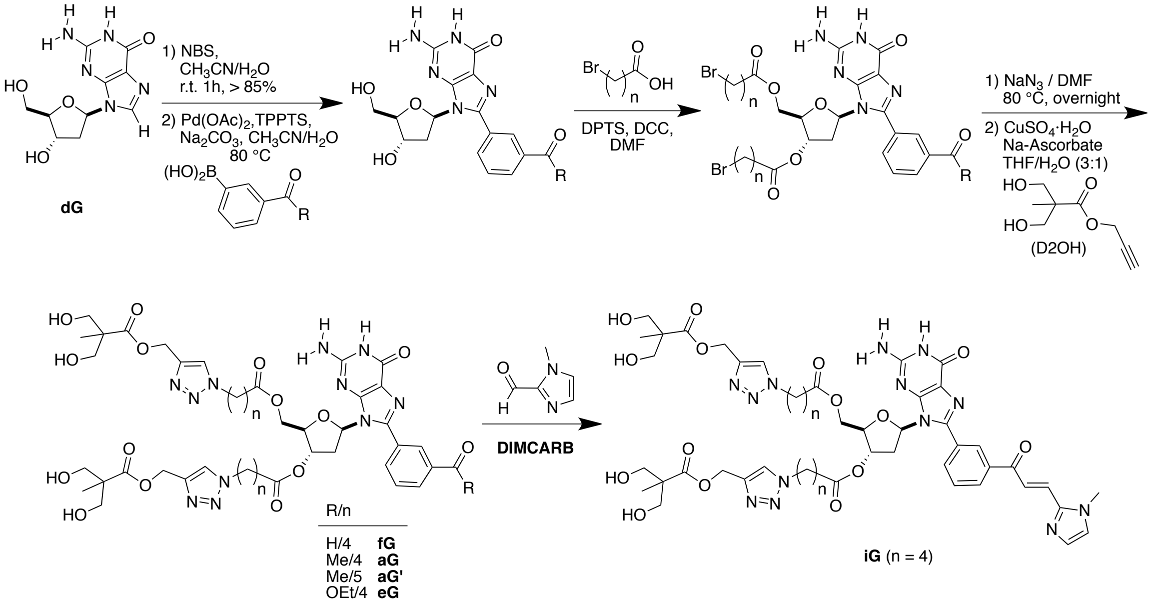

Scheme 2.1. Synthesis of G-derivatives containing four types of carbonyl derivatives R/n.

For this endeavour we applied the previously reported synthetic protocols for related G-derivatives to prepare **fG**, **aG**, **aG’**, **eG**, and **iG**.[26,27,31,32,32–34] Briefly, as illustrated in Scheme 2.1, bromination of 2’-deoxyguanosine and subsequent Suzuki-Miyaura, the Steglich reaction with 5-bromovaleric acid was employed to esterify the 3’- and 5’-OH groups.[31–33] Subsequently, a nucleophilic substitution (S_N2) using NaN_3, followed by the copper catalyzed Huisgen cycloaddition click reaction with an alkynyl containing dendron[34–36] furnished derivatives **fG**, **aG**, **eG**. A DIMCARB catalyzed Claisen Schmidt condensation between **aG** and formyl imidazole provided **iG**. The detailed preparative protocols and spectroscopic characterization is included in the Experimental Procedures section at the end of the chapter Figures 2.11 – 2.16.

2.3.1.2. Salting-in

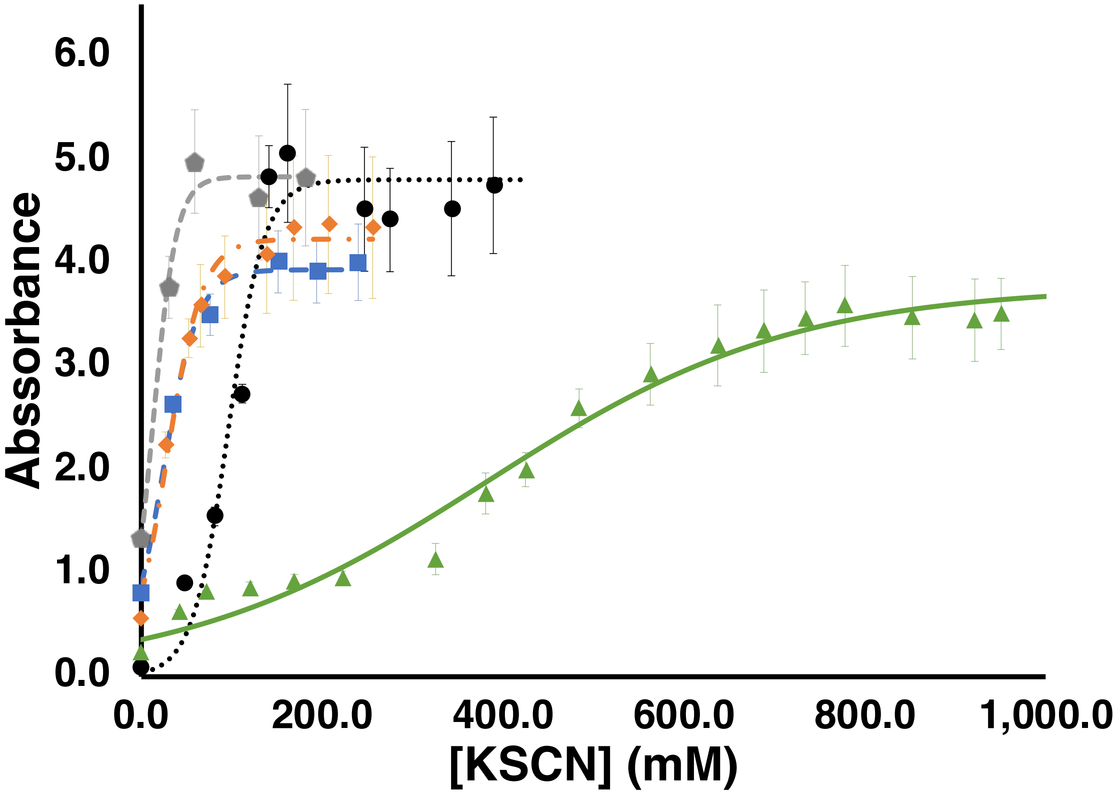

Figure 2.1. Absorbance of solutions of G-derivatives (1 mM in PBS, pH 7.4) as a function of the concentration of KSCN at 2 °C: **aG'** (black ●, fitting R^2 = 0.9221), **aG** (gray ⬟, fitting R^2 = 0.9714), **eG** (blue ■, fitting R^2 = 0.9862), **fG** (orange ◆, fitting R^2 = 0.9775) and **iG** (green ▲, fitting R^2 = 0.9753). All absorbance measurements were performed at λ_{max} 376 nm for **iG** and 300 nm for the other G-derivatives. Curve fittings were obtained from a 4-parameter logistic equation and are used as trend lines to guide the eye.

With the G-derivatives in hand, we decided to look into the minimum concentration of KSCN needed to promote a salting-in process ($[KSCN]_{min}$). It is expected that as the [KSCN] is increased, the G-derivatives solubilize, but each at different concentrations of KSCN due to their varied hydrophobicity. By measuring the absorbance of a solution of each G-derivative, dissolved at 1 mM in PBS, pH 7.4, in increments of [KSCN], we anticipated the absorbance to stabilize once all the G-derivative has entered solution. While this experiment does not reveal details of the self-assembly of each G-derivative, it has to be performed at low temperature (2 °C), anticipating the likelihood of forming SGQs, which in turn would show the LCST phenomenon. Partial solubility is achieved for all G-derivatives upon the addition of even small amounts of KSCN (Figure 2.1). The absorbance stabilizes after KSCN concentrations of 200 mM for **aG'**, 50 mM for **aG**, 100 mM for **eG**, and for **fG**, and 800 mM for **iG**, which indicate that these represent the $[KSCN]_{min}$ for these G-derivatives.

2.3.2 SGQ Characterization

2.3.2.1 SGQ Structure Characterization

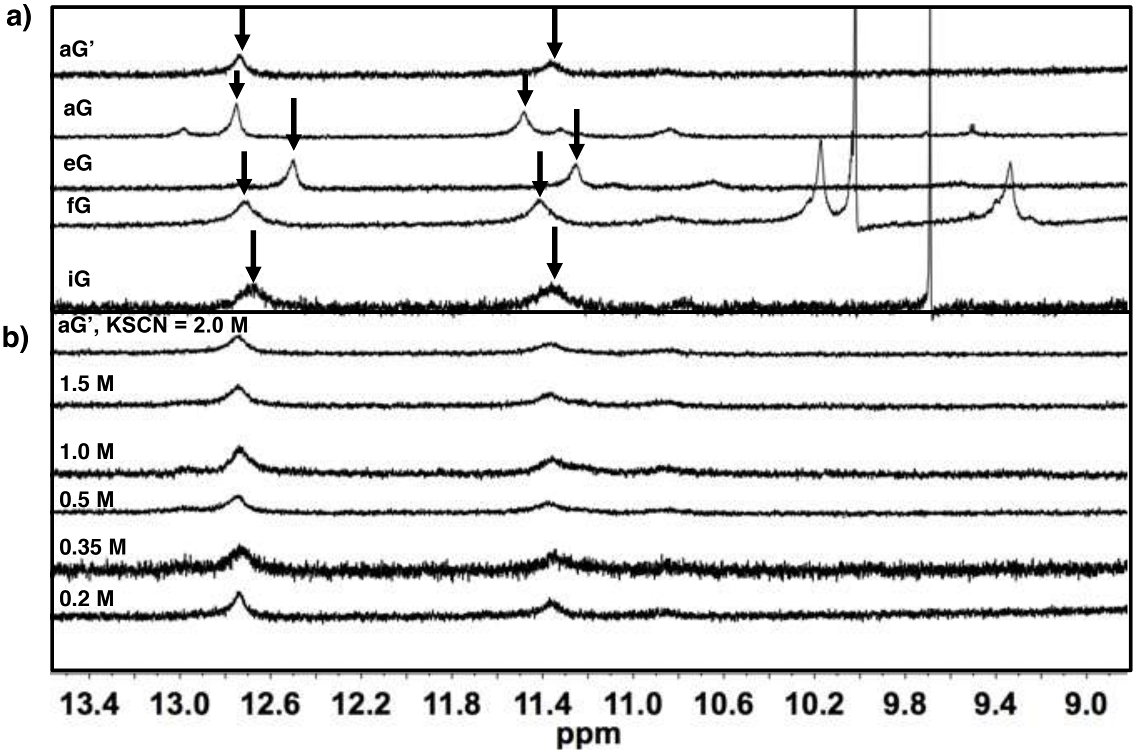

Figure 2.2. ^1H NMR water-suppression experiments that reveal the formation of the corresponding SGQs for: (a) various G-derivatives at their corresponding $[KSCN]_{min}$ (b) **aG'** in solutions with varying amounts of KSCN (12.50–11.15 ppm). All experiments were performed at 5 °C in PBS, pH 7.4 with 2% D_2O solutions containing 1 mM of the corresponding G-derivative and KSCN. The experiments in part a were measured at 700 MHz and those in part b at 500 MHz. The arrows in part a indicate the N1H peaks characteristic of hexadecameric SGQs and some of the remaining minor peaks likely corresponding to SGQs with lower molecularities such as dodecamers and/or octamers.

Because of the nature of chaotropic ions, it is possible that the salting-in may result in solubilization of the G-derivative but not necessarily the self-assembly into the corresponding SGQ.[30,37] To determine the presence of an SGQ, we look into molecular characterization experiments based on NMR. In previous studies, we have shown vital elements that help us elucidate the self-assembly of

G-derivatives into SGQs. These are based on a series of signature peaks, most prominently, those seen in ranges of 13–11 ppm.[38–40] As shown in Figure 2.2a, we were able to see the occurrence of these signature peaks in the solutions. Peaks highlighted by arrows result from the N1H of the guanine base. The H-bonding taking place within the tetrad minimizes the exchange with the solvent water molecules making readily visible by NMR. The two predominant N1H signals in this range show the distinct chemical shift of hexadecameric SGQs as our group has reported before.[41] A the hexadecameric SGQ forms from the stacking of four tetrads, the outer and the inner tetrads provide different chemical environments in this D4-symmetric system.[42] This difference in chemical environments results in the N1H of the outer tetrad showing in a lower field compared to the N1H of the inner tetrad.[38] SGQ structures of different molecularities (e.g., dodecamers, octamers) are responsible for other minor signals in that region. These findings support that the corresponding $[\mathrm{KSCN}]_{\mathrm{min}}$ is a suitable concentration to promote the self-assembly of all these G-derivatives into their corresponding SGQ structures.

We also explored the effects of higher concentrations of KSCN to evaluate the potential disruption of the SGQs at concentrations of KSCN to up to 2 M for **aG’** (**SGQ-aG’**) based in a previously determined $[\mathrm{KI}]_{\mathrm{min}}$ = 2 M.[27] The rationale behind this was to test the possibility of an induce disassembly analogous to that observed for proteins that denature at high ionic strengths of chaotropic salts like KSCN. While we have previously reported that high concentrations of iodide (e.g., 2-4 M) do not disrupt the formation of SGQs, there are instances where high concentrations of thiocyanate destabilize proteins and induced a salting-out effect due to denaturation.[37] These effects result from the strong binding of such chaotropes to the solute, which in turn interrupts the protein's intramolecular non-covalent interactions and intermolecular interactions with water.[29,30] In contrast to this, and similar to iodide, an increase in [KSCN] leads to no apparent disruption of **SGQ-aG'**, as shown by ^{1}H NMR experiments (Figure 2.2b). Differential Scanning Calorimetry and turbidimetry experiments were used to further explore the stability of these SGQs as discussed further ahead.

2.3.2.2 Thermal responsiveness of SGQs

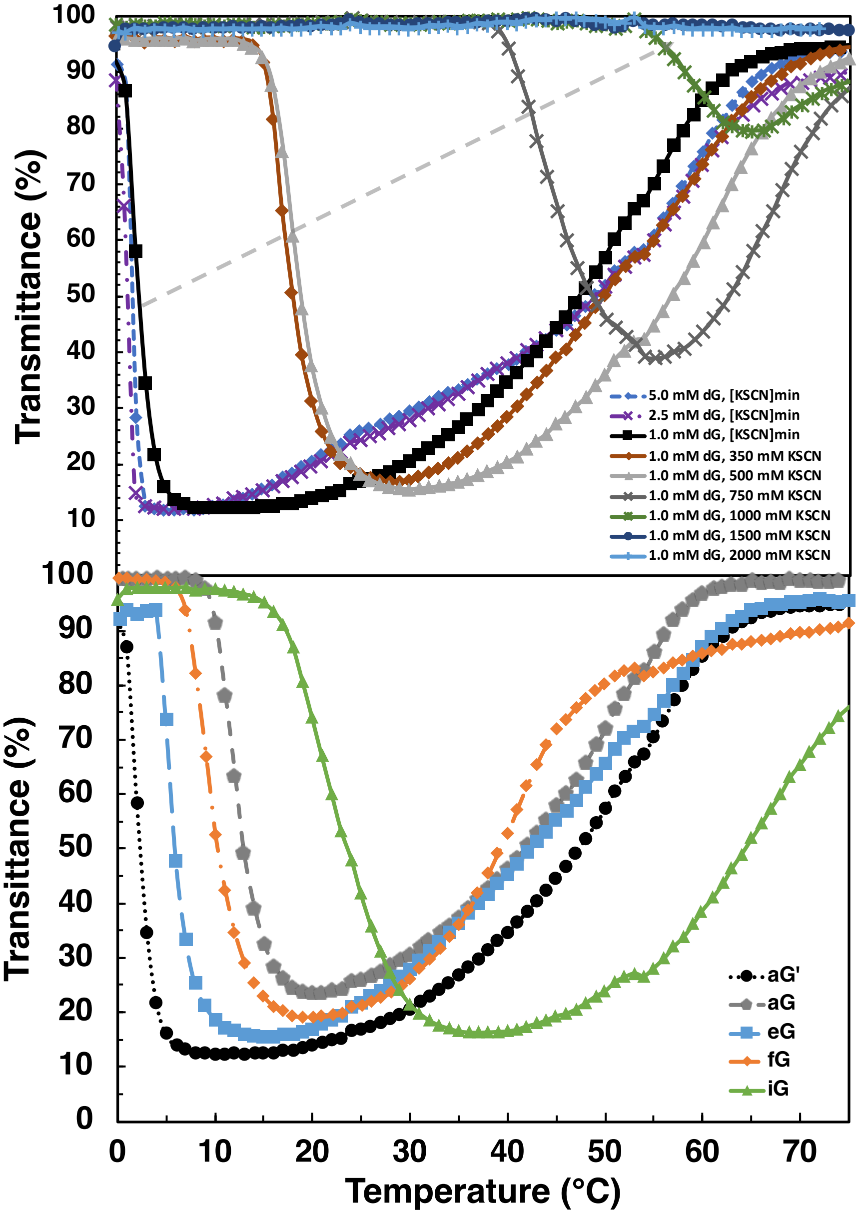

Figure 2.3. Turbidimetry experiments as a function of temperature for various G-derivatives. (a) Turbidimetry experiments for **SGQ-aG’** at $[KSCN]_{min}$ with varying concentrations of **aG’** (5 mM (blue, ◆); 2.5 mM (purple, ×); 1 mM (black, ■) and at constant concentration of **aG’** (1 mM) with varying concentrations of KSCN: 0.350 M (brown, ◆); 0.500 M (gray, ▲); 0.750 M (dark gray, ×); 1.0 M (green, ∗); 1.5 M (blue, ●); 2.0 M (light blue, +). (b) Turbidimetry experiments for SGQs made with various G-derivatives (1 mM) at their corresponding $[KSCN]_{min}$ in PBS, pH 7.4: **aG’** (black, ●), **aG** (gray, ⬟); **eG** (light blue, ■); **fG** (orange, ◆); **iG** (green, ▲). The gray arrow represents the trend in LCST

Since the formation of the SHS particles depends on the thermoresponsive behavior of the corresponding SGQs, we next evaluated this phenomenon by determining the LCST (the threshold for SHS formation) using turbidimetry (determined by the inflection point of the turbidity curve). As the soluble SGQ, forms the particle these solutions become cloudy. The LCST is known to be dependent on the hydrophobicity of the system (an intrinsic parameter) and a specific formulation (an extrinsic parameter).[12,30,43–45]

Therefore, we first determined the LCST at varying concentrations of **aG’** at the corresponding $[\mathrm{KSCN}]_{\mathrm{min}}$ in PBS, pH 7.4 (Figure 2.3a). In the range of 1–5 mM of **aG’**, the LCST remains fairly stable at around 2–1.5 °C with a small tendency towards a lower LCST at higher [**aG’**]. In comparison to the 2.5 and 5.0 mM, the solution of **aG’** at 1 mM remains at a lower transmittance for a broader range of temperature. The lowering of LCST is an expected trend when increasing the solute concentration. The lower LCST is due to its cooperative nature. The entropy in solution is increased as the structuring of the solvent around the solute hydrophilic groups decreases. This disorder is then extended across other structures. As there is a higher concentration of the solute, this behavior is more probable and more facile to expand. The cooperative nature of LCST makes the seen transitions of **aG’** at different concentrations sharper. It keeps the change from a high transmittance to a lower one happening in a shorter range of temperatures.[12,44,46,47]

As we continue to explore the formulation of SGQs, and how this affects the LCST, we dive further into the use of the chaotropic anion thiocyanate anion. Here we look into how the excess of the thiocyanate anion affects the thermoresponsive properties of each SGQ. For these experiments, we studied the turbidity of the SGQ in the temperature range of 2 - 75 °C using 1 mM of G-derivative at either $[KSCN]_{min}$ (Figure 2.3b) or at higher [KSCN] (Table 2.1). The LCST values for range from the lowest for **SGQ-aG’** (~2 °C), to 6 °C for **SGQ-eG,** 10 °C for **SGQ-fG**, 12 °C for **SGQ-aG**, and 21 °C for **SGQ-iG**. As anticipated, an increase the concentration of KSCN results in an increase in the LCST.

Table 2.1. Thermo-responsiveness for SGQs made by various G-derivatives (1 mM) in PBS, pH 7.4 at different [KSCN].

G-derivative	**[KSCN] (M)**	**LCST (° C)**	**UCST (° C)**
aG’	0.2	2	51
	0.35	17	51
	0.5	18	63
	0.75	44	68
	1	59	–
aG	0.05	12	55
	0.162	21	56
	0.215	28	60
	0.3	34	63
	0.35	40	63
eG	0.1	6	57
	0.3	20	67
	0.5	39	71
	0.75	63	–
	1	74	–
fG	0.1	10	42
	0.2	13	53
	0.3	22	–
	0.4	29	–
	0.45	54	–
iG	0.8	21	68
	1	32	75
	1.275	46	–
	1.5	53	–

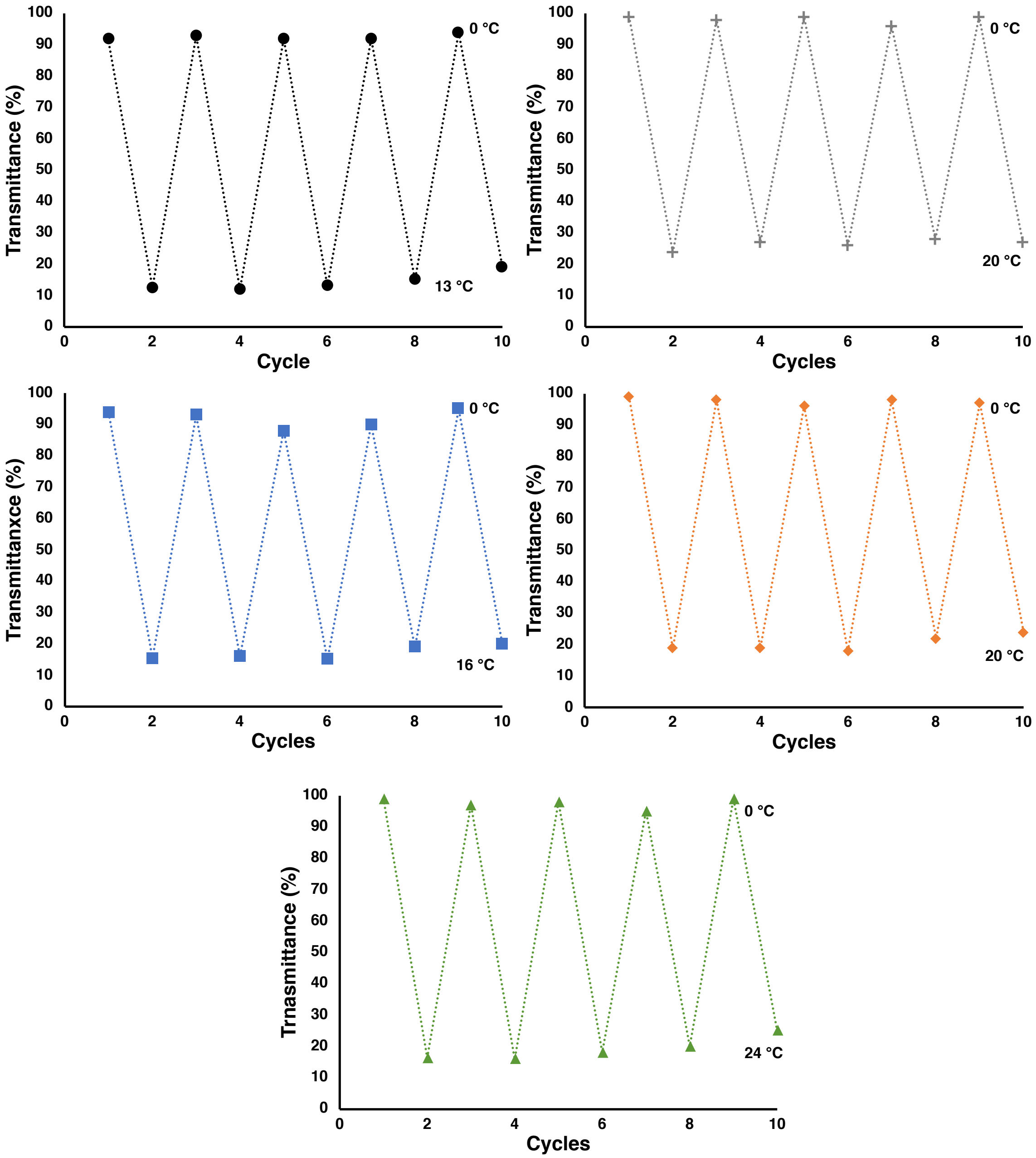

Figure 2.4. Change in transmittance (at 650 nm) for solutions of various G-derivatives. (a) **aG’** ($T_{\min}$ = 0 °C; $T_{\max}$ = 12 °C); (b) **aG** ($T_{\min}$ = 0 °C; $T_{\max}$ = 20 °C); (c) **eG** ($T_{\min}$ = 0 °C; $T_{\max}$ = 16 °C); (d) **fG** ($T_{\min}$ = 0 °C; $T_{\max}$ = 20 °C); (e) **iG** ($T_{\min}$ = 0 °C; $T_{\max}$ = 24 °C). Conditions: All solutions contained G-derivatives (1 mM) dissolved in PBS, pH 7.4 and varying concentrations of KSCN (**aG’**: 200 mM; **aG**: 50 mM; **eG**, **fG**: 100 mM; **iG**: 800 mM).

As each sample with $[\text{KSCN}]_{\min}$ is put through the same cycle 5 times, we see no variations in the LCST or the change in transmittance (Figure 2.4). From this, we can see that all systems show the same behavior in each cycle. The data show that the phase change itself does not compromise the reliability of transition from a single-phase to a two-phase solution. For each experiment, we can also see the disappearance of this turbidity after the transition, with varying temperatures for different SGQ structures. The reversibility of the system helps us understand that this may be a process of SHS particles dissolving into the SGQ due to the high input of heat. Yet as the SHS particles redissolves into solution, we can identify that these solutions not only show an LCST but also show an UCST (Table 2.1). With this information, we were able to build a global phase diagram (Figure 2.5). This phase diagram shows the highest UCST and lowest LCST, depending on the concentration of KSCN.

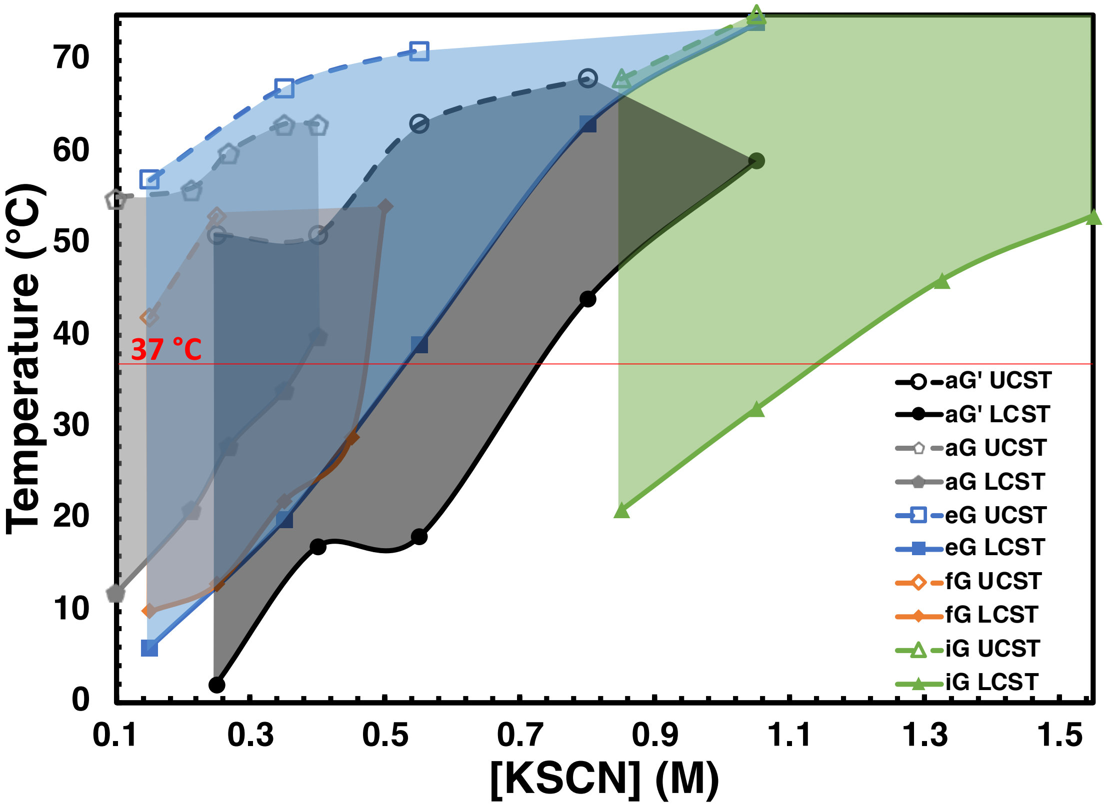

Figure 2.5. Phase diagram of 1 mM of G-derivatives depending on KCSN (M) in PBS 1X. The LCST and UCST were calculated by using the inflection points of the transmittance curves. Shaded area illustrates where SHS particles can be found in solution per G-derivative. The LCST and UCST transitions are represented by solid, and dashed lines, respectively. Shaded area shows which regions SHS are present in dependance of [KSCN] and temperature. Each data point represented as follows: The data points are represented as follows: **aG’** (black, ●), **aG** (gray, ⬟); **eG** (blue, ■); **fG** (orange, ◆); **iG** (green, ▲).

As previously mentioned, the LCST depends on a system’s hydrophobicity and formulation.[16] These entropy-driven process change the energy that is needed for an SGQ to expel water molecules in its hydration shell. Using this mechanism, these SGQ conglomerate and form SHS particles. On the other hand, UCST depends primarily on enthalpic considerations.[16] Both properties can be tunable when changing the parameters of the solution. As higher concentration of the G derivative shows a sharper LCST transition, a higher concentration of KSCN modulates where both LCST and UCST are seen for each system.

2.3.3. SHS Particle Characterization

2.3.3.1 SHS Particles Thermal Response

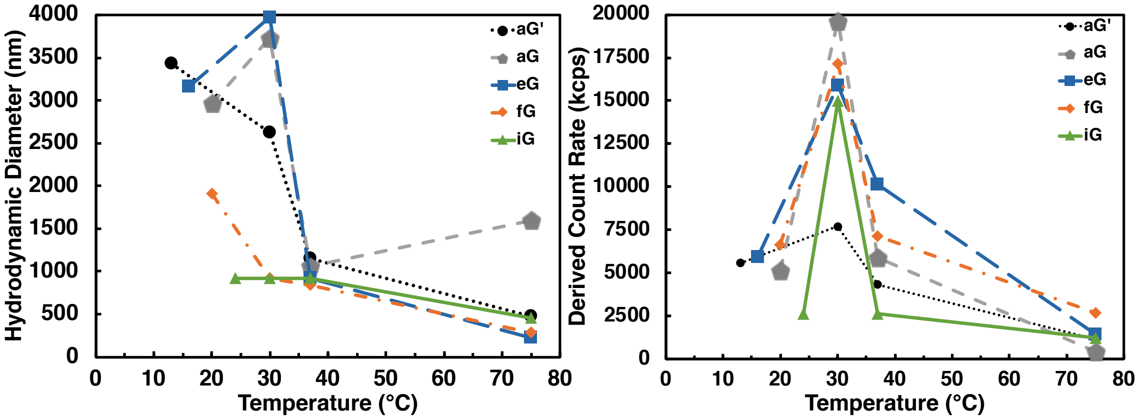

Figure 2.6. DLS measurements as a function of temperature. a) Average hydrodynamic diameter (D_H) and b) derived count rate (DCR) for: **aG'** (black, ●), T_{cp} = 13 °C; **aG** (gray, ⬟), T_{cp} = 20 °C; **eG** (light blue, ■), T_{cp} = 16 °C; **fG** (orange, ◆), T_{cp} = 20 °C; **iG** (green, ▲), T_{cp} = 24 °C. Conditions: All solutions contained G-derivatives (1 mM) dissolved in PBS, pH 7.4 at $[KSCN]_{min}$.

Dynamic light scattering (DLS) was used to characterize all SHS particles. We used this technique to characterize the hydrodynamic diameter (D_H) of the SHS particles and to quantify the corresponding populations via derived count rate (DCR) measurements. To execute this, we used different temperatures at the clouding temperature (T_{cp}) where the transmittance was the lowest, as shown in Figure 2.9b, at 30 °C, 37 °C, and 75 °C (Figure 2.6). These measurements help us understand: the mechanism of the formation of SHS particles, an insight of morphology and population of the SHS particles in a biologically relevant environment, and what is happening in the solution after UCST.

By comparing the D_H measurements at T_{cp} and at 30 °C, we can see that **aG** and **eG** based SHS (**SHS-aG** and **SHS-eG**) particles increase its D_H, while **SHS-aG'** and **SHS-fG** particles decreased D_H and **SHS-iG** stays in the same range (Figure 2.6a). Confocal images of SHS particles (at 30 °C) are shown in the Figure 2.7. Yet all SHS particles population has dramatically increased by 30 °C (Figure 2.6b). Comparing the data from 30 °C and 37 °C both D_H and population have decreased for all SHS particles. When examining the data from 37 °C and 75 °C, all populations decline. All SHS particles decrease in size but **SHS-aG** particles in transitioning from 37 °C to 75 °C.

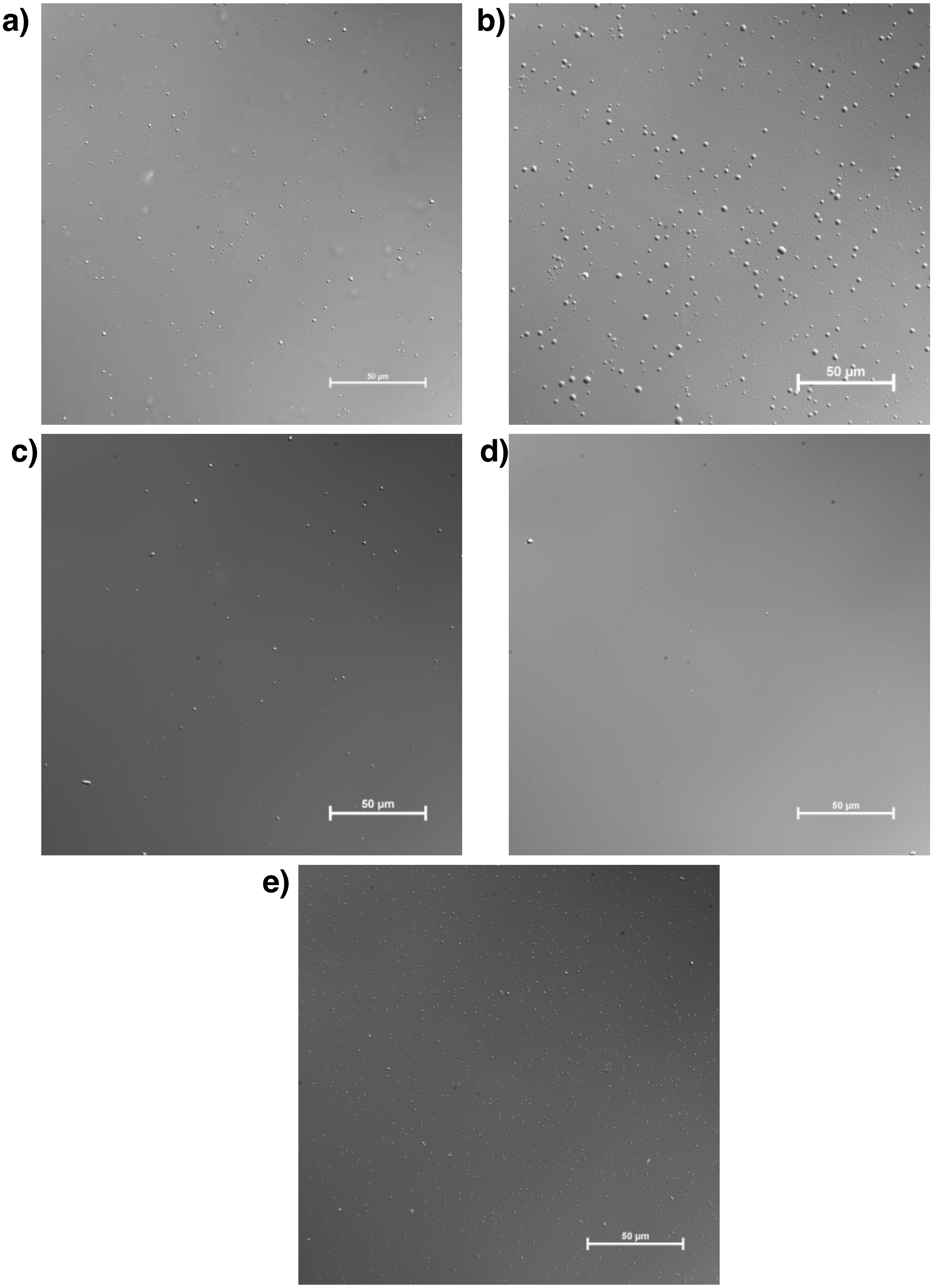

Figure 2.7. Confocal microscopy images of SHS particles made from: a) **aG’,** b) **aG,** c) **eG**, d) **fG**, and e) **iG**. Conditions: G-derivatives (1 mM) dissolved in PBS, pH 7.4 with $[KSCN]_{min}$ at 30 °C.

Using the previously described trends, we can understand SHS particle formation mechanisms and UCST behaviors. At T_{cp}, not all SGQ structures have transitioned into SHS particles when compared to the data at 30 °C, as all solutions increase the SHS particle population. Within this range, the data suggests that there is a threshold of SHS particle size dependent on G-derivative structure or [KSCN].[48] Here we can notice than three of the SHS (**SHS-a'**, **-a**, **-e**) are over the 2 μm. Although these systems are at a micron scale, previous data shows internalization of SHS particles above 1 μm into SH-SY5Y cells through the macropinocytosis mechanism.[31,49] As the temperature is further increased to 37 °C all SHS particles, regardless of G-derivative, behave similarly. At 37 °C as all SHS populations decrease, these share similar D_H decrease of 1 μm. Above the UCST threshold (at 75 °C), with the exception of **SHS-aG**, the D_H for all other SHS particles decrease. The D_H decrease is concurrent with previously reported SHS going through dehydration.[50] The behavior of **SHS-aG** is consistent with an Ostwald ripening effect. As we notice fewer particles at 75 °C, the SHS in solution has become larger. Ostwald ripening consists of smaller particles shrinking. This is the result of the diffusion of smaller particles into the larger particles.[51] The SHS particles formed by the other derivatives, in contrast, do not show a similar increase in particle size, which may indicate a full dissolution of the constituent G-derivatives at such high temperatures.

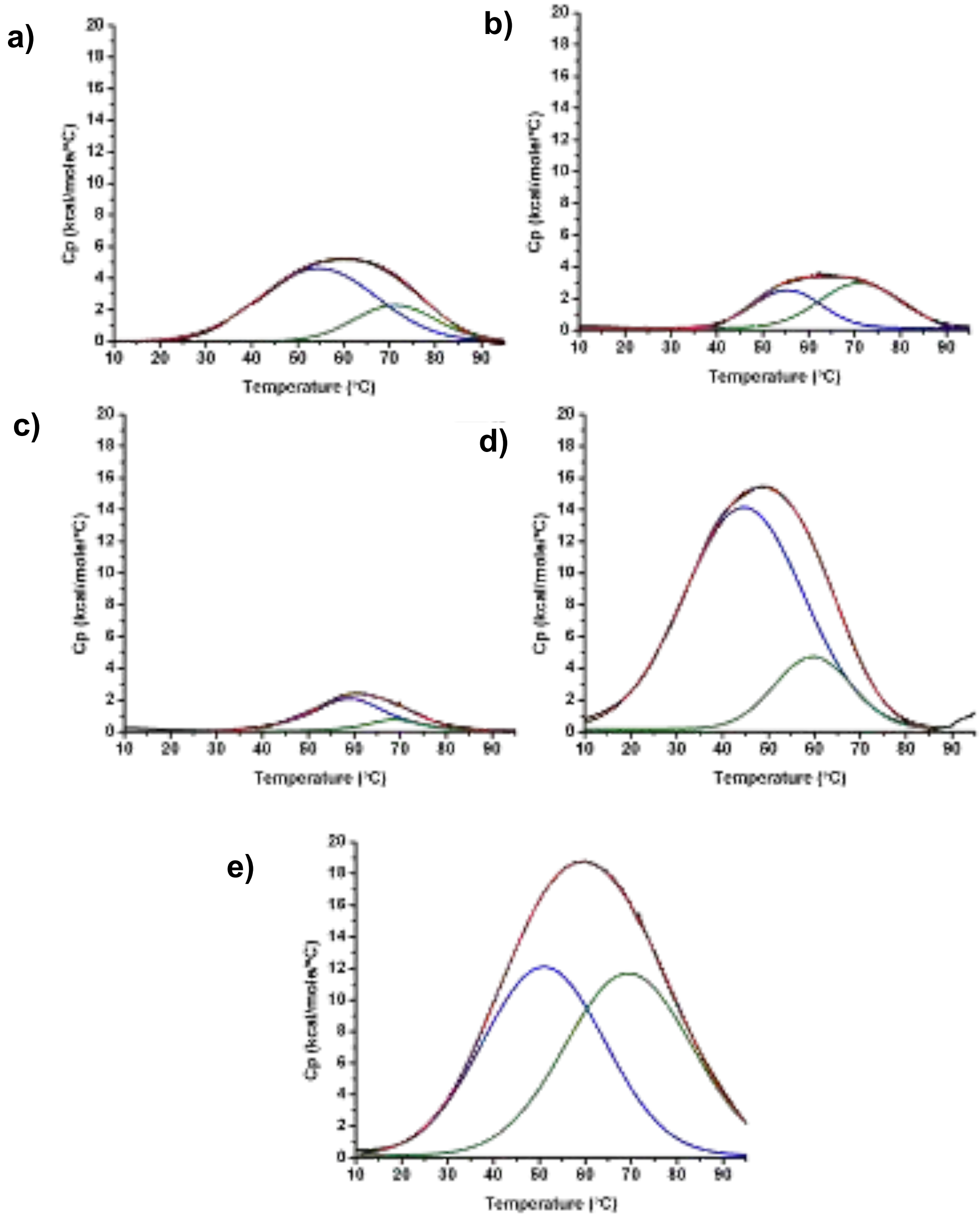

Figure 2.8. DSC traces for solutions of G-derivatives at $[KSCN]_{min}$: a) **aG'**, b) **aG,** c) **eG**, d) **fG**, e) **iG**. The DSC endotherms are represented by a red line. The blue and green deconvolution peaks correspond to, respectively, the LCST process, and the thermally-induced dissociation of the SGQ structures (i.e., T_m). Conditions: All solutions were 1 mM in the G-derivative dissolved into PBS, pH 7.4.

Differential scanning calorimetry (DSC) measurements (Figure 2.8) reveals an endothermic process. Data deconvolution allows showing two main curves, each showing a different thermodynamic process. As we know, the SGQ has a thermal response, which we identify as the SGQ going through its LCST to form the SHS. In the DSC data, we can see the SHS formation temperature (T_M) represented by the first deconvoluted curve (blue), which overlaps with a second curve (red). As we defined LCST as the inflection point of the fist change in the transmittance studies, the T_M is where we can expect the formation of all SHS. The hydration shell disruption allows the formation of the SHS. This curve shows this entropically favored endothermic process. Therefore, the LCST and T_M will not always coincide, as we have previously reported.[27,52] The second curve is produced by the melting point (T_m) of the SGQ. Regardless of G-derivative at 75 °C, all SGQ structures are at or close to T_m, as previously reported.[27,52] The thermodynamic values can be seen in Table 2.2.

The overlapping of the SHS formation and SGQ melting curves validates our understanding of the UCST. We can see that above 37 °C, we can start to see the SGQ melting curve regardless of the G derivative system. The disassembly of SGQ forces the SHS in solution to disassemble. Therefore, allowing the enthalpic process of UCST to take place.

Table 2.2. Summary of the data DSC data.

G-derivative	**T_M (°C)**	**ΔH_{cal} (T_M) (kcal/mol)**	**T_m (°C)**	**ΔH_{cal} (T_m) (kcal/mol)**
aG’	54.53 ± 0.03	4.6 ± 0.3	71.21 ± 0.02	2.2 ± 0.3
aG	55.30 ± 0.02	2.5 ± 0.1	71.04 ± 0.02	3.0 ± 0.3
eG	58.96 ± 0.02	2.1 ± 0.1	68.65 ± 0.02	0.780 ± 0.002
fG	44.67 ± 0.02	14.1 ± 0.3	59.75 ± 0.01	4.7 ± 0.1
iG	50.97 ± 0.02	12.1 ± 0.1	69.39 ± 0.02	11.6 ± 0.2

2.3.3.2 SHS particle fixing

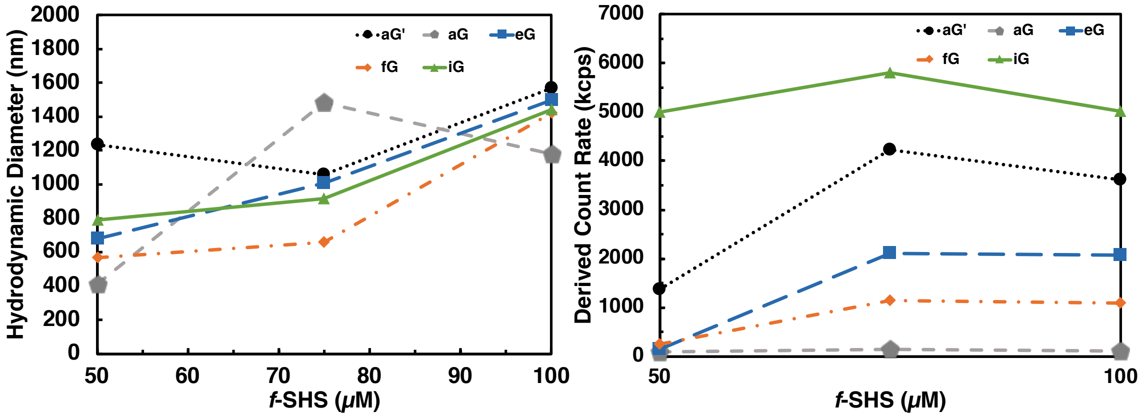

Figure 2.9. DLS measurements as a function of concentration for *f*-SHS particles in PBS, pH 7.4 at 37 °C. a) Average hydrodynamic diameter (D_H) and b) derived count rate (DCR) for: ***f*-SHS-aG’** (black, ●), T_{cp} = 13 °C; ***f*-SHS-aG** (gray, ⬟), T_{cp} = 20 °C; ***f*-SHS-eG** (light blue, ■), T_{cp} = 16 °C; ***f*-SHS-fG** (orange, ◆), T_{cp} = 20 °C; ***f*-SHS-iG** (green, ▲), T_{cp} = 24 °C. Conditions: All solutions contained G-derivatives (1 mM) dissolved in PBS, pH 7.4 at $[KSCN]_{min}$.

To continue the characterization of SHS particles, we decided to study these by lowering the ionic strength in solution. This process kinetically stabilizes the SHS particles in solution, which prevents their dissolution back to the constituent SGQ structures.[31,53,54] We diluted the initial solutions of SHS particles to with [KSCN]$_{\text{min}}$ to 50, 75, and 100 µM of SHS particles at 37 °C (Figure 2.9). At 100 µM, the populations of the *f*-SHS particles varied their average D_H in the range of 2 to 5 µm and 0.5 – 1.5 µm (Figure 2.9a) with DCR values in the range of 70 – 4000 kcps (Figure 2.9b). Using *f*-SHS particles concentrations of 50 and 75 µM, all G-derivative populations were uniform in terms of size within each G-derivative *f*-SHS particle (Figure 2.9a). The population at 50 µM of all *f*-SHS particles regardless of G-derivative was at considerably low, with ***f*-SHS-aG'** particle being the highest at 1236 kcps (Figure 2.9b). All G-derivatives showed the highest population at 75 µM of *f*-SHS particles. To visualize and study further their morphology of *f*-SHS particles, we did confocal microscopy of all samples at 75 µM of SHS particles (Figure 2.10). These are all spherical and oval shapes, as previously reported data.[31,53] Size measurements done in the confocal microscope concur with DLS data.

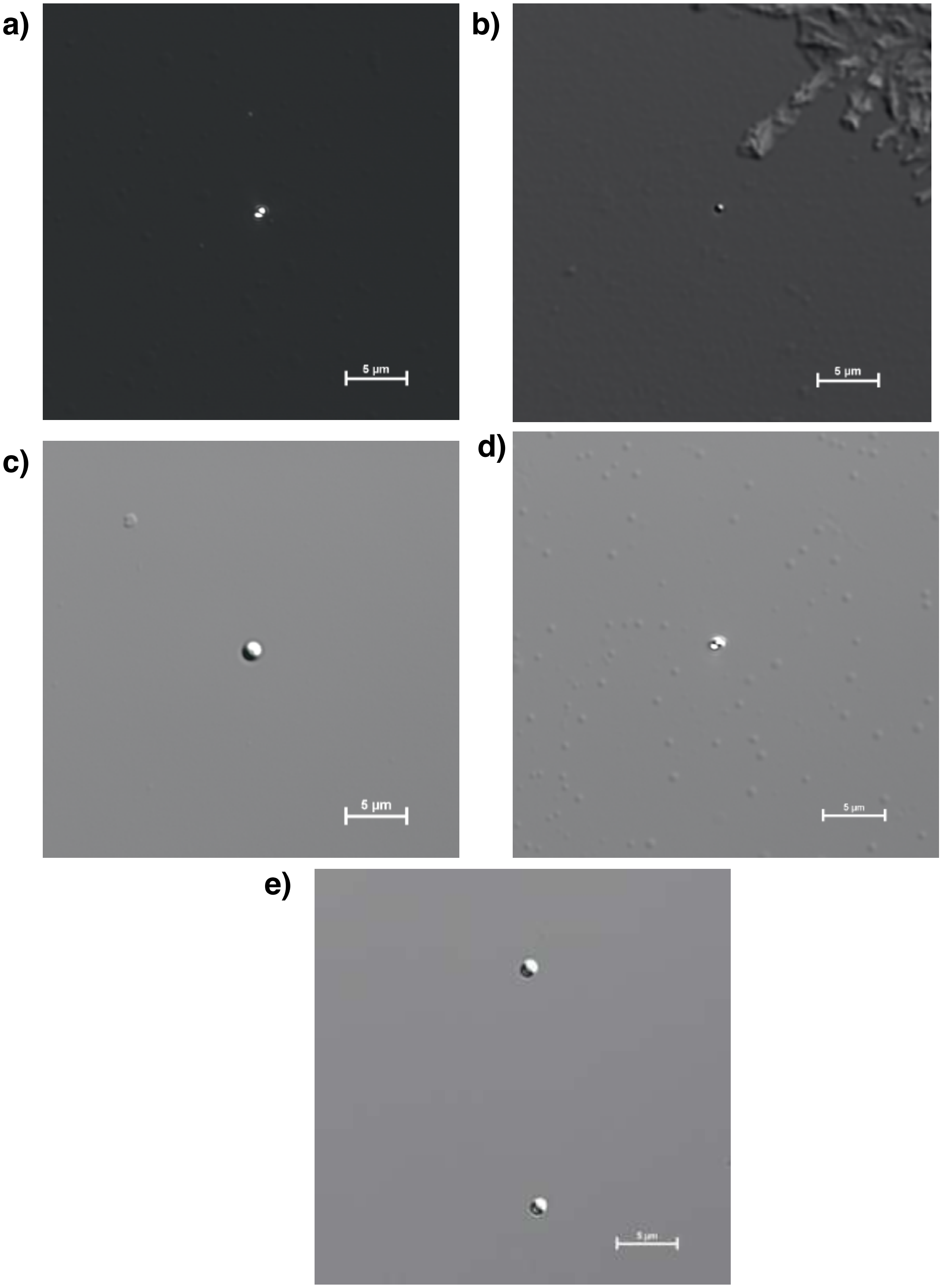

Figure 2.10. Confocal microscopy experiments for *f*-SHS (75 µM): a) **aG’** with 15.00 mM of KSCN. b) **aG** with 3.75 mM of KSCN. c) **eG** with 7.50 mM of KSCN. d) **fG** with 7.50 mM of KSCN. e) **iG** with 60.00 mM of KSCN. Conditions: all solutions were in PBS, pH 7.4 at 37 °C.

An essential element of the reversibility between the SGQ and SHS particles is that the solution conditions used to assist the self-assembly, in particular the presence of the salts used to enhance the dissolution of the G-derivatives (e.g., KSCN).[31,48,53,54] As previously explained, the cation organizes the SGQ, but the chaotropic anions is the one that facilitate the SGQ-water interactions. By taking an SHS aliquote and diluting it we lower the concentrations of the salts. Low concentrations of chaotropic anions hinder attractive interactions between SGQs and water, favoring the SGQ-SGQ interactions within the SHS particles, which in turn preclude their dissolution. At a particle concentration of 100 μM, there is a lower abundance of particles relative to 75 μM. The SHS D_H at a particle concentration of 100 μM shows an average of 1400 nm. D_H shows an average of 700 nm at a particle concentration of 75 μM. Particles based on **aG** at 100 μM particle concentration resulting in smaller particles than 75 μM particle concentration. This environment of SHS tends to promote an Ostwald ripening effect, previously discussed.[51,55,56] At 50 μM, clustering becomes entropically unfavorable, leading to dissolution via diffusion of the particles[51,57] The most hydrophobic G-derivatives (i.e., **aG’** and **iG**) show the largest particle populations across the board. A balance between the [KSCN] effects and the hydrophobicity G-derivatives seem to result in homogeneous populations not affecting the abundance of the *f*-SHS particles in solution

Table 2.3. Summary of the data for the SHS made from the G-derivatives reported in this chapter.

G-derivative	$[\mathrm{KSCN}]_{\mathrm{min}}$ (mM)	LCST (°C)	T_{cp} (°C)	D_H (nm)				
				T_{cp}	30 °C	37 °C	75 °C	*f*-SHS (75 μM)
aG’	200	2	13	3432	2622	1155	479	1060
aG	50	12	20	2966	3736	1061	1593	1483
eG	100	6	16	3158	3974	916	225	1009
fG	100	10	20	1908	917	843	283	658
iG	800	21	24	916	917	916	451	917

D_H = Hydrodynamic diameter

2.4. Conclusions

Here we have successfully designed and studied a new library of stable particles in biologically relevant environments at low salt concentrations and biorelevant temperatures. As we explore different G-derivatives, we can point out discoveries in the behavior of their corresponding SGQ structures. Because these are supramolecular structures, we evaluated intrinsic (i.e., structural) and extrinsic parameters to formulate SHS particles. The intrinsic parameters of each G-derivative (e.g., sugar ester side chain length, C8-*meta*-carbonylphenyl modifications) play a role in the solvation. We showed the chaotropic thiocyanate anion leads to a salting-in process that resulted in a fourfold lower salt concentration needed to dissolve for **aG** relative to **aG’**. In turn, derivative **aG’** uses a fourth of the KSCN required for **iG** to self-assemble. Although it has the same alkyl chain at the ester groups attached to the sugar moiety of **aG** dendron, the vinyl-imidazole moiety appears to have a greater influence in solvation and self-assembly. In cases like these, the presence of a chaotropic anion becomes critical because of the greater hydrophobicity of the G-derivatives.

At [KSCN]$_{\text{min}}$ all the SGQ structures evaluated in this chapter have an LCST below room temperature, but the T_{cp} can be increased to higher temperatures by increasing the concentration of KSCN. We confirmed that, like for previous studies, the process is reversible and the T_{cp} remains constant even after going through multiple heating-cooling cycles. We also expanded our understanding of the UCST of these systems, a phenomenon we have observed previously, but one we have not evaluated systematically.[27,50] This enabled the construction of an LCST-UCST phase diagram as a function of [KSCN], which provides a map for the conditions where a given SHS particle can be produced in order to tailor them for specific applications.[58]

We fixed these particles into *f*-SHS by lowering the ionic strength of the solution, which locks the SHS particle in this state due to insufficient thiocyanate to promote the salting-in of the constituent SGQs. Derivatives as **aG** are able to assemble *f*-SHS at a final [KSCN] of 3.75 mM at 37 °C. The final concentration ***f*-SHS-aG** falls within the range of 3.5 – 5.2 mM K^+ in plasma.[28] Although the SHS particles start forming at or near the T_{cp}, the population increases at 30 °C, finally stabilizing at 37 °C. We took advantage of the larger populations at 30 °C to prepare *f*-SHS particles demonstrating variations in average sizes as a function of the specific G-derivative used. Understanding that these particles are stable in biorelevant environments, we can now evaluate them for further development as stimuli-responsive systems. As we further develop SHS, we may use them in areas such as biological imaging, drug delivery, or vaccine development.[59]

2.5. Experimental Procedures

2.5.1. Reagents

The (3-formylphenyl)boronic acid was purchased from COMBI-BLOCKS. Silica gel 60, 0.04-0.063 mm and TLC plates with EMD silica gel 60 F254 glass-backed from Sorbent Technologies. Visualization in TLC plated was done using UV light and iodine. Phosphate buffered saline (PBS) solutions was purchased from Fisher Scientific as PBS-1X. All other reagents were also from commercial sources and used without further purification.

2.5.2. Synthesis of G-derivatives

Derivative **aG’** and dendron synthesis followed as published in 2015 to a final field of .[27] G-derivatives **aG**, **eG**, and **fG** were synthesized (esterification, nucleophilic substitution, and click reaction followed as previously published) using the methodology described by us.[26,31] For the **fG** derivative, bromination reaction and Suzuki-Miyaura cross-coupling were done as previously reported with the corresponding boronic acid.[33] Derivative **iG** was prepared as previously reported.[26,32]

Table 2.4. Percent yields obtained for each previously reported dG per preformed reaction.

Final dG	Suzuki-Miyaura	Steglich	S_N2	Click	Claisen Schmidt
aG’	82 %	57 %	80 %	72 %	-
aG	-	62 %	87 %	69 %	-
eG	75 %	50 %	85 %	75 %	-
iG	-	-	-	-	65 %

Allylic Bromination reaction to 2’-deoxyguanosine results in an 86 % yield.

*2.5.2.1. Synthesis of **mFGC5Br***

To a 2-neck round bottom flask dried under vacuum the *meta*-formyl-2'-deoxyguanosine (**mFG**), 5-bromovaleric acid (3.5 equiv), DCC (3.5 equiv) and DMAP (1 equiv) were added followed by addition of dry DCM (for a concentration of **mFG** of 64.9 mM) via syringe and the solution was left stirring for 8-12 hours under an inert atmosphere. After filtering the urea and rotoevaporation of the DCM, the mixture was then left for 12 h at 2 °C to promote the precipitation of any remaining urea, which was subsequently filtered out. The crude reaction mixture was then dry-loaded into silica gel and left drying under vacuum (12 h) before purification by flash chromatography using DCM:MeOH (using a gradient mobile phase starting at 0% of MeOH followed by increments of 2% up to 6%). R_f = 0.65 (DCM:MeOH 9:1); yield 55%. δ 10.84 (s, 1H), 10.10 (s, 1H), 8.18 (s, 1H), 8.04 (d, *J* = 7.8, 1.4 Hz, 1H), 7.97 (d, *J* = 7.7, 1.4 Hz, 1H), 7.78 (t, *J* = 7.7 Hz, 1H), 6.52 (s, 2H), 6.12 (t, *J* = 6.9 Hz, 1H), 5.45 (dt, *J* = 7.3, 3.6 Hz, 1H), 4.45 (dd, *J* = 11.6, 4.8 Hz, 1H), 4.29 (dd, *J* = 11.6, 7.3 Hz, 1H), 4.18 (dt, *J* = 7.8, 4.1 Hz, 1H), 3.59 – 3.53 (m, 1H), 3.50 (q, *J* = 6.7 Hz, 4H), 2.40 (dt, *J* = 6.9, 3.5 Hz, 1H), 2.35 (q, 4H), 1.79 (dq, *J* = 15.4, 6.8 Hz, 4H), 1.62 (h, *J* = 7.7 Hz, 4H). δ 192.51, 172.08, 171.87, 156.26, 152.82, 151.65, 145.35, 136.10, 130.57, 116.86, 84.36, 81.43, 74.40, 63.30, 34.27, 32.01, 31.00, 22.60. IR (ν_{max}/cm^{-1}): 3842.05, 3737.842, 1847.964, 1847.088, 1818.07, 1794.538, 1778.303, 1740.332, 1678.761, 1634.48, 1488.731, 1266.088, 1248.244, 1217.322, 671.504. MS: ESI-MS [M + Na]$^+$ 708.06 m/z

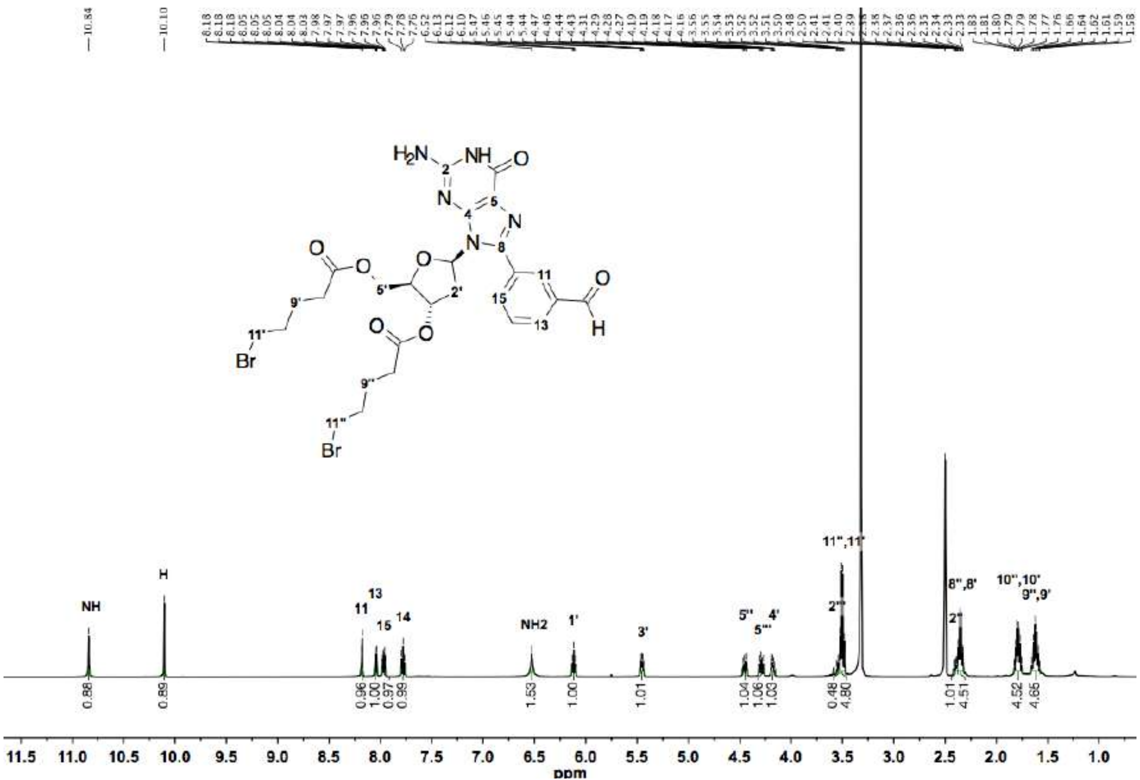

Figure 2.11. **mFGC$_5$Br** ^{1}H NMR (500 MHz, DMSO-d_6, 298.1 K)

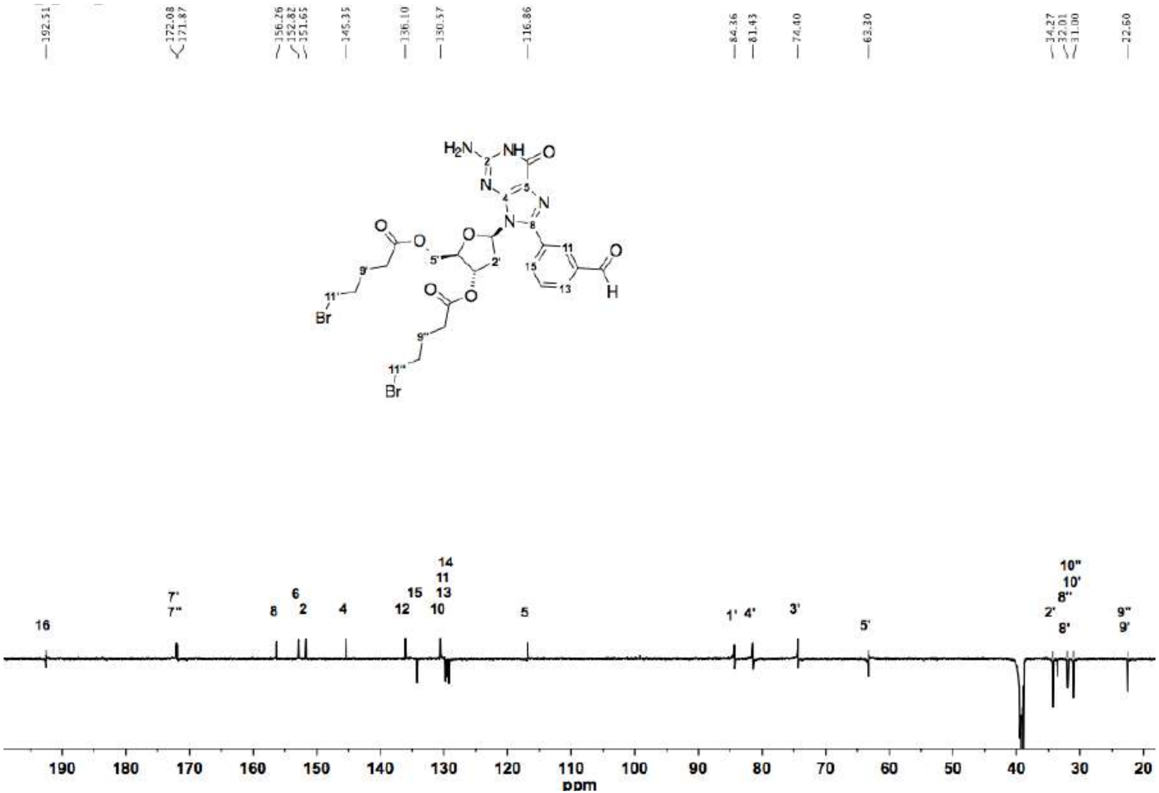

Figure 2.12. **mFGC$_5$Br** ^{13}C (APT) NMR (176 MHz, DMSO-d_6, 298.1 K)

*2.5.2.2. Synthesis of **mFGC$_5$N$_3$***

Synthesis is done by adding the **mFGC$_5$Br** into a vial with NaN$_3$ (4 eq.) and DMF for a concentration of 56.2 mM of **mFGC$_5$Br**. This is stirring for 12 hours at 80 °C. Sample then is dried and washed with distilled water to eliminate excess of NaN$_3$ and side products. Yield of 92%. δ 11.11 (s, 1H), 10.10 (s, 1H), 8.18 (s, 1H), 8.04 (d, *J* = 7.6 Hz, 1H), 7.97 (d, *J* = 7.7 Hz, 1H), 7.78 (t, *J* = 7.7 Hz, 1H), 6.61 (s, 2H), 6.12 (t, *J* = 7.0 Hz, 1H), 5.47 – 5.43 (m, 1H), 4.46 (dd, *J* = 11.6, 4.9 Hz, 1H), 4.29 (dd, *J* = 4.3 Hz, 1H), 4.21 – 4.15 (m, 1H), 3.60 – 3.49 (m, 2H), 2.42 – 2.37 (m, 1H), 2.35 (q, *J* = 7.0, 6.5 Hz, 7H), 1.60 – 1.47 (m, 9H). δ 192.87, 172.52, 172.30, 152.19, 145.55, 136.48, 131.08, 117.28, 84.77, 81.82, 74.81, 63.62, 33.85, 32.79, 32.68, 27.55, 21.67, 21.51. IR (v_{max}/cm^{-1}): 1818.084, 1678.335, 2203.397, 2205.697, 1268.749, 1740.241, 1114.623, 1794.666, 1778.29, 3737.688, 1849.316, 1488.477, 1846.903, 672.058. MS: ESI-MS [M + Na]$^+$ 633.24 m/z

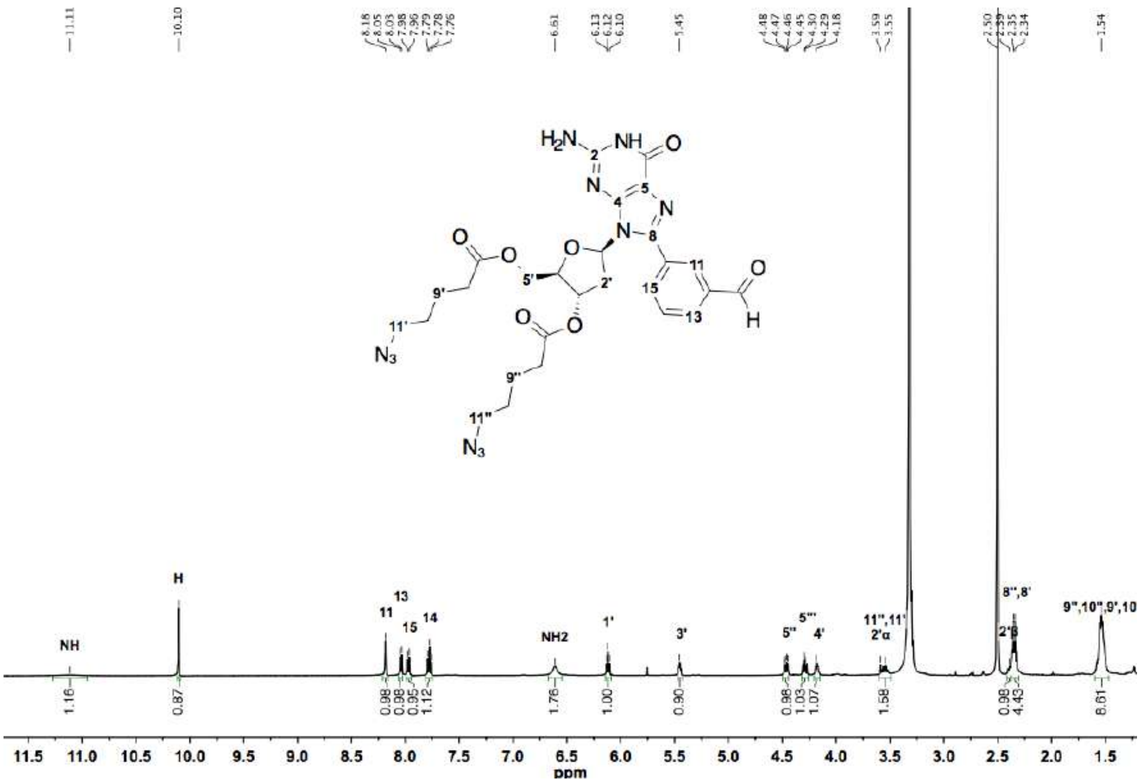

Figure 2.13. **mFGC$_5$N$_3$** ^{1}H NMR (500 MHz, DMSO-*d$_6$*, 298.1 K)

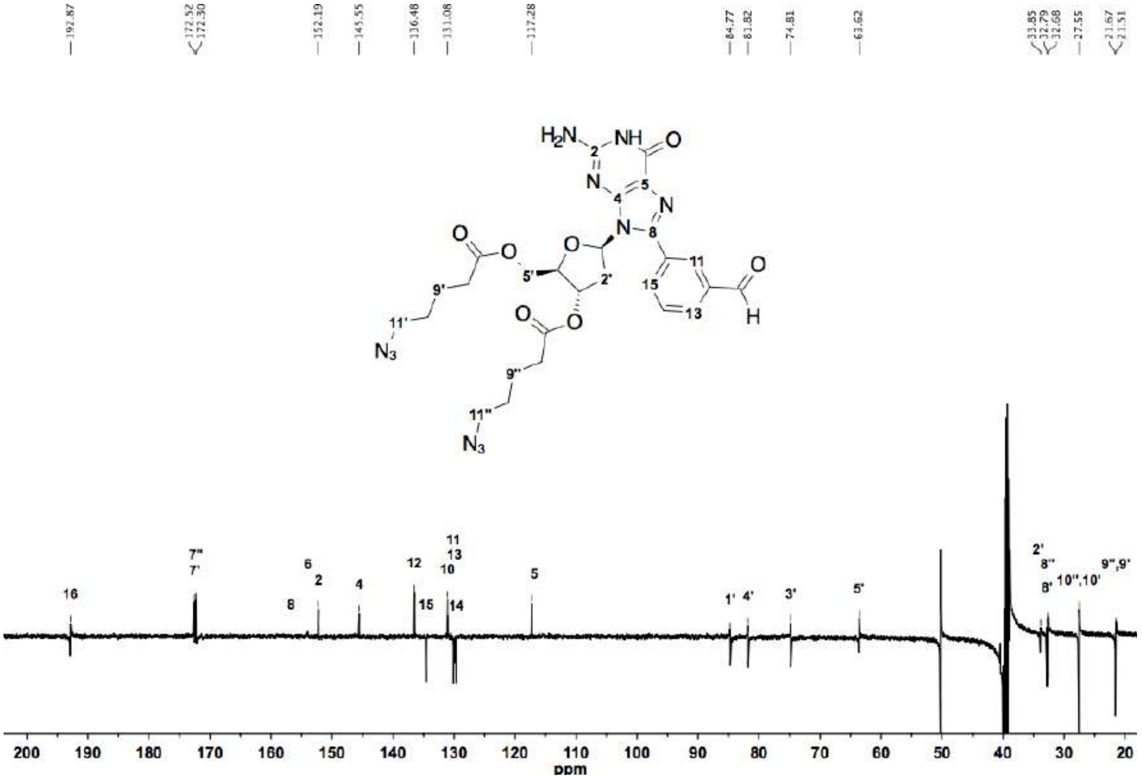

Figure 2.14. **mFGC$_5$N$_3$** ^{13}C (APT) NMR (126 MHz, DMSO-*d$_6$*, 2980.1 K)

*2.5.2.3. Synthesis of **fG** (also referred to as **mFGC$_5$D2OH**)*

mFGC$_5$N$_3$ (0.17 mmol) is added to a vial with D2OH (4 equiv), sodium ascorbate (0.6 eq), copper solution $CuSO_3 \cdot 5H_2O$ of 0.1 M (0.36 mL), and 4.37 mL of THF:D_2O (3:1). This is stirring with a stirring bar for 2 to 4 hours. The mixture is dried with silica gel and left drying in vacuum for over 12 hours. A column chromatography is then used to separate the mixture using EtOAc:DCM (1:1) with MeOH starting at a mixture of 0% of MeOH to 5%, 10%, 12.5%, 15% at 20%. Rf = 0.55 on TLC plates with a mobile phase of EtOAc:DCM:MeOH (4:4:1). Yield of 75%. δ 10.87 (s, 1H), 10.10 (s, 1H), 8.17 (s, 1H), 8.06 (s, 2H), 8.04 (d, J = 7.6 Hz, 1H), 7.96 (d, J = 7.5 Hz, 1H), 7.77 (t, 1H), 6.54 (s, 2H), 6.11 (t, 1H), 5.46 – 5.42 (m, 1H), 5.09 (s, 4H), 4.68 (s, 4H), 4.45 – 4.42 (m, 1H), 4.36 – 4.30 (m, 4H), 4.28 – 4.24 (m, 1H), 4.17 (s, 1H), 3.49 (d, J = 10.2 Hz, 3H), 3.41 (d, J = 8.6 Hz, 2H), 2.34 (s, 6H), 1.80 (s, 4H), 1.46 (s, 4H), 1.03 (s, 6H). δ 192.87, 174.47, 172.41, 172.22, 156.64, 153.22, 152.00, 145.71, 142.22, 136.46, 134.52, 130.94, 129.98, 129.62, 124.07, 84.69, 81.81, 74.72, 63.78, 57.30, 50.27, 48.96, 39.02, 34.07, 32.54, 21.15, 16.80. IR (v_{max}/cm^{-1}): 3311, 3124, 2945, 1726, 1689, 1600, 1454, 1369, 1170, 1124, 1033, 804, 783, 703. MS: ESI-MS $[M + Na]^+$ 977.39 m/z

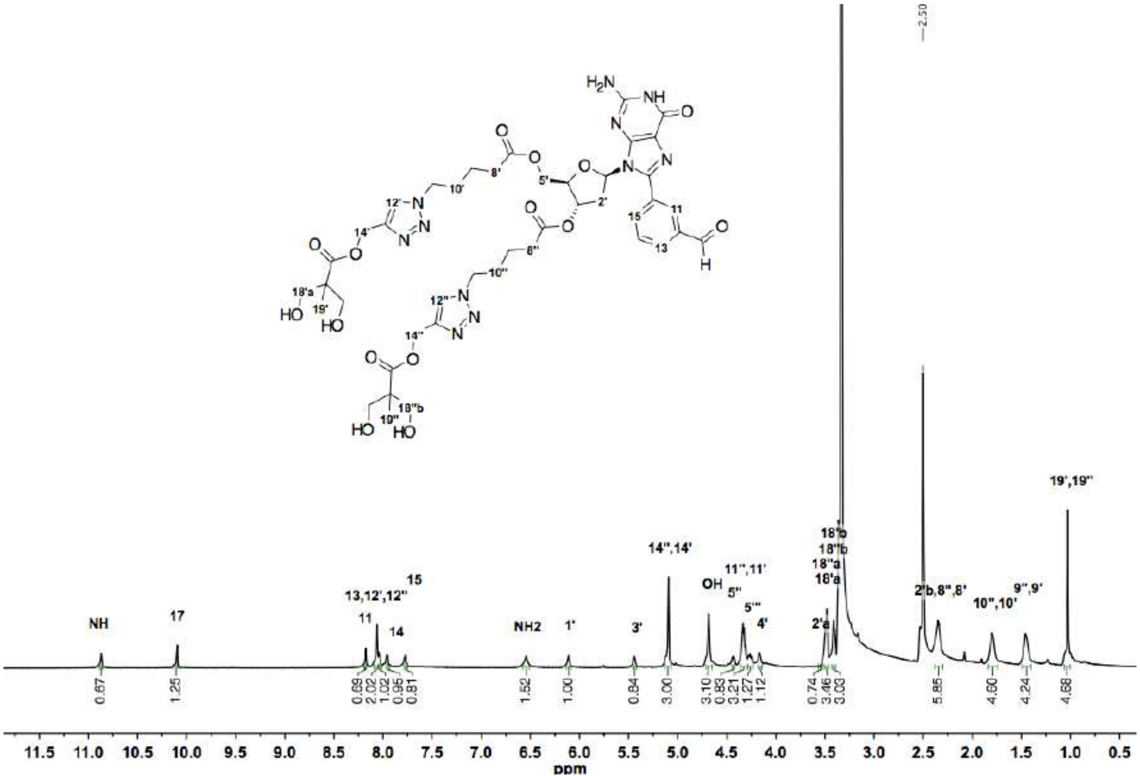

Figure 2.15. **fG** ^{1}H NMR (700 MHz, DMSO-d_6, 298.1 K)

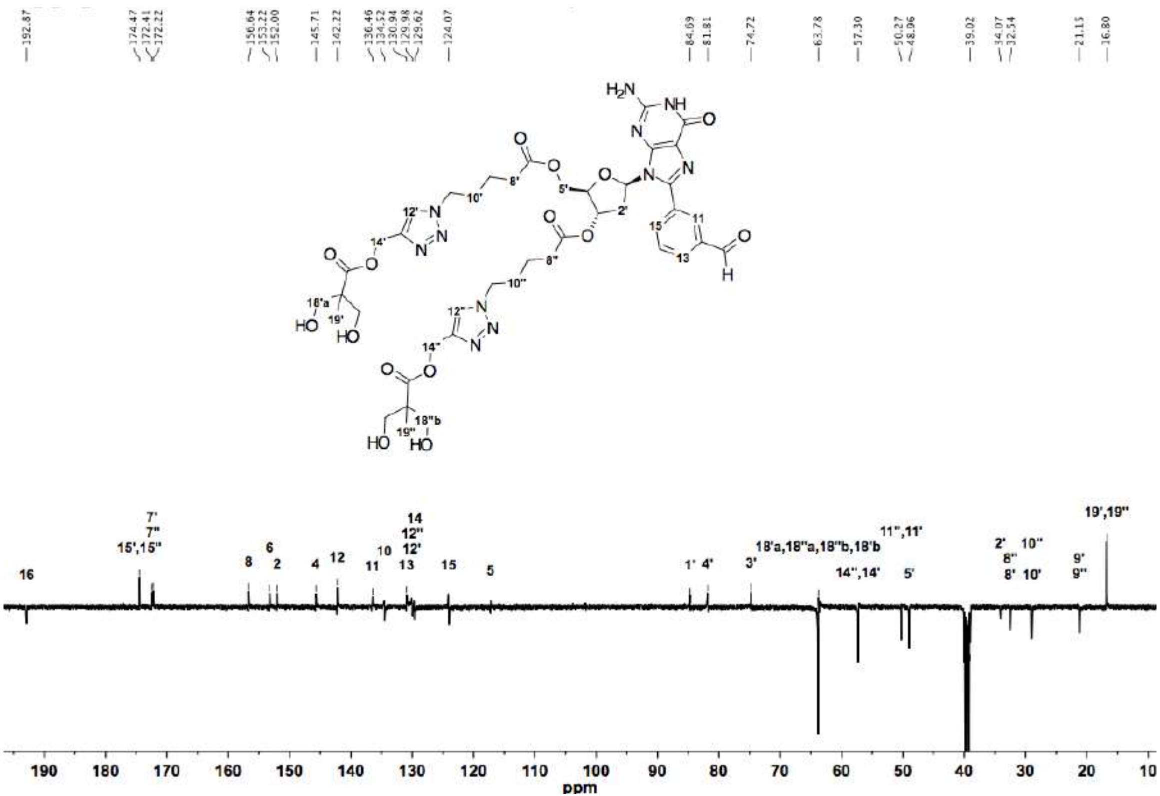

Figure 2.16. **fG** ^{13}C (APT) NMR (126 MHz, DMSO-d_6, 298.2 K)

2.5.3. Salting-in experiments

Salting-in experiments were done by measuring the absorbance of a solution of 1 mM of the G-derivative in PBS, pH 7.4 with increments of salt KSCN at 2 °C in a Cary temperature controller UV-Vis spectrophotometer Varian instrument (Cary Bio-100) at the UPR's MSRC.

2.5.4. Protocols for the preparation of SGQ solutions

The KSCN was added from a 14 M solution in distilled water for the desired concentration for a final volume of 1 mL. Then, water evaporated in an oven for 60 °C for over 12 hr. Then, the corresponding G-derivative was added from a MeOH solution for a final concentration of 1 mM in 1 mL to the KSCN. Then the MeOH was evaporated in an oven at 35 °C for 12 hr. Then 1 mL of PBS, pH 7.4 was added and let for over 12 hr at 2 °C for the SGQ to stabilize. This procedure was done to establish the exact amount of the desired G-derivative.

2.5.5. NMR Studies

NMR studies were done using a Bruker Ascend Aeon 700 or 500 equipped with a CPP BBO 500S1 BB-H&*F*-D-05 Z probe. For samples of characterization studies, each G-derivative (5 mM) was dissolved in DMSO-d_6 at 298 K unless otherwise stated. SGQ samples were studied dissolving 1 mM of each G-derivative in PBS, pH 7.4 with a 2% of H_2O-D_2O (9:1) and with varying concentrations of KSCN at 278 K unless otherwise stated. Sodium 3-(trimethylsilyl)propionate-2,2,3,3-d_4 (Aldrich) was used as the internal standard for the NMR experiments performed in H_2O-D_2O (9:1). NMR measurements of SGQ were performed using excitation sculpting water suppression experiments.

2.5.6. MS and IR characterization of G-derivatives

For the MS studies, an electrospray ionization mass spectrometry (ESI-MS) was recorded on a Waters Xevo-TQD using direct infusion. For the FT-IR analyses were performed on a Bruker Tensor 27 Infrared Spectrometer equipped with a Helios Attenuated Total Reflectance (ATR) accessory with a diamond crystal.

2.5.7. Turbidimetry

Turbidimetry experiments were performed at 650 nm using a UV-Vis spectrophotometer Varian instrument (Cary Bio-100) with a temperature controller. These studies were done at the minimum concentration of salt needed for the monomer to self-assemble into the SGQ, and in the temperature range of 0 °C to 75 °C at a heating rate of 0.3 min/°C.

2.5.8. Fixing of SHS particles

The solutions of SGQs were heated to 37 °C, and an aliquot of it was transferred to a vial with PBS, pH 7.4 at 37 °C for a final concentration of 50, 75, and 100 μM.

2.5.9. DLS size measurements of the SHS particles

A Malvern Zetasizer Nano Zs (ZEN3600) with a low-volume quartz batch cuvette (ZEN2112) was used to measure the hydrodynamic diameters of the SHS particles at varying temperatures.

2.5.10. DSC measurements of the stability of SHS particles

DSC measurements were performed on a VP-DSC microcalorimeter (MicroCal Inc.) with a cell volume of 0.517 mL, in a range of 2 °C to 90 °C with a heating rate of 1 °C min^{-1}. The experiments were performed at the minimum salt needed to self-assemble 1 mM of a given G-derivative in PBS, pH 7.4 with with a similar solution not containing the G-derivative used as a blank. Origin v7 was used for processing and deconvoluting the resulting curves.

2.5.11. Confocal microscopy experiments

Confocal microscopy images were done with a Nikon Eclipse Ti-E Inverted microscope of the Neuroimaging and Electrophysiology Facility (NIEF) at the UPR MSRC (NIH award number P20GM103642). The camera type used for all the samples of SHS particles was Andor Zyla VSC-9608 using an Plan Apo λ 60X with oil optics. A Nikon A1 plus camera with a Plan Apo λ 60X with oil optics was used for all the diluted SHS (*f*-SHS) particles.

2.6. Supplemental Information

2.6.1. Salting-In experiments

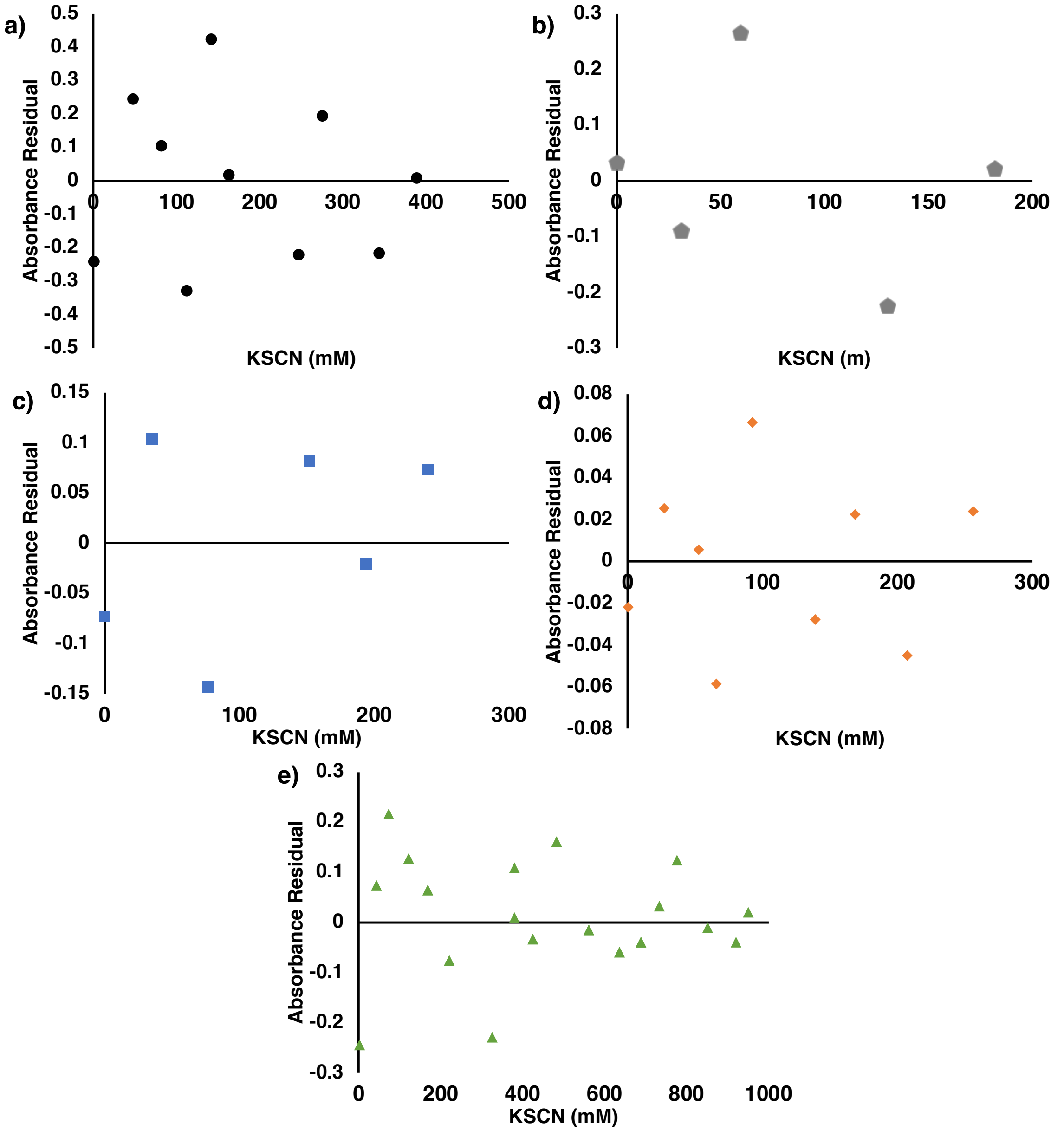

Figure S2.1. Residuals graphs of the 4-parameter logistic equation fitting done on the salting-in experiments. a) **aG’** b) **aG** c) **eG** d) **fG** d) **iG**.

2.6.2. SGQ Characterization

2.6.2.1. Water suppression NMR experiments at higher concentration of G-derivatives or KSCN

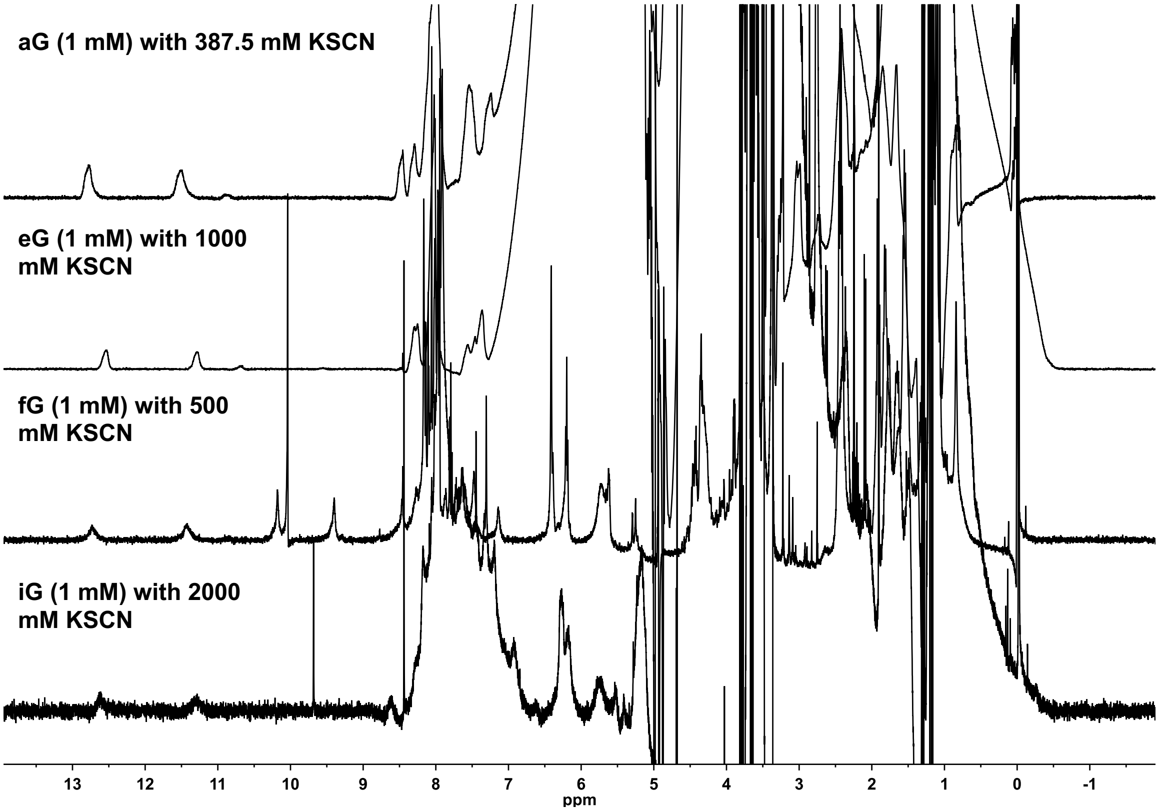

Figure S2.2. ^{1}H NMR of SGQs formed by various G-derivatives. The peaks in the region 11.20 - 12.80 ppm belong to the N1H and provide a signature for self-assembly. Conditions: $[KSCN]_{max}$ in PBS, pH 7.4 with 2% D_2O on 700 MHz at 278.15 K.

2.6.2.2. Turbidimetry Experiments

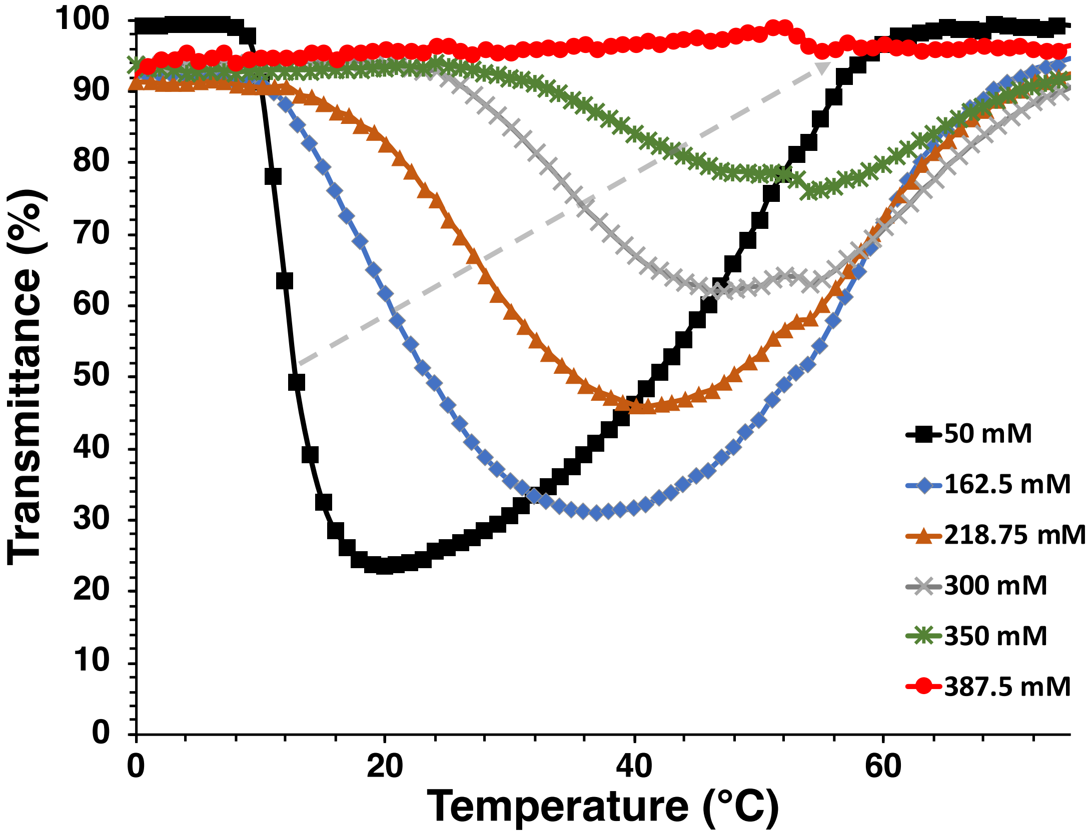

Figure S2.3. Turbidimetry experiments of variation of **aG** and KSCN concentrations in PBS, pH 7.4. Gray arrow showing the trend LCST.

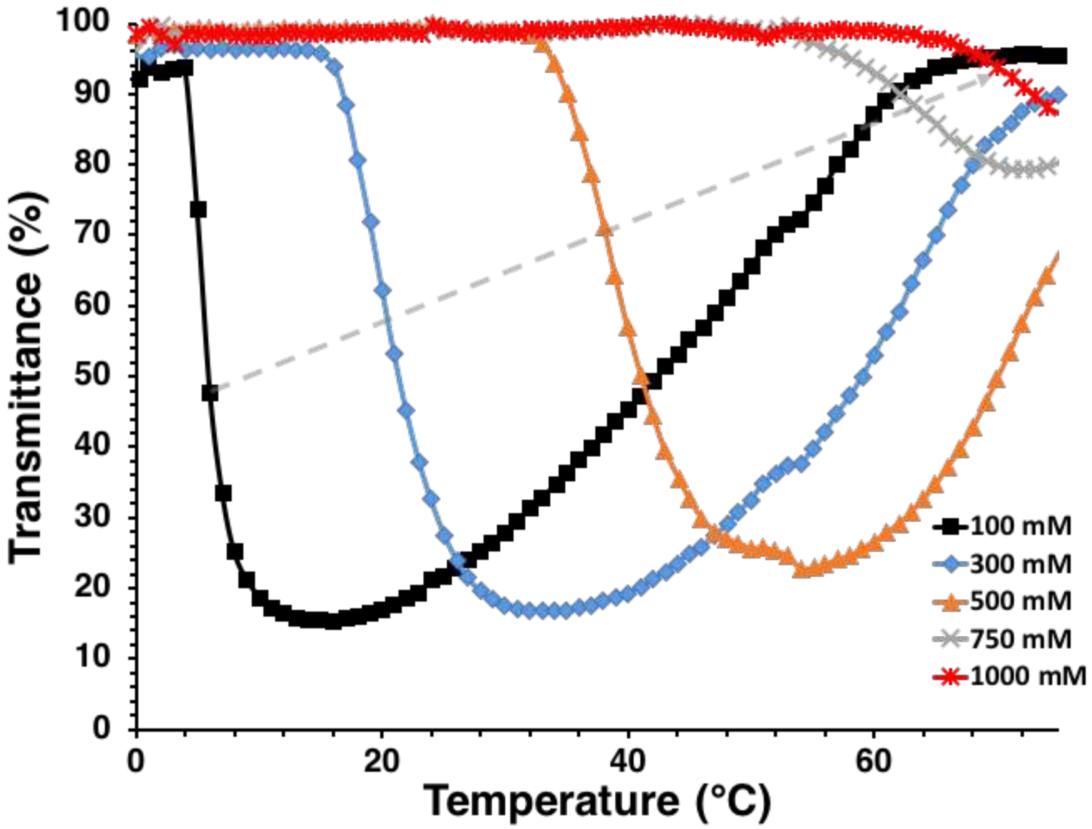

Figure S2.4. Turbidimetry experiments of variation of **eG** and KSCN concentrations in PBS, pH 7.4.

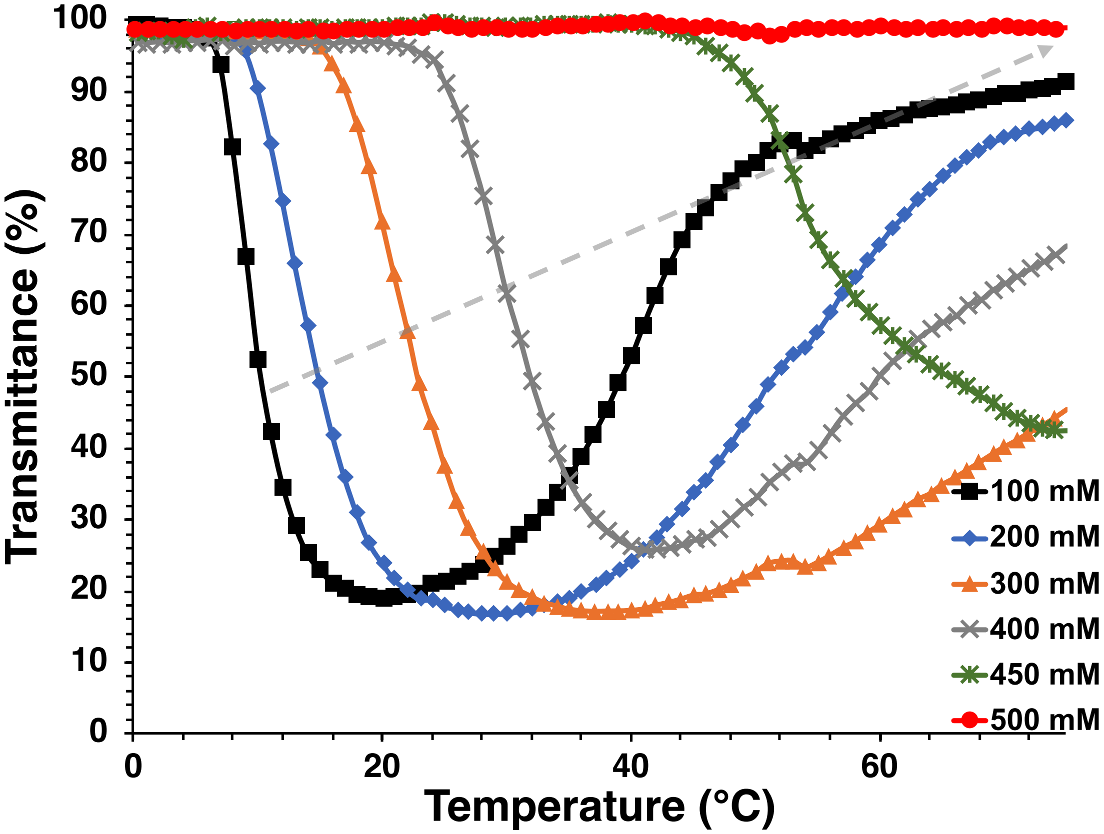

Figure S2.5. Turbidimetry experiments of variation of **fG** and KSCN concentrations in PBS, pH 7.4. Gray arrow showing LCST trend.

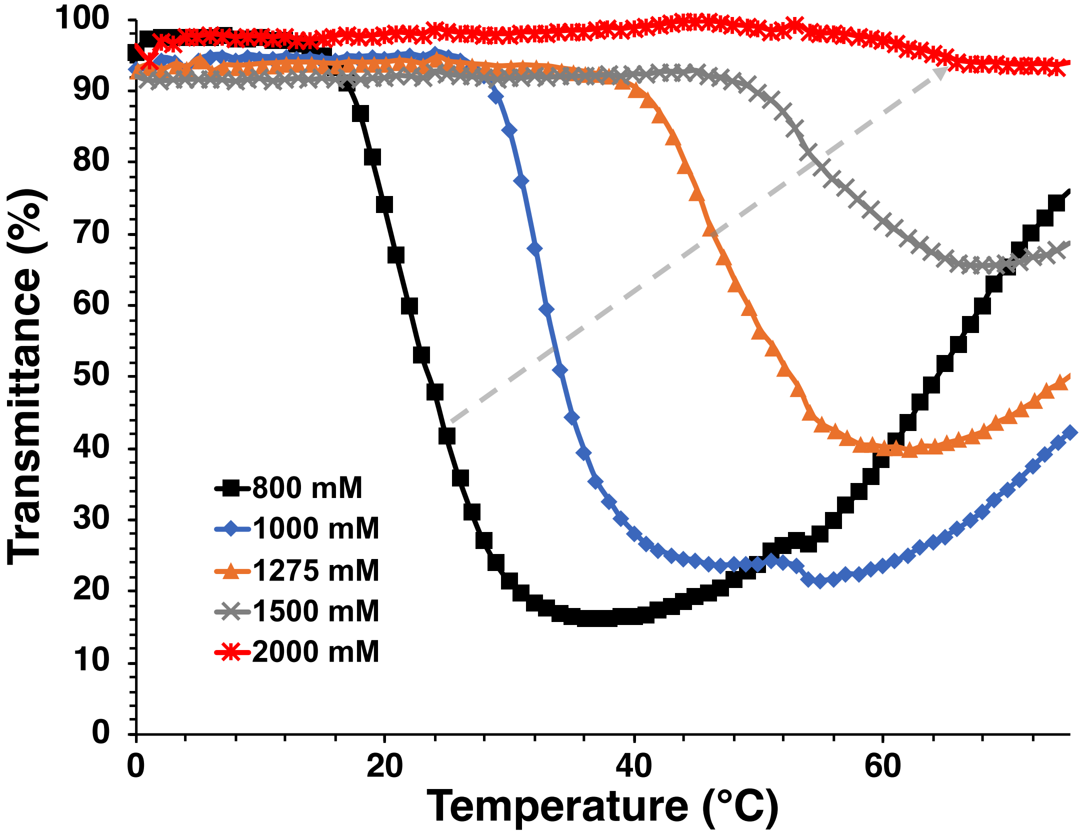

Figure S2.6. Turbidimetry experiments of variation of **iG** and KSCN concentrations in PBS, pH 7.4. Gray arrow showing LCST trend.

Table S2.1. Thermal properties of solutions with various concentrations of **aG’** in PBS (pH 7.4) at $[\text{KSCN}]_{\text{min}}$.

[aG’] (mM)	**LCST (°C)**	**UCST (°C)**
1	3	51
2.5	2.5	51
5	2.5	63

2.6.3. SHS particle characterization

2.6.3.1. Dynamic light scattering

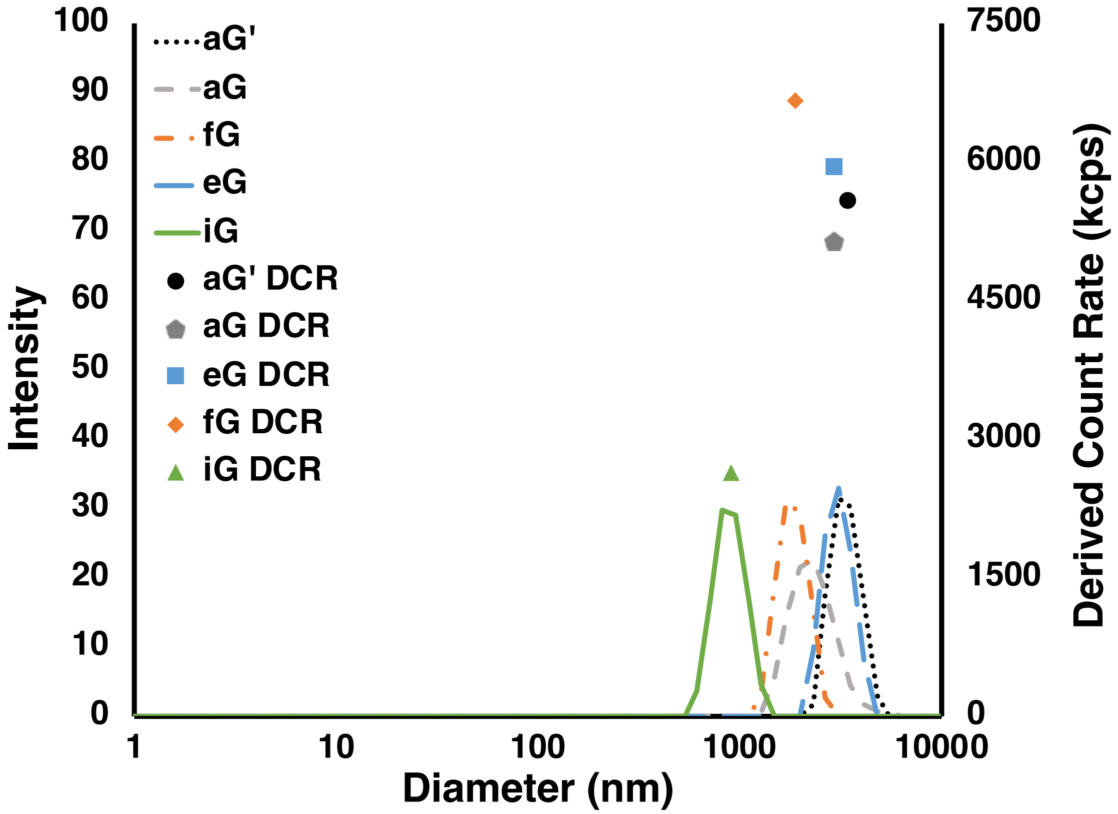

Figure S2.7. Hydrodynamic ratio and derived count rate and derived count rate of 1mM of G-derivatives with $[\mathrm{KSCN}]_{\mathrm{min}}$ in PBS, pH 7.4 at T_{cp} where the transmittance is lowest transmittance determined by the turbidimetry experiments. **aG'** was done in 13 °C, **aG** was done in 20 °C, **eG** was done in 16 °C, **fG** was done in 24 °C, and **iG** was done in 24 °C.

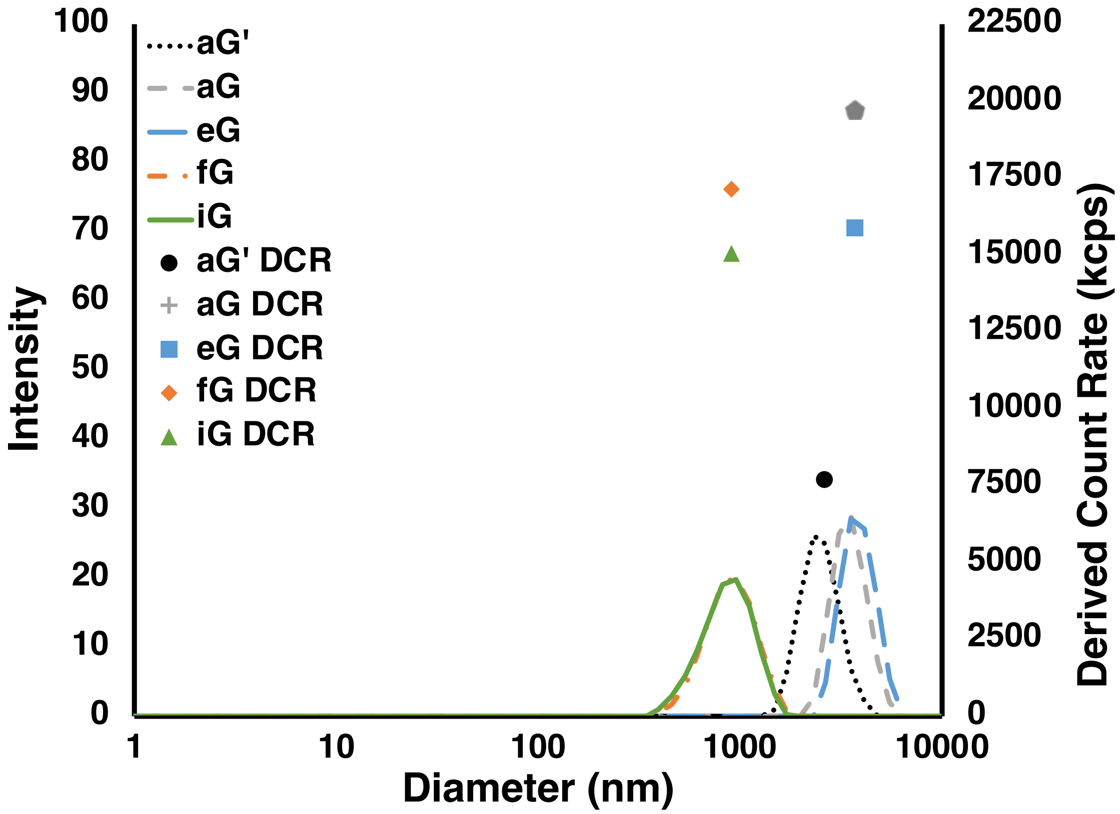

Figure S2.8. Hydrodynamic ratio and derived count rate of 1mM of G-derivatives with $[KSCN]_{min}$ in PBS, pH 7.4 at at 30 °C

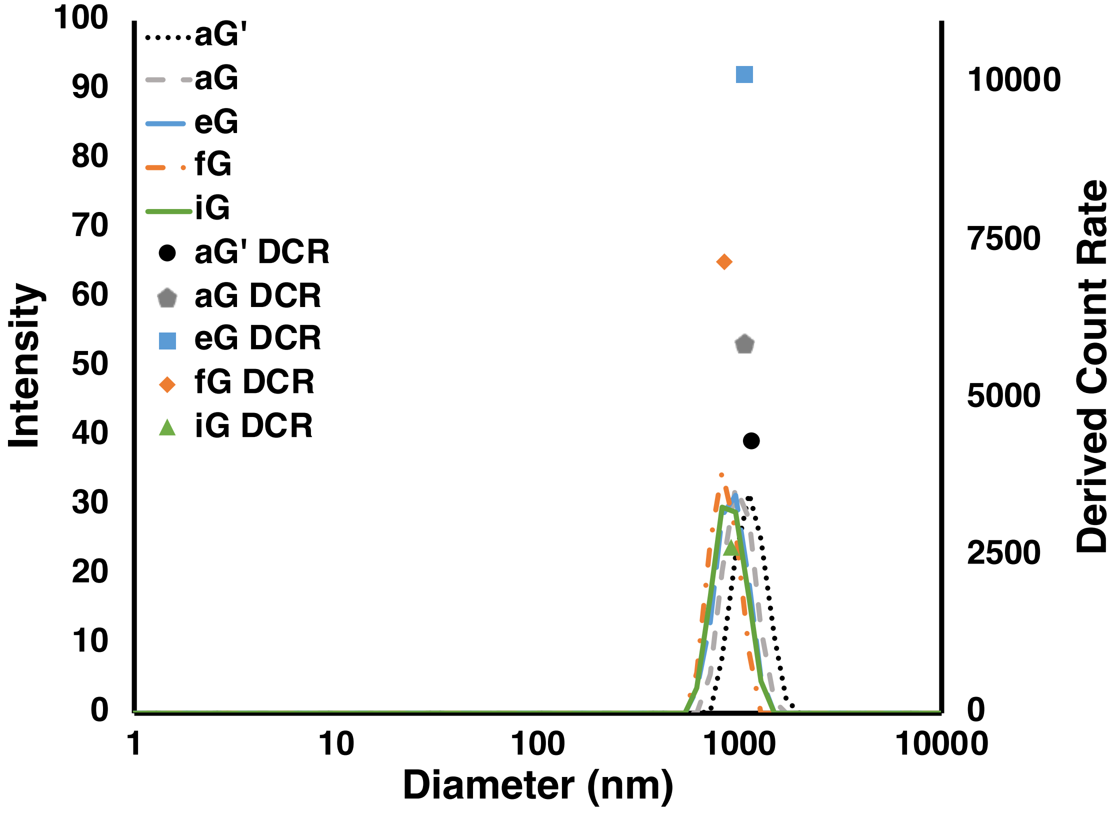

Figure S2.9. Hydrodynamic ratio and derived count rate of 1mM of G-derivatives with $[KSCN]_{min}$ in PBS, pH 7.4 at 37 °C

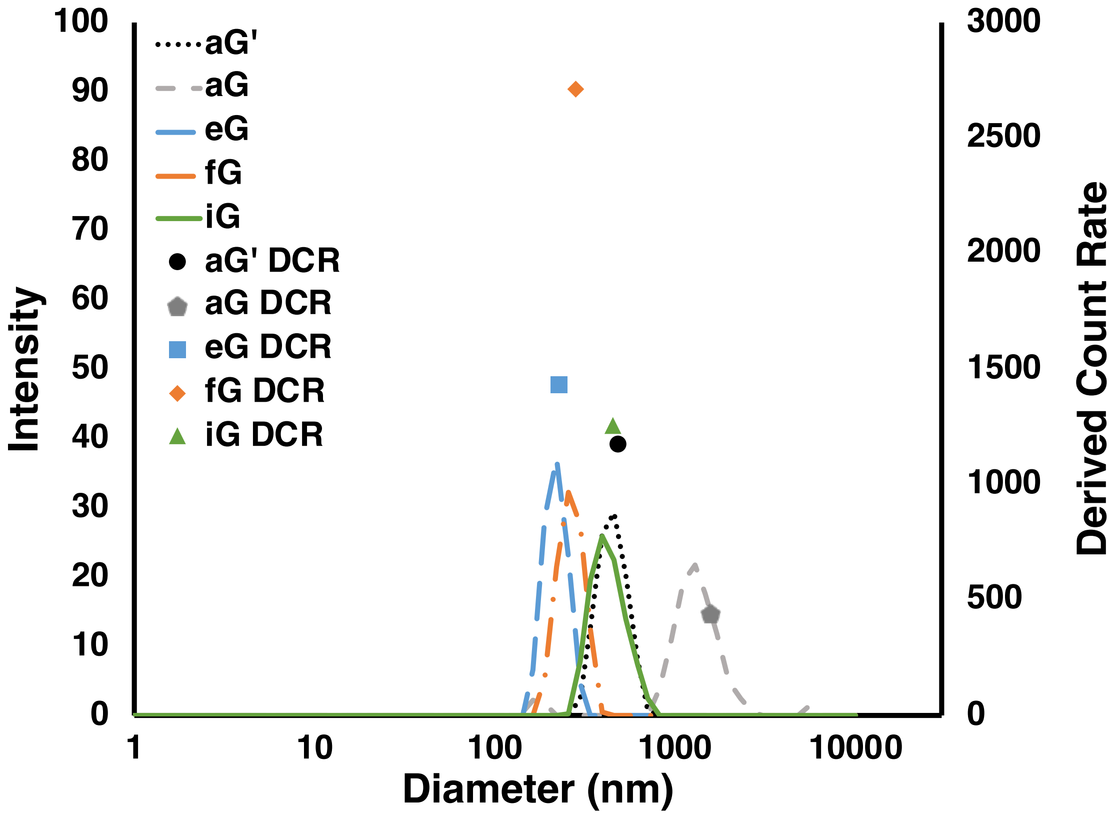

Figure S2.10. Hydrodynamic ratio and derived count rate of 1mM of G-derivatives with $[KSCN]_{min}$ in PBS, pH 7.4 at 75 °C.

2.6.3.2. Confocal Microscopy Experiments

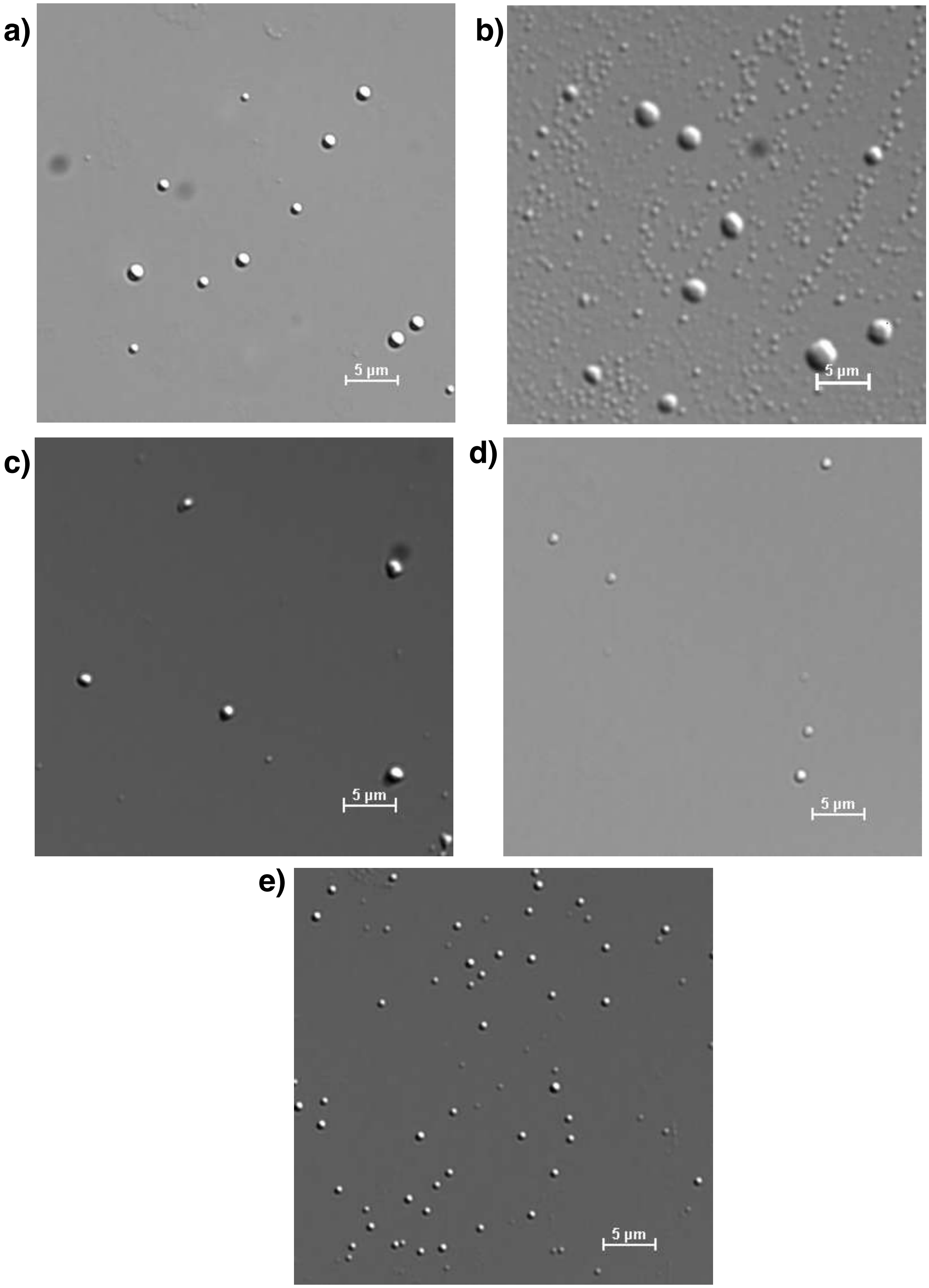

Figure S2.11. Confocal microscopy zoomed images of SHS particles at 1 mM with $[\text{KSCN}]_{\text{min}}$ in PBS, pH 7.4 at 30 °C. a) **aG’** b) **aG** c) **eG** d) **fG** e) **iG**.

Table S2.2. Summary of DLS data for SHS particle with 1 mM of G-derivatives and $[KSCN]_{min}$ in PBS, pH 7.4.

SHS	D_H at T_{cp} (nm)	DCR at T_{cp} (kcps)	D_H at 30 °C (nm)	DCR at 30 °C (kcps)	D_H at 37 °C (nm)	DCR at 37 °C (kcps)	D_H at 75 °C (nm)	DCR at 75 °C (kcps)
aG’	3432	5587	2623	7706	1155	4315	479	1179
aG	2966	5146	3736	19664	1061	5867	1593	448
eG	3158	5947	3974	15894	916	10139	225	1431
fG	1908	6662	917	17142	843	7162	283	2713
iG	916	2640	917	15019	916	2640	451	1255

T_{cp}: where the transmittance is lowest determined by the turbidimetry experiments. aG’ measured at 13 °C, aG measured at 20 °C, eG measured at 16 °C, fG measured at 20 °C; iG measured at 24 °C.

2.6.3.2. SHS particle fixing DLS

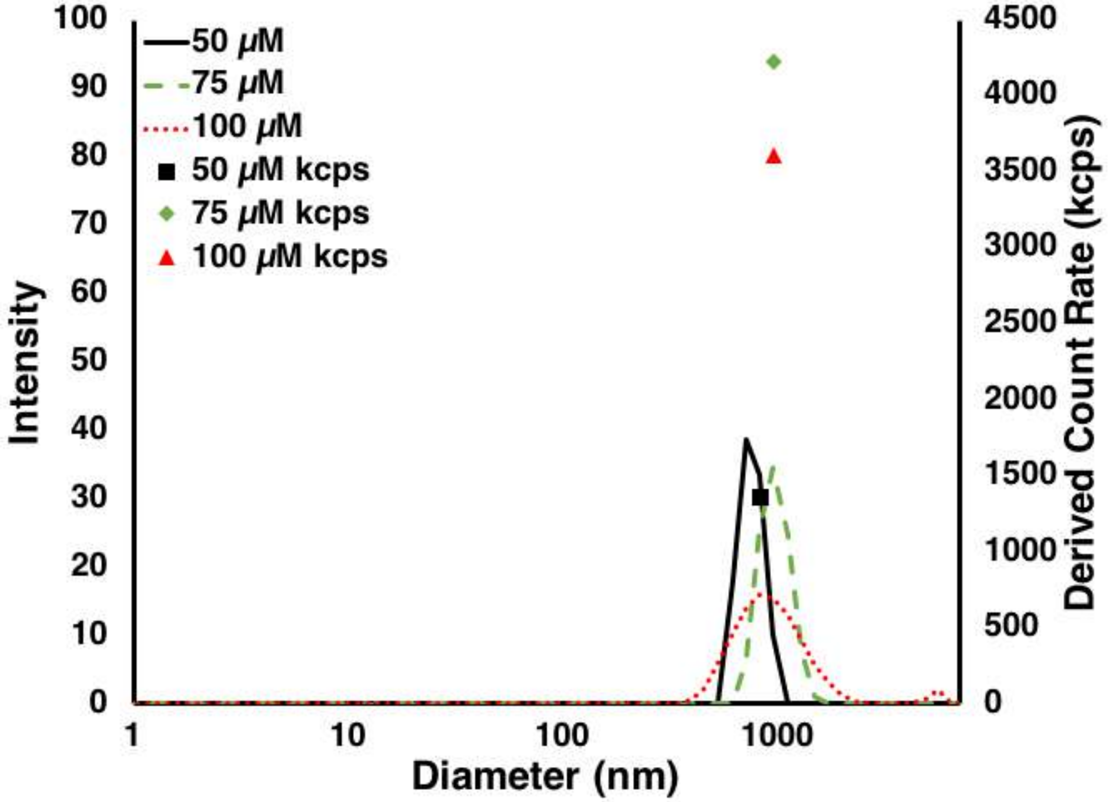

Figure S2.12. DLS experiments of ***f*-SHS-aG’** particles at 50, 75 and 100 μM of with 10, 15 and 20 mM of KSCN respectively of in PBS, pH 7.4 at 37 °C.

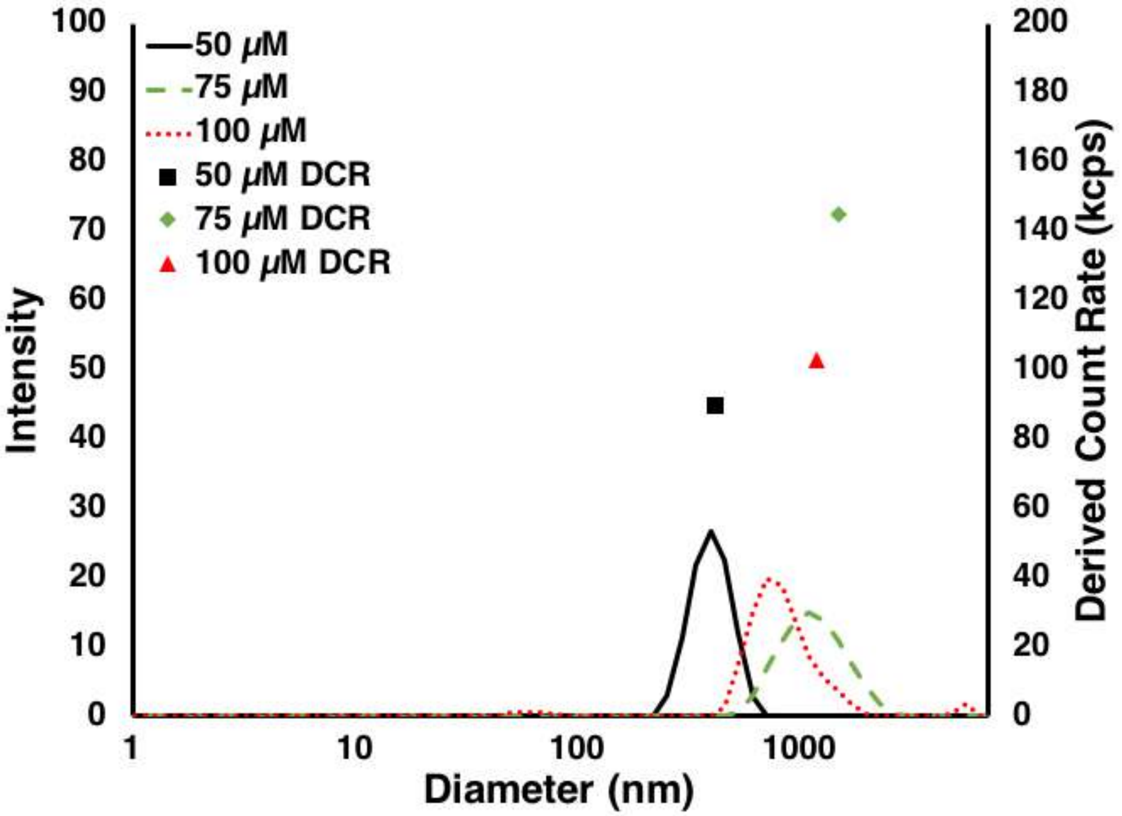

Figure S2.13. DLS experiments of ***f*-SHS-aG** particles at 50, 75 and 100 μM with 2.50, 3.75, 5.00 mM of KSCN respectively of in PBS, pH 7.4 at 37 °C.

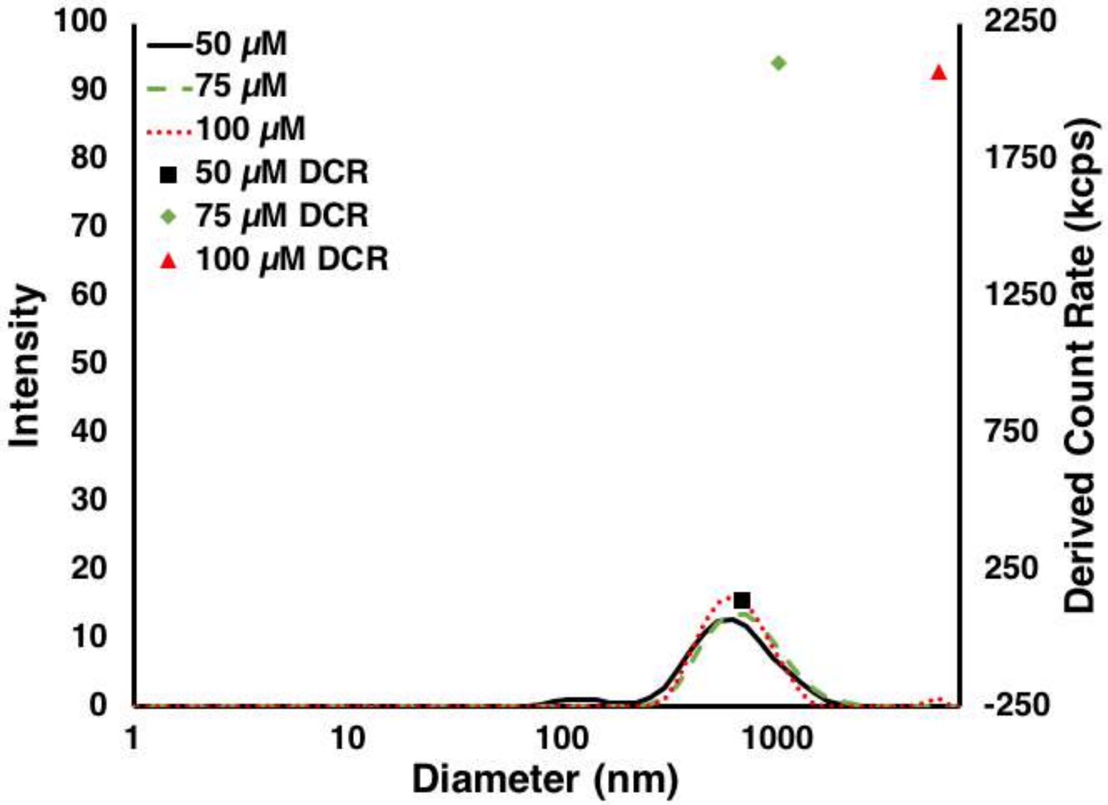

Figure S2.14. DLS experiments of ***f*-SHS-eG** particles at 50, 75 and 100 μM of with 5.0, 7.5 and 10.0 mM of KSCN respectively of in PBS, pH 7.4 at 37 °C.

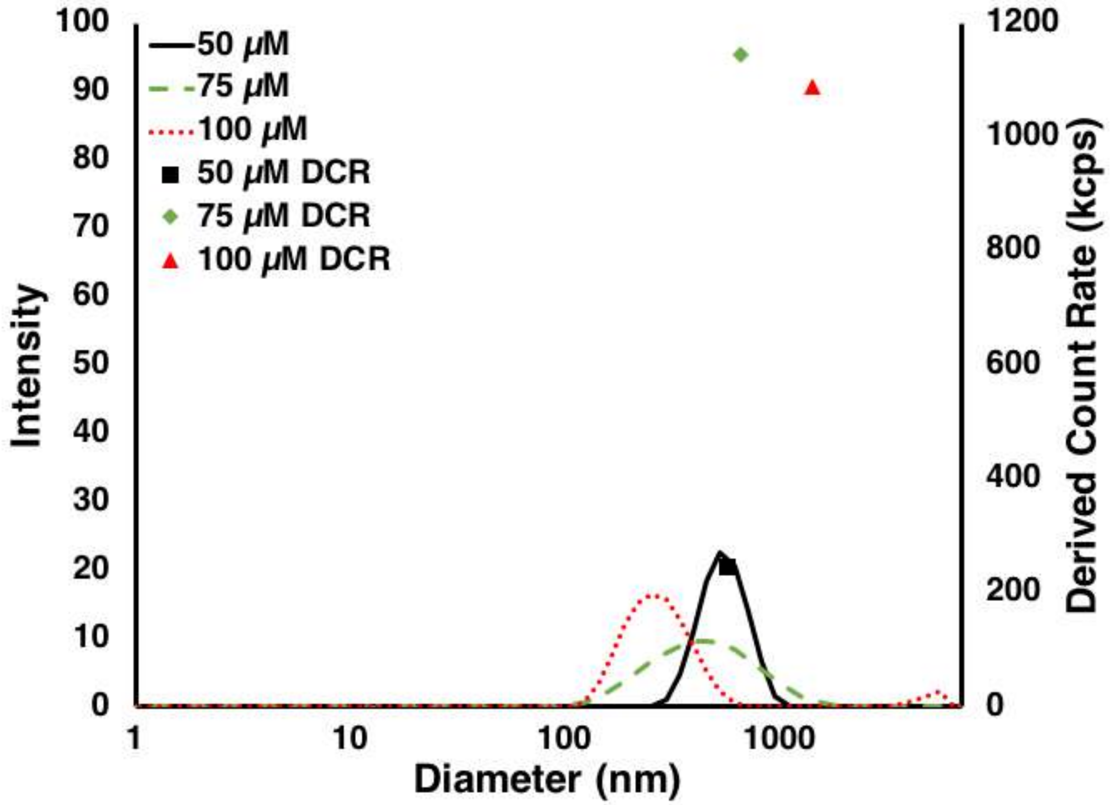

Figure S2.15. DLS experiments of ***f*-SHS-fG** particles at 50, 75 and 100 μM of with 5.0, 7.5 and 10.0 mM of KSCN respectively of in PBS, pH 7.4 at 37 °C.

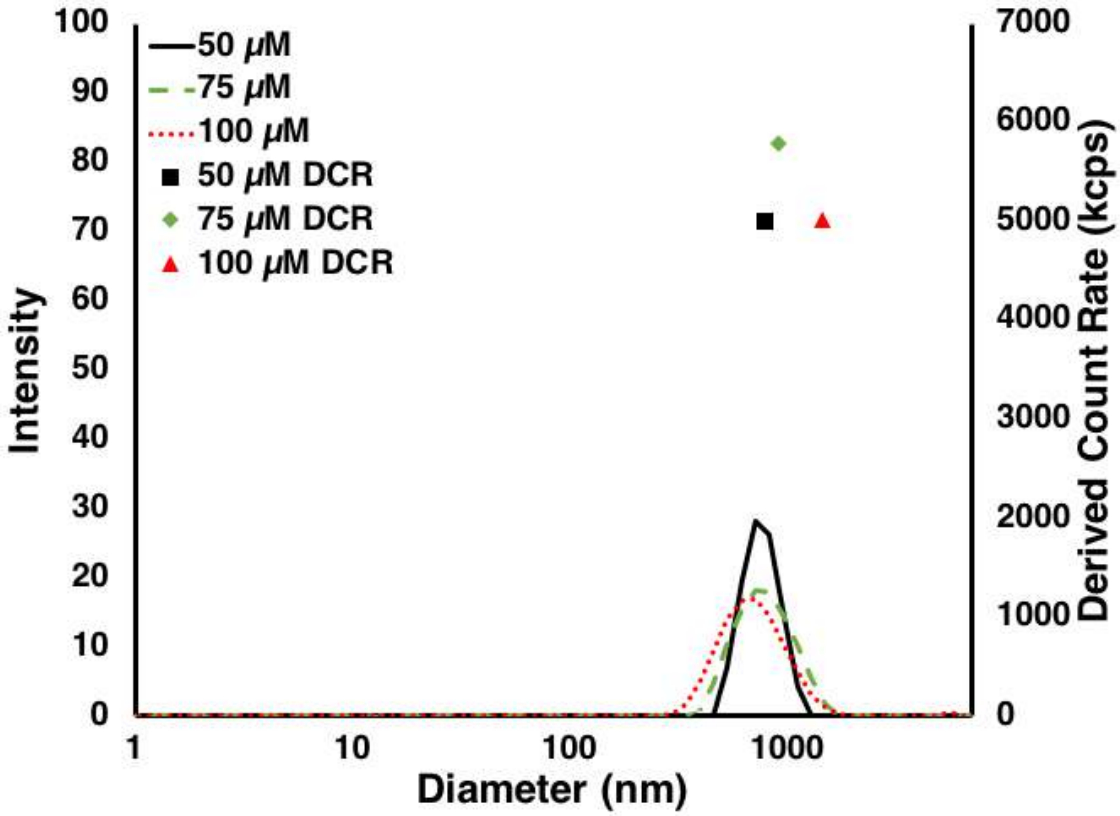

Figure S2.16. DLS experiments of ***f*-SHS-iG** particles at 50, 75 and 100 µM of with 40, 60 and 80 mM of KSCN respectively of in PBS, pH 7.4 at 37 °C.

Table S2.3. Summary of all DLS data for all *f*-SHS particles studied in this chapter .

	50 µM		**75 µM**		**100 µM**	
***f*-SHS**	**Diameter (nm)**	**DCR (kcps)**	**Diameter (nm)**	**DCR (kcps)**	**Diameter (nm)**	**DCR (kcps)**
aG’	1236	1364	1060	4227	1568	3614
aG	413	90	1483	145	1181	103
eG	679	138	1009	2104	1499	2075
fG	570	245	658	1145	1423	1087
iG	791	4999	917	5795	1442	5010

2.7. References

(1) Joshi, A. Microparticulates for Ophthalmic Drug Delivery. *J. Ocul. Pharmacol.* **1994**, *10* (1), 29–45. https://doi.org/10.1089/jop.1994.10.29.

(2) Crucho, C. I. C.; Barros, M. T. Polymeric Nanoparticles: A Study on the Preparation Variables and Characterization Methods. *Mater. Sci. Eng. C* **2017**, *80*, 771–784. https://doi.org/https://doi.org/10.1016/j.msec.2017.06.004.

(3) Anselmo, A. C.; Mitragotri, S. Nanoparticles in the Clinic. *Bioeng. Transl. Med.* **2016**, *1* (1), 10–29. https://doi.org/10.1002/btm2.10003.

(4) Caruso, F.; Caruso, R. A.; Möhwald, H. Nanoengineering of Inorganic and Hybrid Hollow Spheres by Colloidal Templating. *Science (80-.).* **1998**, *282* (5391), 1111 LP – 1114. https://doi.org/10.1126/science.282.5391.1111.

(5) McNamara, K.; Tofail, S. A. M. Nanoparticles in Biomedical Applications. *Adv. Phys. X* **2017**, *2* (1), 54–88. https://doi.org/10.1080/23746149.2016.1254570.

(6) Gao, W.; M. Chan, J.; C. Farokhzad, O. PH-Responsive Nanoparticles for Drug Delivery. *Mol. Pharm.* **2010**, *7* (6), 1913–1920. https://doi.org/10.1021/mp100253e.

(7) Chen, W.; Li, F.; Tang, Y.; Yang, S.; Li, J.; Yuan, Z.; Liu, Y.; Zhou, X.; Liu, C.; Zhang, X. Stepwise PH-Responsive Nanoparticles for Enhanced Cellular Uptake and on-Demand Intracellular Release of Doxorubicin. *Int. J. Nanomedicine* **2017**, *Volume 12*, 4241–4256. https://doi.org/10.2147/IJN.S129748.

(8) Cheng, R.; Meng, F.; Deng, C.; Klok, H.-A.; Zhong, Z. Dual and Multi-Stimuli Responsive Polymeric Nanoparticles for Programmed Site-Specific Drug Delivery. *Biomaterials* **2013**, *34* (14), 3647–3657. https://doi.org/https://doi.org/10.1016/j.biomaterials.2013.01.084.

(9) Van Vlierberghe, S.; Dubruel, P.; Schacht, E. Biopolymer-Based Hydrogels As Scaffolds for Tissue Engineering Applications: A Review. *Biomacromolecules* **2011**, *12* (5), 1387–1408. https://doi.org/10.1021/bm200083n.

(10) Kurzbach, D.; Hassouneh, W.; McDaniel, J. R.; Jaumann, E. A.; Chilkoti, A.; Hinderberger, D. Hydration Layer Coupling and Cooperativity in Phase Behavior of Stimulus Responsive Peptide Polymers. *J. Am. Chem. Soc.* **2013**, *135* (30), 11299–11308. https://doi.org/10.1021/ja4047872.

(11) Boutris, C.; Chatzi, E. G.; Kiparissides, C. Characterization of the LCST Behaviour of Aqueous Poly(N-Isopropylacrylamide) Solutions by Thermal and Cloud Point Techniques. *Polymer (Guildf).* **1997**, *38* (10), 2567–2570. https://doi.org/https://doi.org/10.1016/S0032-3861(97)01024-0.

(12) Huang, D.; Zhang, Q.; Deng, Y.; Luo, Z.; Li, B.; Shen, X.; Qi, Z.; Dong, S.; Ge, Y.; Chen, W. Polymeric Crown Ethers: LCST Behavior in Water and Stimuli-Responsiveness. *Polym. Chem.* **2018**. https://doi.org/10.1039/c8py00412a.

(13) Roux, R.; Ladavière, C.; Montembault, A.; Delair, T. Particle Assemblies: Toward New Tools for Regenerative Medicine. *Mater. Sci. Eng. C* **2013**, *33* (3), 997–1007. https://doi.org/https://doi.org/10.1016/j.msec.2012.12.002.

(14) Kanta Sharker, K.; Ohara, Y.; Shigeta, Y.; Ozoe, S.; Yusa, S. Upper Critical Solution Temperature (UCST) Behavior of Polystyrene-Based Polyampholytes in Aqueous Solution. *Polymers (Basel).* **2019**, *11* (2), 265. https://doi.org/10.3390/polym11020265.

(15) Seuring, J.; Agarwal, S. Polymers with Upper Critical Solution Temperature in Aqueous Solution. *Macromol. Rapid Commun.* **2012**, *33* (22), 1898–1920. https://doi.org/10.1002/marc.201200433.

(16) Pietsch, C.; Hoogenboom, R.; Schubert, U. S. PMMA Based Soluble Polymeric Temperature Sensors Based on UCST Transition and Solvatochromic Dyes. *Polym. Chem.* **2010**. https://doi.org/10.1039/c0py00162g.

(17) Ougizawa, T.; Inoue, T. UCST and LCST Behavior in Polymer Blends and Its Thermodynamic Interpretation. *Polym. J.* **1986**, *18* (7), 521–527. https://doi.org/10.1295/polymj.18.521.

(18) Martin, E. W.; Mittag, T. Relationship of Sequence and Phase Separation in Protein Low-Complexity Regions. *Biochemistry* **2018**, *57* (17), 2478–2487. https://doi.org/10.1021/acs.biochem.8b00008.

(19) Danhier, F.; Ansorena, E.; Silva, J. M.; Coco, R.; Le Breton, A.; Préat, V. PLGA-Based Nanoparticles: An Overview of Biomedical Applications. *J. Control. Release* **2012**, *161* (2), 505–522. https://doi.org/https://doi.org/10.1016/j.jconrel.2012.01.043.

(20) Scherzinger, C.; Schwarz, A.; Bardow, A.; Leonhard, K.; Richtering, W. Cononsolvency of Poly-N-Isopropyl Acrylamide (PNIPAM): Microgels versus Linear Chains and Macrogels. *Curr. Opin. Colloid Interface Sci.* **2014**, *19* (2), 84–94. https://doi.org/https://doi.org/10.1016/j.cocis.2014.03.011.

(21) Wolfram, J.; Zhu, M.; Yang, Y.; Shen, J.; Gentile, E.; Paolino, D.; Fresta, M.; Nie, G.; Chen, C.; Shen, H.; Zhao, M. F. and Y. Safety of Nanoparticles in Medicine. *Current Drug Targets*. 2015, pp 1671–1681. https://doi.org/http://dx.doi.org/10.2174/1389450115666140804124808.

(22) Hua, S.; de Matos, M. B. C.; Metselaar, J. M.; Storm, G. Current Trends and Challenges in the Clinical Translation of Nanoparticulate Nanomedicines: Pathways for Translational Development and Commercialization. *Front. Pharmacol.* **2018**, *9*. https://doi.org/10.3389/fphar.2018.00790.

(23) Lehn, J.-M. From Supramolecular Chemistry towards Constitutional Dynamic Chemistry and Adaptive Chemistry. *Chem. Soc. Rev.* **2007**, *36* (2), 151–160. https://doi.org/10.1039/B616752G.

(24) Akiyoshi, K.; Deguchi, S.; Moriguchi, N.; Yamaguchi, S.; Sunamoto, J. Self-Aggregates of Hydrophobized Polysaccharides in Water. Formation and Characteristics of Nanoparticles. *Macromolecules* **1993**, *26* (12), 3062–3068. https://doi.org/10.1021/ma00064a011.

(25) Todd, E. M.; Quinn, J. R.; Park, T.; Zimmerman, S. C. Fidelity in the Supramolecular Assembly of Triply and Quadruply Hydrogen-Bonded Complexes. *Isr. J. Chem.* **2005**, *45* (3), 381–389. https://doi.org/10.1560/DQCJ-1K9J-1TBT-DK5M.

(26) Negrón, L. M.; Meléndez-Contés, Y.; Rivera, J. M. Patchy Supramolecules as Versatile Tools To Probe Hydrophobicity in Nanoglobular Systems. *J. Am. Chem. Soc.* **2013**, *135* (10), 3815–3817. https://doi.org/10.1021/ja401373h.

(27) Betancourt, J. E.; Rivera, J. M. Tuning Thermoresponsive Supramolecular G-Quadruplexes. *Langmuir* **2015**, *31* (7), 2095–2103. https://doi.org/10.1021/la504446k.

(28) Rastegar, A. Chapter 195 Serum Potassium. In *Clinical Methods: The History, Physical, and Laboratory Examinations*; 1990.

(29) Zangi, R. Can Salting-In/Salting-Out Ions Be Classified as Chaotropes/Kosmotropes? *J. Phys. Chem. B* **2009**, *114* (1), 643–650. https://doi.org/10.1021/jp909034c.

(30) Okur, H. I.; Hladílková, J.; Rembert, K. B.; Cho, Y.; Heyda, J.; Dzubiella, J.; Cremer, P. S.; Jungwirth, P. Beyond the Hofmeister Series: Ion-Specific Effects on Proteins and Their Biological Functions. *J. Phys. Chem. B* **2017**, *121* (9), 1997–2014. https://doi.org/10.1021/acs.jpcb.6b10797.

(31) Negrón, L. M. Synthesis and Characterization of Thermo/PH-Responsive Supramolecular G-Quadruplexes for the Construction of Supramolecular Hacky Sacks for Biorelevant Applications, University of Puerto Rico, Rio Piedras Campus, 2014.

(32) Rivera, J. M.; Negrón, L. M. Supramolecular Hacky Sacks (SHS), Method of Synthesis and Applications Thereof. 10106572, 2018.

(33) Gubala, V. Self-Assembly and Molecular Recognition of 8-Aryl-2'-Deoxyguanosine Analogues, University of Puerto Rico, Rio Piedras, 2006. https://doi.org/CN 547.7 G921S.

(34) Wu, P.; Malkoch, M.; Hunt, J. N.; Vestberg, R.; Kaltgrad, E.; Finn, M. G.; Fokin, V. V; Sharpless, K. B.; Hawker, C. J. Multivalent, Bifunctional Dendrimers Prepared by Click Chemistry. *Chem. Commun.* **2005**, No. 46, 5775–5777. https://doi.org/10.1039/B512021G.

(35) Betancourt, J. E.; Rivera, J. M. Hexadecameric Self-Assembled Dendrimers Built from 2′-Deoxyguanosine Derivatives. *Org. Lett.* **2008**, *10* (11), 2287–2290. https://doi.org/10.1021/ol800701j.

(36) Rostovtsev, V. V; Green, L. G.; Fokin, V. V; Sharpless, K. B. A Stepwise Huisgen Cycloaddition Process: Copper(I)-Catalyzed Regioselective “Ligation” of Azides and Terminal Alkynes. *Angew. Chemie Int. Ed.* **2002**, *41* (14), 2596–2599. https://doi.org/10.1002/1521-3773(20020715)41:14<2596::AID-ANIE2596>3.0.CO;2-4.

(37) Heyda, J.; I. Okur, H.; Hladílková, J.; B. Rembert, K.; Hunn, W.; Yang, T.; Dzubiella, J.; Jungwirth, P.; S. Cremer, P. Guanidinium Can Both Cause and Prevent the Hydrophobic Collapse of Biomacromolecules. *J. Am. Chem. Soc.* **2017**, *139* (2), 863–870. https://doi.org/10.1021/jacs.6b11082.

(38) Gubala, V.; Betancourt, J. E.; Rivera, J. M. Expanding the Hoogsteen Edge of 2‘-Deoxyguanosine: Consequences for G-Quadruplex Formation. *Org. Lett.* **2004**, *6* (25), 4735–4738. https://doi.org/10.1021/ol048013v.

(39) Rivera, L. R.; Betancourt, J. E.; Rivera, J. M. Aquatic Self-Assembly of Sixteen Subunits into a 39-KDa Dendrimer. *Langmuir* **2011**, *27* (4), 1409–1414. https://doi.org/10.1021/la103961m.

(40) Rivera-Sánchez, M. del C.; García-Arriaga, M.; Hobley, G.; Morales-de-Echegaray, A. V; Rivera, J. M. Small-Molecule-Based Self-Assembled Ligands for G-Quadruplex DNA Surface Recognition. *ACS Omega* **2017**, *2* (10), 6619–6627. https://doi.org/10.1021/acsomega.7b01255.

(41) García-Arriaga, M.; Hobley, G.; Rivera, J. M. Structural Studies of Supramolecular G-Quadruplexes Formed from 8-Aryl-2′-Deoxyguanosine Derivatives. *J. Org. Chem.* **2016**, *81* (14), 6026–6035. https://doi.org/10.1021/acs.joc.6b01113.

(42) García-Arriaga, M.; Acosta-Santiago, M.; Cruz, A.; Rivera-Rivera, J. M.; López, G. E.; Rivera, J. M. Probing the Limits of Supramolecular G-Quadruplexes Using Atomistic Molecular Dynamics Simulations. *Inorganica Chim. Acta* **2017**, *468* (Supplement C), 209–222. https://doi.org/https://doi.org/10.1016/j.ica.2017.08.051.

(43) Schild, H. G. Poly(N-Isopropylacrylamide): Experiment, Theory and Application. *Prog. Polym. Sci.* **1992**, *17* (2), 163–249. https://doi.org/10.1016/0079-6700(92)90023-R.

(44) Dalgakiran, E.; Tatlipinar, H. The Role of Hydrophobic Hydration in the LCST Behaviour of POEGMA300 by All-Atom Molecular Dynamics Simulations. *Phys. Chem. Chem. Phys.* **2018**, *20* (22), 15389–15399. https://doi.org/10.1039/C8CP02026D.

(45) Rahimian-Bajgiran, K.; Chan, N.; Zhang, Q.; Noh, S. M.; Lee, H.; Oh, J. K. Tuning LCST with Thiol-Responsiveness of Thermoresponsive Copolymers Containing Pendant Disulfides. *Chem. Commun.* **2013**, *49* (8), 807–809. https://doi.org/10.1039/C2CC37804C.

(46) Lutz, J.-F.; Akdemir, Ö.; Hoth, A. Point by Point Comparison of Two Thermosensitive Polymers Exhibiting a Similar LCST: Is the Age of Poly(NIPAM) Over? *J. Am. Chem. Soc.* **2006**, *128* (40), 13046–13047. https://doi.org/10.1021/ja065324n.

(47) Tavagnacco, L.; Zaccarelli, E.; Chiessi, E. On the Molecular Origin of the Cooperative Coil-to-Globule Transition of Poly(N-Isopropylacrylamide) in Water. *Phys. Chem. Chem. Phys.* **2018**, *20* (15), 9997–10010. https://doi.org/10.1039/C8CP00537K.

(48) Oncsik, T.; Desert, A.; Trefalt, G.; Borkovec, M.; Szilagyi, I. Charging and Aggregation of Latex Particles in Aqueous Solutions of Ionic Liquids: Towards an Extended Hofmeister Series. *Phys. Chem. Chem. Phys.* **2016**, *18* (10), 7511–7520. https://doi.org/10.1039/C5CP07238G.

(49) Belfleur, L. New Alternatives for the Development and Characterization of Stimuli-Responsive Supramolecules by Using Guanosine Derivatives and Raman Spectroscopy, University of Puerto Rico, Rio Piedras Campus, 2019.

(50) Betancourt, J. E.; Rivera, J. M. Nonpolymeric Thermosensitive Supramolecules. *J. Am. Chem. Soc.* **2009**, *131* (46), 16666–16668. https://doi.org/10.1021/ja9070927.

(51) Hyman, A. A.; Weber, C. A.; Jülicher, F. Liquid-Liquid Phase Separation in Biology. *Annu. Rev. Cell Dev. Biol.* **2014**. https://doi.org/10.1146/annurev-cellbio-100913-013325.

(52) Betancourt, J. E.; Martín-Hidalgo, M.; Gubala, V.; Rivera, J. M. Solvent-Induced High Fidelity Switching Between Two Discrete Supramolecules. *J. Am. Chem. Soc.* **2009**, *131* (9), 3186–3188. https://doi.org/10.1021/ja809612d.

(53) Negrón, L. M.; Díaz, T. L.; Ortiz-Quiles, E. O.; Dieppa-Matos, D.; Madera-Soto, B.; Rivera, J. M. Organic Nanoflowers from a Wide Variety of Molecules Templated by a Hierarchical Supramolecular Scaffold. *Langmuir* **2016**, 2283–2290. https://doi.org/10.1021/acs.langmuir.5b03946.

(54) Bizmark, N.; Ioannidis, M. A. Effects of Ionic Strength on the Colloidal Stability and Interfacial Assembly of Hydrophobic Ethyl Cellulose Nanoparticles. *Langmuir* **2015**, *31* (34), 9282–9289. https://doi.org/10.1021/acs.langmuir.5b01857.

(55) Milz, L.; Schmiedeberg, M. Connecting the Random Organization Transition and Jamming within a Unifying Model System. *Phys. Rev. E* **2013**, *88* (6), 62308. https://doi.org/10.1103/PhysRevE.88.062308.

(56) Tjhung, E.; Berthier, L. Hyperuniform Density Fluctuations and Diverging Dynamic Correlations in Periodically Driven Colloidal Suspensions. *Phys. Rev. Lett.* **2015**, *114* (14), 148301. https://doi.org/10.1103/PhysRevLett.114.148301.

(57) Mo, S.; Shao, X.; Chen, Y.; Cheng, Z. Increasing Entropy for Colloidal Stabilization. *Sci. Rep.* **2016**, *6* (1), 36836. https://doi.org/10.1038/srep36836.

(58) Kim, H.; Jeon, B. jin; Kim, S.; Jho, Y. S.; Hwang, D. S. Upper Critical Solution Temperature (UCST) Behavior of Coacervate of Cationic Protamine and Multivalent Anions. *Polymers (Basel).* **2019**. https://doi.org/10.3390/polym11040691.

(59) Kreuzer, L. P.; Widmann, T.; Bießmann, L.; Hohn, N.; Pantle, J.; Märkl, R.; Moulin, J.-F.; Hildebrand, V.; Laschewsky, A.; Papadakis, C. M.; Müller-Buschbaum, P. Phase Transition Kinetics of Doubly Thermoresponsive Poly(Sulfobetaine)-Based Diblock Copolymer Thin Films. *Macromolecules* **2020**, *53* (8), 2841–2855. https://doi.org/10.1021/acs.macromol.0c00046.

Chapter 3. Supramolecular Structure & Dynamics of Biothiol Guanine Conjugates

3.1. Abstract

Biothiols have been useful for the study of responsive nanomaterials. A way to implement these is by having a thiol-Michael reaction receptor incorporated in the nanomaterial. Current thiol-Michael reaction receptors are polymers and nanomaterials, whose lack of quality control can hinder their development and translation into the clinic. Previously we have reported the synthesis of colloidal particles termed Supramolecular Hacky Sacks (SHS). Here we are introducing their responsive behavior towards biothiols such as cysteine and glutathione. We achieved biothiol responsiveness by studying the forward and reverse reactions of the monomeric G-derivative as a thiol-Michael acceptor. Experiments showed that cysteine had a rapid forward reaction $t_{1/2}$ = 6 min as glutathione $t_{1/2}$ = 36 min. We also saw this behavior for the reversible reaction. The presence of biothiols affected the corresponding SHS particle in the same way, showing a slow release of encapsulated Rhodamine B. SHS particles that react with cysteine show the fastest Rhodamine B release compared to those reacting with glutathione. These results show the successful synthesis of a biothiol responsive discrete supramolecule SHS particles. Later work should include the exploration of other molecules.

3.2. Introduction

As particles continue to be developed for biomedical applications, responsive properties come to the forefront. Researchers design reaction-based probes for detecting glutathione (GSH) by using thiol-Michael addition to produce useful bioconjugates in responsive nanoparticles.[1–3] This is because GSH in the cellular environment has been connected to several types of cancers or HIV.[4] This reaction has been used extensively in material and polymer chemistry to synthesize small molecules, surface modifications, polymer conjugation, cross-linked polymer networks, hydrogels, and the synthesis of nanomaterials specifically for improving their solubility properties.[3,5] In polymer chemistry and materials science, the thiol-Michael addition is an essential tool. This tool's primary use is to derivatize polymers containing acrylates, acrylamides, or maleimides to obtain the desired physical and chemical properties.[3,6,7] In the case of proteins, the maleimide-thiol "click" chemistry is employed to form useful bioconjugates.[3,6,8,9] Therefore, this reaction is a flexible tool that expands the materials used in drug delivery and sensing.

The reversibility of the thiol-Michael reaction can be achieved by reacting to the thiol moiety with an α,β-unsaturated carbonyl. The thiol-Michael addition is a conjugate addition in which a nucleophilic attack by a thiol or a thiolate on the β-carbon, resulting in a negatively-charged enolate intermediate that yields the Michael adduct.[3,6,9] The kinetics of the reaction depends on the thiol pK_a, the electron-deficiency of the β carbon, the presence of catalysts (its concentration and pK_a), and polarity of the solvent and its pH.[3,10]

Using the Michael addition serves as a tool for modulating the hydrophobic-hydrophilic balance and water solubility. Considering this, we can include the α,β-unsaturated carbonyl moiety into our drug delivery systems termed

Supramolecular Hacky Sacks.[11] These meso-globular particles are the thermal response result of supramolecular guanosine quadruplexes (SGQs) when exposed to temperatures over their lowest critical solution temperature (LCST).[11–15] SGQs are typically made up of eight, twelve, or sixteen 8-aryl-2′-deoxyguanosine (8ArG) monomers, forming octameric, dodecameric, or hexadecameric SGQs. The SGQ itself is the self-assembly of 8ArG via H-bond self-recognition to build each tetrad in a salting-in manner. These tetrads are then stacked and held together by cations such as potassium ions between tetrads.[16] This organization-level helps us develop easily modified discrete supramolecular structures by just changing a small molecule. This way, by including an α,β-unsaturated carbonyl in the 8ArG can be translated into a thiol-responsive SHS particle.

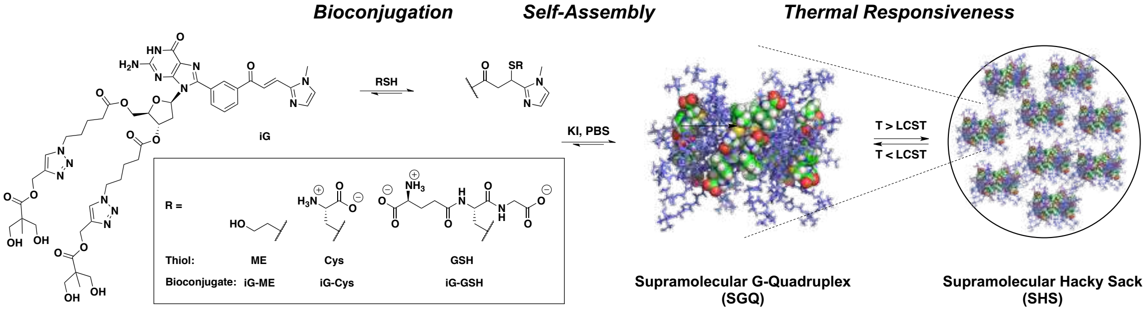

Figure 3.1. Overview of the bioconjugation strategy of biothiols to **iG**, and subsequent self-assembly of these thiol conjugates into discrete SGQ structures. These SGQs are thermoresponsive and can form colloidal SHS particles that have been used to encapsulate and deliver small molecules, polymers, proteins, and plasmid DNA.

Here we show our studies of a α,β-unsaturated carbonyl-containing SHS particle reaction with biothiols. We start by studying the kinetics of this reaction to help us understand its reversibility using G-derivative **iG** with mercaptoethanol (**ME**), L-cysteine (**Cys**), and **GSH** (Figure 3.1). From here, we synthesize compounds **iG-ME**, **-Cys**, and **-GSH** to study their self-assembly into SGQs and thermoresponsive properties resulting in SHS particles. We studied the corresponding SHS particles via dynamic light scattering (DLS). After full characterization of the SHS particles, we decided to investigate how the SHS particles, based on 8ArG 1, released encapsulated rhodamine B (**RhoB**) in the presence of **Cys** and **GSH**.

3.3. Results and discussion

3.3.1. 8ArG Thiol-Michael

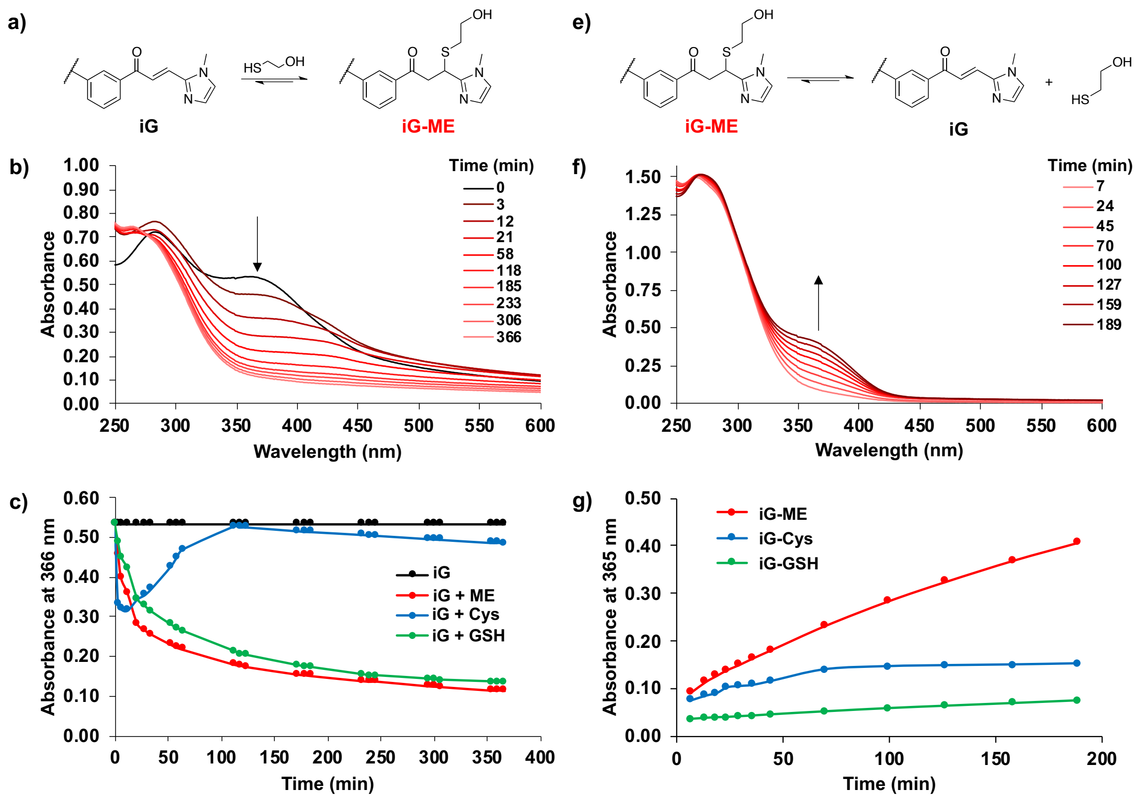

d)

	iG + ME	iG + Cys	iG + GSH
k (M^{-1} s^{-1})	0.537	1.868	0.323
$t_{1/2}$ (min)	22	6.0	36

h)

	iG-ME	iG-Cys	iG-GSH
k_{-1} (s^{-1})	2.83×10^{-4}	1.80×10^{-4}	1.02×10^{-4}
$t_{1/2}$ (min)	41	61	114

Figure 3.2. Thiol-Michael addition kinetics and reversibility studies are done via UV-Vis absorbance. a) Reaction being monitored: **iG** + **ME**. b) UV-Vis spectra as a function of time for the previous reaction (50 μM **iG** + 1 mM ME in 1% MeOH in PBS, pH 7.4). c) Pseudo-first order kinetics of **iG** (50 μM) + thiols (1 mM) by monitoring the absorbance at 365 nm as a function of time. d) Rate constants and hal*f*-lives of reaction for **iG** + thiols. e) Reaction being monitored: retro thiol-Michael reaction of 2. f) UV-Vis spectra as a function of time for the previous reaction (starting concentration of 2: 50 μM, in 1% MeOH in PBS, pH 7.4). g) First-order kinetics of thiol conjugates by monitoring absorbance at 365 nm as a function of time. h) Rate constants for the retro-thiol-Michael reaction and hal*f*-lives of reaction for different thiol conjugates.

First, we tested if **iG** would react with biothiols and if it did, at what rate. To address these, we performed UV-Vis spectroscopy kinetic studies (Figure 2.2). As an example, we show in Figure 3.2 the reaction of **iG** with **ME** to produce **iG**-**ME** (**2**). The UV-Vis spectra for this reaction as a function of time can be seen in Figure 3.2b. At time zero, we see an absorption band at 360 nm, which corresponds to the fully conjugated α,β-unsaturated system. Upon the addition of **ME** showing that the thiol-Michael is taking place, conjugation is lost by the decreases in absorbance at 360 nm. Meanwhile, a new peak arises around 260 nm rises. We take the reduction of absorbance of this band as evidence for consumption of **iG** and monitor it to get pseudo-first-order kinetics. A 20-fold excess of biothiol was used to establish the pseudo-first-order kinetics. We did the same with Cys and GSH, and as shown in Figure 3.2c, we see the kinetic traces of absorbance as a function of time for **iG** (control) and **iG** + thiol.

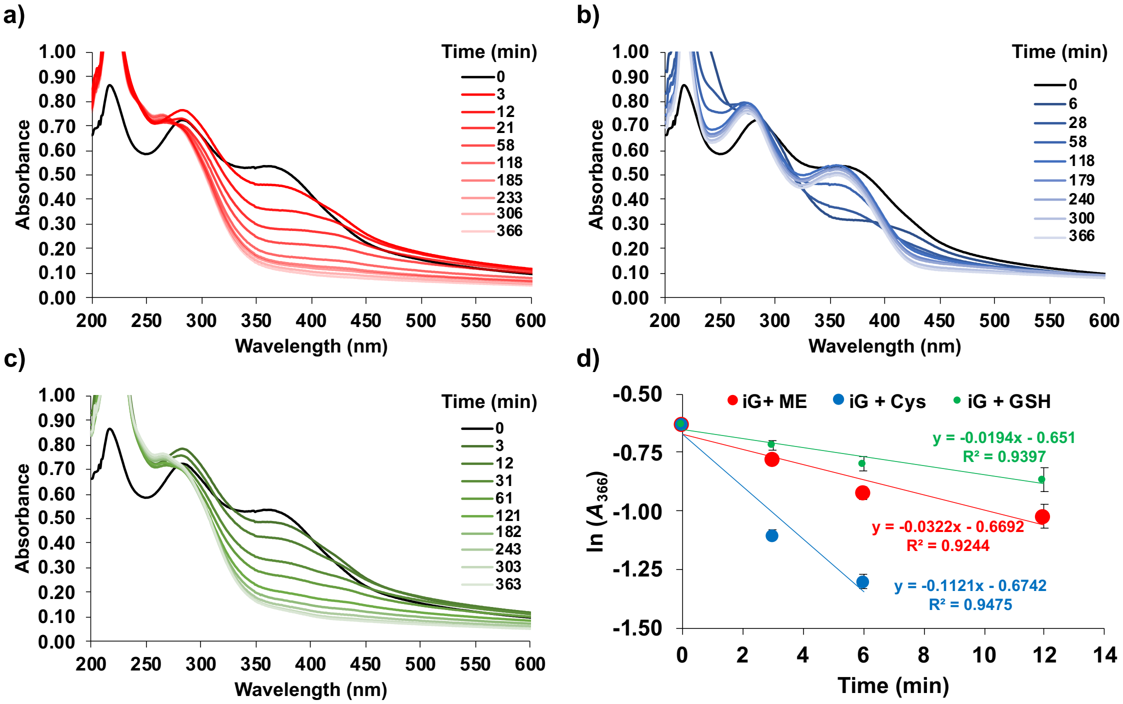

Figure 3.3. Time-dependent UV-Vis spectra for 50 µM **iG** in 1% MeOH in PBS, pH 7.4 with: **a)** 1 mM **ME**, **b)** 1 mM **Cys**, **c)** 1 mM **GSH**. Panel **d)** shows pseudo-first order kinetic plots, whose slopes equal -k, from which we get pseudo-first order rate constants of reaction.

From here, we obtained the rate constants and reactions half-lives of reaction in Figure 3.2d. The response with Cys was initially fast ($t_{1/2}$ = 6 min). This fast-initial rate could be attributed to Cys having the lowest thiol pK_a compared to ME and GSH (8.3, 9.6, and 9.7, respectively).[17] It has been shown that the thiols with lower pK_a the faster the thiol-Michael reaction rate due to the nucleophile being mainly in the thiolate, which is a better nucleophile.[10] We saw reversibility of the reaction and a blue shift in the UV-Vis spectrum (Figure 3.3); this behavior only occurred with Cys (Figure 3.3b). It is possible that once Cys reacts through the thiol Michael addition, it cyclizes via an intramolecular nucleophilic attack of its amino group into the neighboring ketone in **1**, forming a seven-membered 1,4-thiazepine as reported with cysteamine and chalcones.[18]

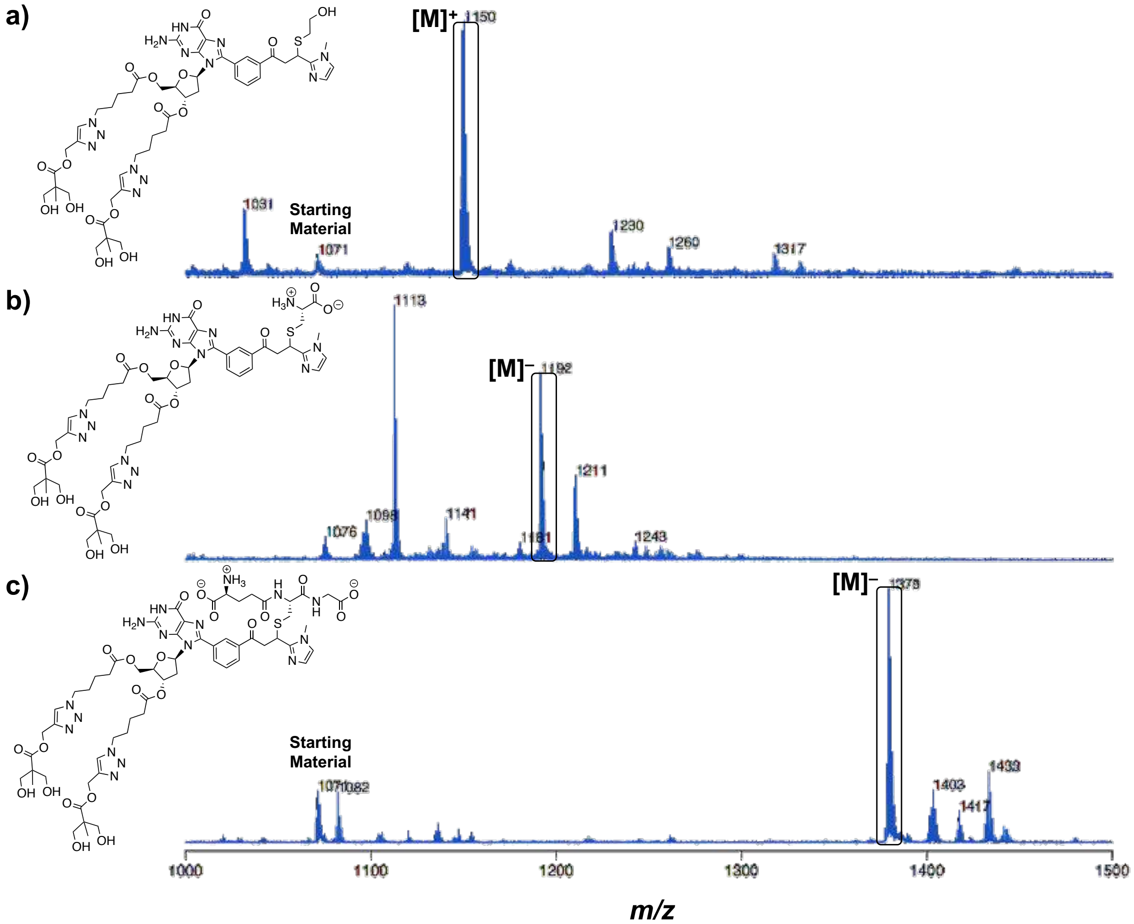

Figure 3.4. MALDI-TOF Mass Spectrometry graphs for thiol adducts a) **iG-ME** (**2**) (positive mode), b) **iG-Cys** (**3**) (negative mode), and c) **iG-GSH** (**4**) (negative mode).

The reactions with **ME** and **GSH** eventually reached equilibrium, the kinetics being faster for **ME** ($t_{1/2}$ = 22 min) than for GSH ($t_{1/2}$ = 36 min), which can be attributed mainly to steric bulk since the pK_a of the thiols for both species is relatively similar are 9.6 and 9.2, respectively.[8] The rate constants for the reaction of **iG** with these three thiols are similar to those of reported GSH probes.[19] Additional evidence of reaction comes from mass spectrometry studies where we see the molecular ions corresponding to **iG-ME**, **iG-Cys**, and **iG-GSH** (Figure 3.4).

Seeing this behavior of the **iG** + Cys reaction, we decided to explore the thiol-Michael reaction's reversibility or retro thiol-Michael reaction. The elimination of **ME** from **iG-ME** can be seen in Figure 3.2e. Following the same absorption band (365 nm) but with the opposite trend (Figure 3.2f), we generated first-order kinetic plots (Figure 3.2g) and obtained rate constants and hal*f*-lives for the retro Michael reaction (Figure 3.2h). We calculated the half-life of the retro thiol-Michael reaction with thiol conjugates to increase with the size of the conjugated thiol **iG-GSH** > **iG-Cys** > **iG-ME**. The decreased kinetics of elimination could be explained by the increasing steric bulk from a relatively small thiol like **ME** to a bigger thiol such as **GSH**. The thiol-Michael reaction is reversible with **iG**. The retro Michael reaction's rate constants are like those of reported GSH probes as of the forward reaction.[19] Now that we know **iG** reacted with these thiols, we wanted to confirm that the product that was forming was the thiol conjugate. Spectra via ^{1}H NMR confirms this by shifting the vinylic protons from the NMR's aromatic region. (Figures 3.5 - 3.8).

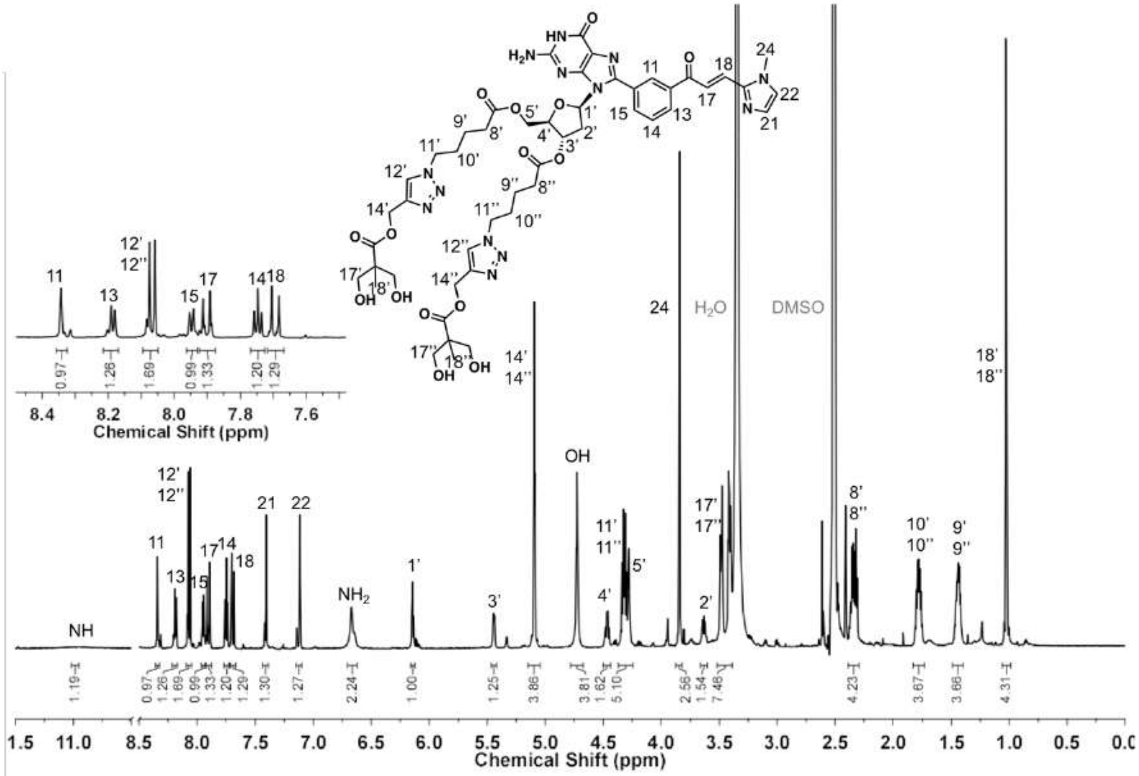

Figure 3.5. ^{1}H NMR spectrum of **iG** (700 MHz, DMSO-d$_6$, 298.2 K).

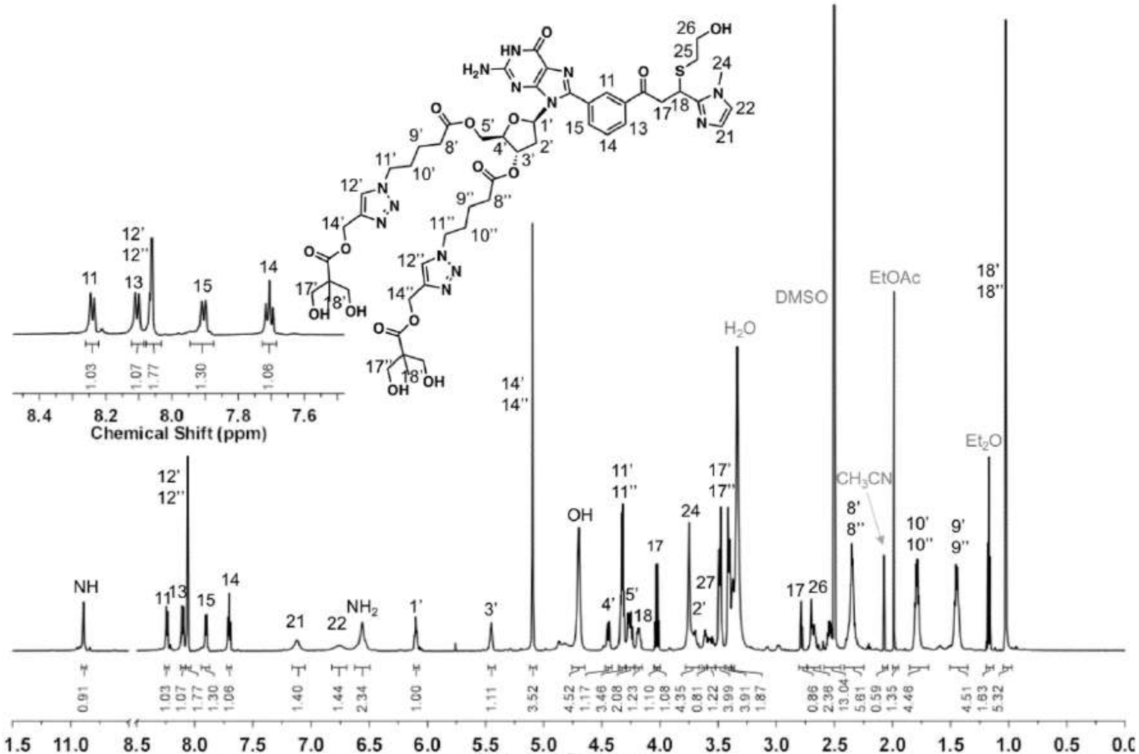

Figure 3.6. ^{1}H NMR spectrum of **iG-ME** (700 MHz, DMSO-d$_6$, 298.2 K)

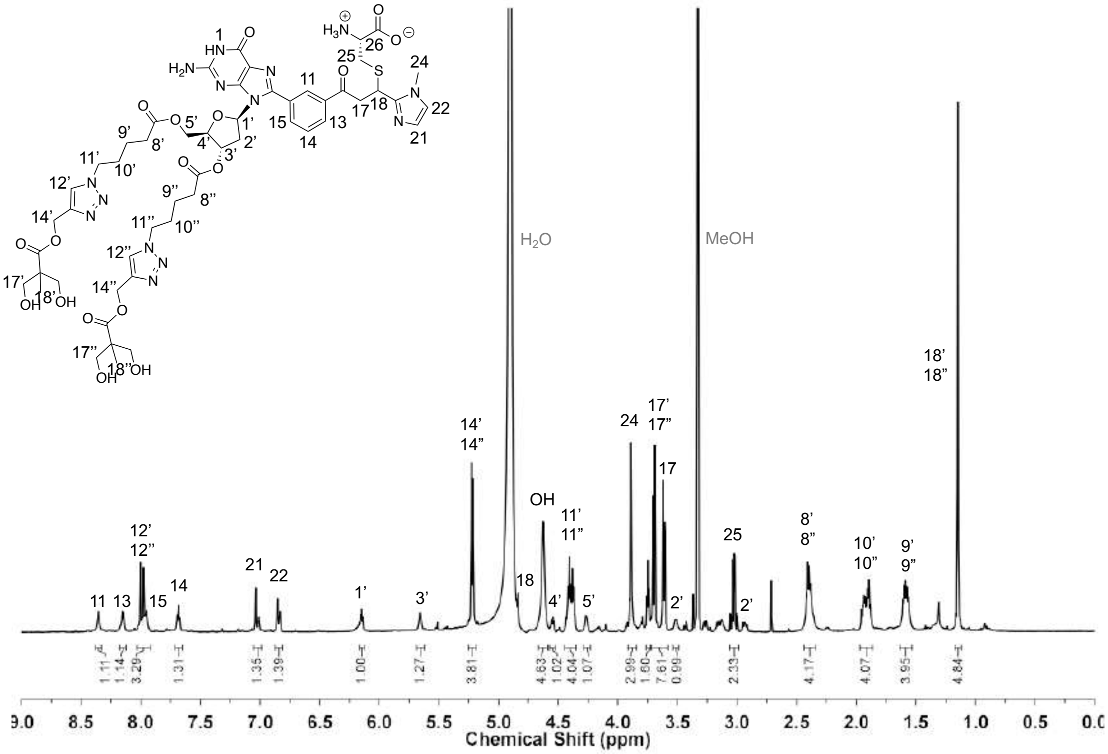

Figure 3.7. ^{1}H NMR spectrum of **iG-Cys** (700 MHz, MeOD-d$_4$, 298.2 K).

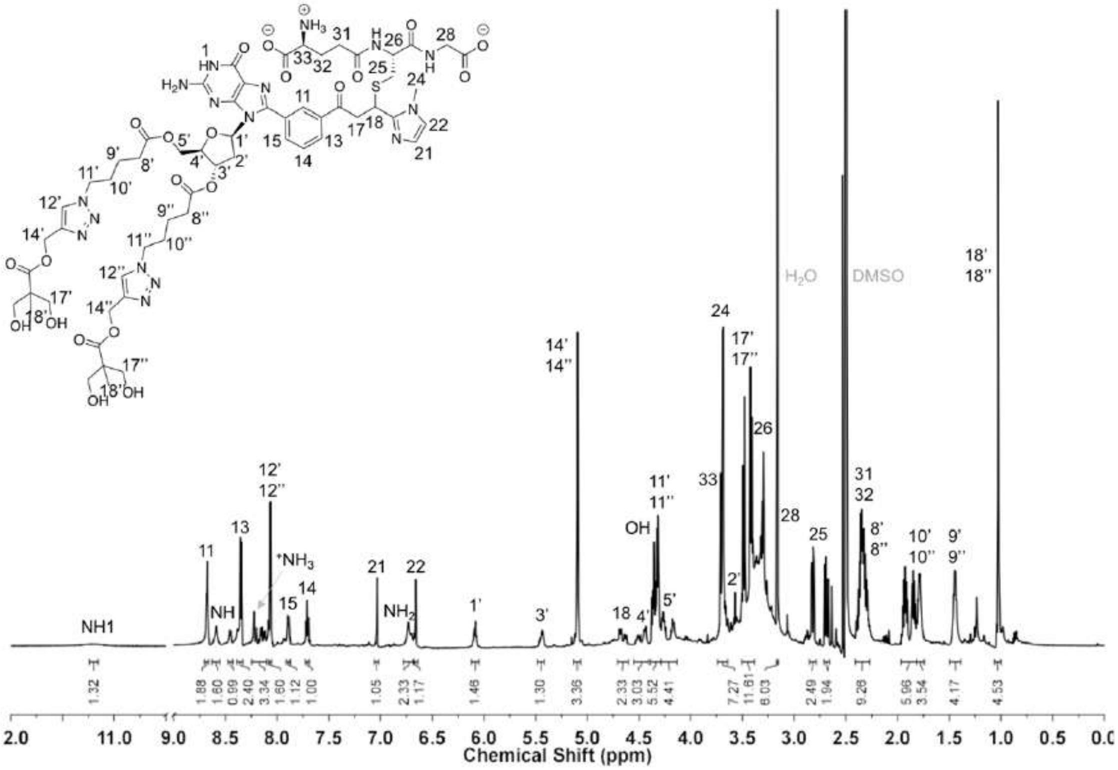

Figure 3.8. ^{1}H NMR spectrum of **iG-GSH** (700 MHz, DMSO-d$_6$, 298.2 K).

3.3.2. SGQ reactions

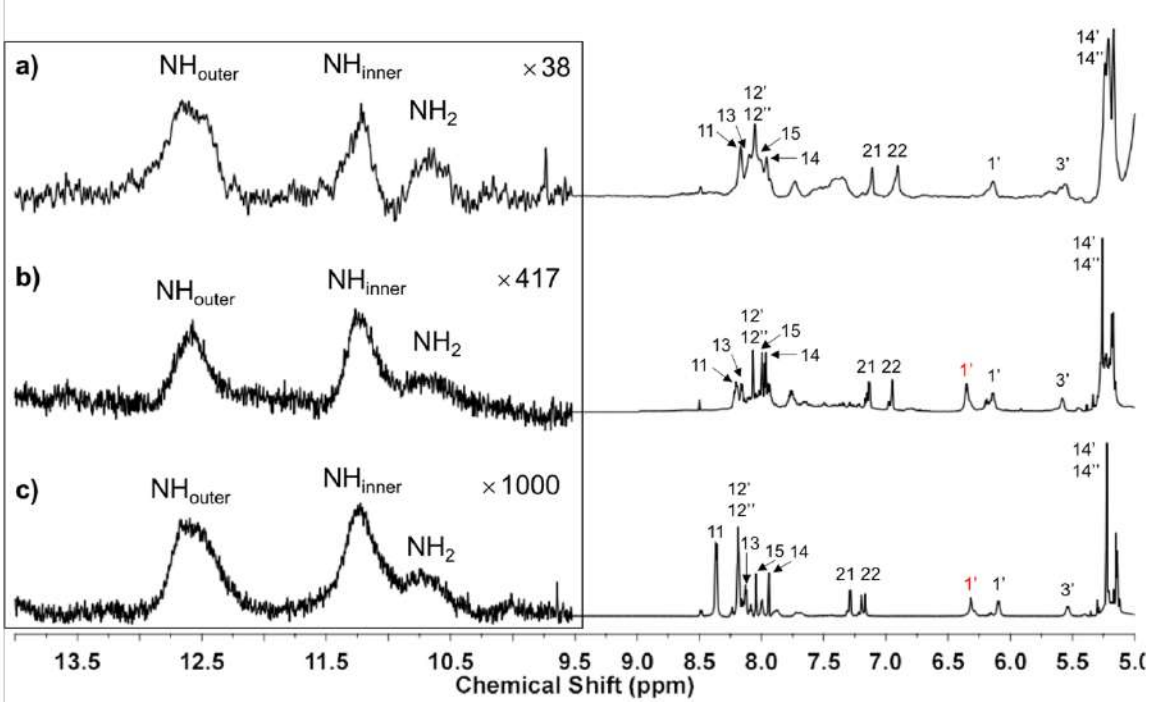

Figure 3.9. Partial ^{1}H NMR spectra (700.13 MHz) for a) **iG-ME** (3.2 mM, 1.3 M KI), b) **iG-Cys** (2.5 mM, 1 M KI), c) **iG-GSH** (5 mM, 1 M KI). All samples are dissolved in PBS, pH 7.4 pH 7.4 with 10% D_2O at 298.2 K. The zoom of the region from 9.5-14.0 ppm is relative to the intensity of the peak at 5.22 ppm (labeled: 14', 14"). Peak legend corresponds to protons labeled in the Figures 2.5 – 2.8 for the respective thiol conjugate.

Once we had the thiol conjugates, we decided to self-assemble the monomers by adding potassium iodide (KI) along with PBS, pH 7.4 (pH 7.4) to see if these self-assembled into SGQs. Usually, **iG** self-assembles into soluble octameric SGQs in aqueous media under its LCST with 2 M of KI.[20,21] The LCST is due to the outward-projecting second-generation dendrons, which have hydrophilic hydroxyl groups that aid in water solubility. Upon adding PBS, pH 7.4 and KI, adduct 2 enters into solution once the solution is left at 0 - 4 °C for over 4 hours. Meanwhile, adducts 3 and 4 appeared to dissolve immediately. The time needed to achieve self-assembly starks contrast with 1, which does not enter in solution after a 12 to 24-hour period of stabilization under 2 °C. The thiol conjugate adducts appear to be hydrophilic enough to be water-soluble or soluble sufficiently to quickly self-assemble.

Water suppression ^{1}H NMR was carried out on these solutions. To look for assembly evidence, we look at the N1H region (10 – 14 ppm). The peaks corresponding to the N1H protons are distinctive of an SGQ assembly and gives us information about the SGQ molecularity.[22] As shown in Figure 3.9 for **SGQ-iG-ME**, **SGQ-iG-CYS** and **SGQ-iG-GSH**, we see two N1H signals, along with the compromised (in the G-tetrad) NH2 signal. Two N1H signals are consistent with a hexadecameric assembly.[23] This type of assembly has four G-tetrads: the two outer tetrads and two inner tetrads, for a total of sixteen (16) G-derivatives subunits. The outer tetrads experience a similar chemical environment. The same is true for the inner tetrads, but the chemical environment is different for the outer and inner tetrads. Different chemical environments explain the chemical shift's difference for these tetrad H-bond locked. Outer tetrad N1H signals are of a higher chemical shift due to the greater exposure to the highly polar aqueous environment. It is important to note that **iG** form hexadecameric SGQs at neutral pH, while all the thiol conjugates form hexadecameric SGQs at the same pH.[20]

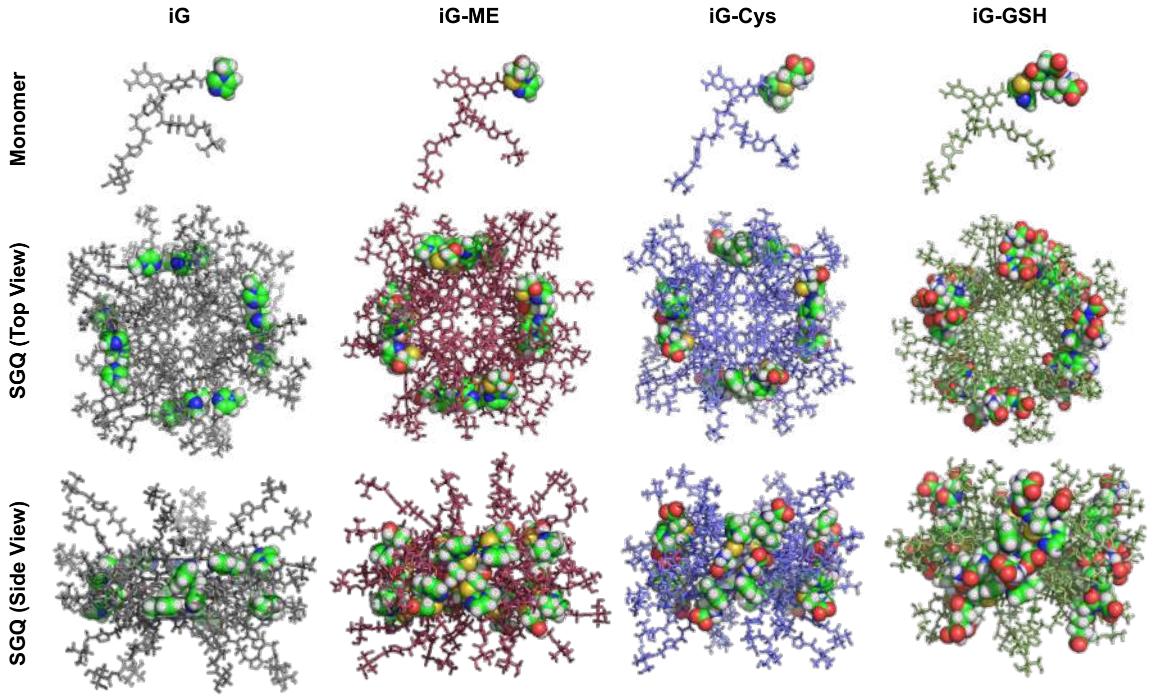

Figure 3.10. Molecular modeling of all monomers and their corresponding SGQs. The space-filling atoms highlight the atoms added by each corresponding thiol, including the methylimidazole moiety. The molecular model representations were minimized using: OPLS_2005 (MacroModel), Version Maestro 9.3.5; Schrödinger, LLC: New York, 2007, representing the water as continuum.[24,25]

Surprisingly conjugate **iG-GSH** was able to assemble into an SGQ given the great steric bulk of the added GSH moiety. For this reason, and to further support the assembly studies, we did molecular modeling (Figure 3.10) of **iG** and thiol conjugates and SGQs. From left to right, starting from **SGQ-iG-ME** to **SGQ-iG-GSH**, we see an increased crowding in the center of the SGQ due to the accommodation of the newly added groups in the chalcone region of monomer 1, which are more prominent in the order **GSH** > **Cys** > **ME (iG-GSH** > **iG-Cys** > **iG-ME**). All structure's steric hindrance appears consistent with the experimental NMR data. It is reasonable to conclude that the higher the steric hindrance in that region, the more difficult it is to produce a stable SGQ.

3.3.3. Thermo-responsive properties

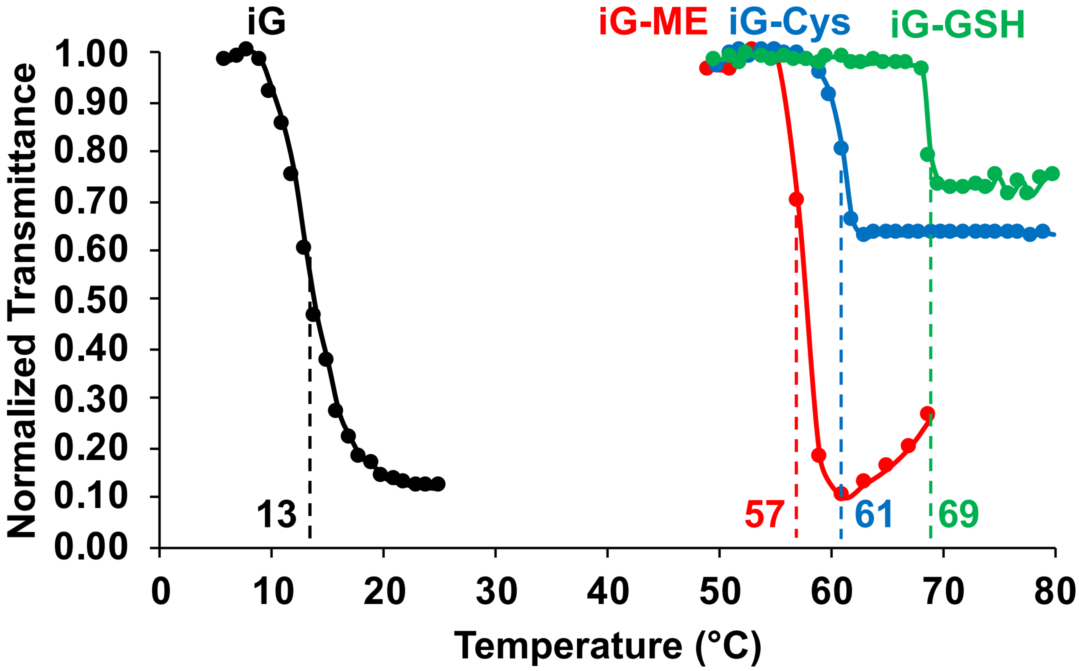

Figure 3.11. Turbidimetry studies for different SGQ solutions as a function of temperature. All solutions used 5 mM of the G-derivative dissolved in PBS, pH 7.4. The solutions of SGQ of **iG** and **iG-ME**, were 2 M in KI, while those of **iG-Cys** and **iG-GSH** were 1 M KI.

As **iG-ME**, **iG-Cys**, and **iG-GSH** form SGQs, we need to understand if formed SHS have any thermal response as LCST and how the LCST has changed from **SGQ-iG** due to the less hydrophobic new compounds. As compounds are more hydrophobic, less energy is needed to strip the hydration shell of water molecules that solvate the SGQs to get them out of solution and form the colloidal SHS particles.[26,27] We hypothesized that these new conjugates would have higher transition temperatures than **SGQ-iG**. Turbidity experiments were carried out, in which the transmittance of the solution is measured as a function of temperature.

When the solution turns cloudy due to colloidal SHS particles formation, the transmittance goes down as we see SGQ to SHS particle transition. The temperature for this transition is called the cloud-point temperature (T_{cp}) and is related to the LCST.

Turbidity experiments show a cloud-point temperature for **SGQ-iG-ME** of 57 °C at pH 7.4 (Figure 3.11). The **SGQ-iG-ME** shows a 44 °C difference in comparison with **SGQ-iG** T_{cp} of 13 °C. This high transition temperature is characteristic of less hydrophobic SGQs because a higher temperature is needed to destabilize the SGQ-water interactions. A transition temperature higher than body temperature (37 °C) means that upon the reaction of **SHS-iG** with GSH in the cell, the formation of a less hydrophobic SGQ will lead to the SHS particles disassembly due to greater solubility or the SGQ. Another possibility is not one of disassembly but increased porosity and enhanced release. The **SGQ-iG-Cys** and **SGQ-iG-GSH** also exhibit high cloud-point temperatures (61 and 69 °C, respectively). The decrease in transmittance for both these SGQs is not as drastic as for **SGQ-iG** and **SGQ-iG-ME** The low transmittance change is consistent with a lower concentration of assembled monomers into SGQs. The high solubility of the G-derivatives leads to low SGQ assembly as the magnification in Figure 3.9 expansions in exposes. Temperatures have also to be considered as the transmittance change could be due to the melting of the SGQs that are part of the SHS particle at temperatures above 60 °C.[12] The turbidity curve for **SGQ-iG-ME** after 60 °C is evidence of this, as the transmittance starts to increase above this temperature. Therefore, fewer SGQs available to form their corresponding SHS particle.

3.3.4. SHS characterization

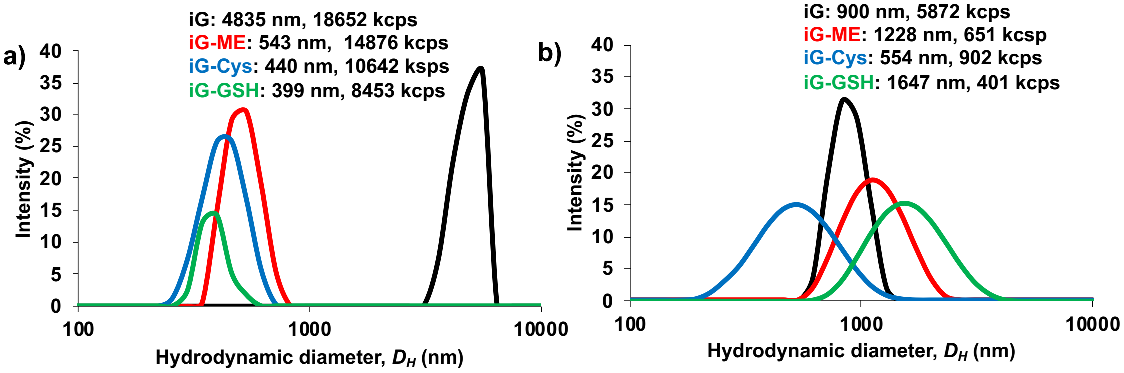

Figure 3.12. Hydrodynamic diameters and derived count rate (kcps) for **SHS-iG** and thiol SHS particles a) before (5 mM, 2 M KI; 40 °C for **iG**, 65 °C for thiol derivatives **SHS-iG-ME** and **SHS-iG-Cys**, 70 °C for **SHS-iG-GSH**) and (b) after (0.300 mM, 120 mM, 25 °C) fixing.

After confirming the formation of SHS particles, we decided to characterize using DLS (Figure 3.12). All thiol conjugates lead to smaller SHS particles than the parent **SHS-iG** ranging in diameter from ~400 to 550 nm, with populations showing also showing narrower distributions (Figure 3.12a). Consistent with the amount of SGQs formed for each bioconjugate and the turbidity experiments, we noticed a decreased peak intensity in the order **SHS-iG-ME** > **SHS-iG-Cys** > **SHS-iG-GSH**. DLS data also shows us the derived count rate as a particle count after T_{cp} of each SGQ. The derived count rate also shows a parallel trend of **SHS-iG-ME** > **SHS-iG-Cys** > **SHS-iG-GSH**. We have previously reported a method for kinetically stabilizing the SHS particles in a manner that can allow their manipulation at lower temperatures without disassembling and dissolving.[11,13] We term this process "fixing" (*f*), since it fixes the current state trapping the SGQ constituents within the

SHS particles in a metastable state, by merely lowering the solution's ionic strength via dilution.[28] Sample of ***f*-SHS-iG** particle shows a size reduction and much less polydisperse than its non-fixed counterpart (Figure 3.12b). Upon fixing, ***f*-SHS-iG-Cys** particle changed very little in size, while the ***f*-SHS-iG-ME** and the ***f*-SHS-iG-GSH** particles increased drastically in size. All the *f*-SHS particles decrease their abundance as an inverse function of their hydrophobicity, with the most hydrophobic producing lower concentrations particles (Figure 3.12).

The reason thiol-SHS particle are smaller than 1-SHS is due to their less hydrophobic nature. The smaller they are, the more surface area is exposed to water. The **SHS-iG**, being more hydrophobic, are bigger to "shield" the hydrophobic **iG** from the water, akin to the hydrophobic effect for proteins. Upon fixing, the ionic strength of the solution is lowered. Thus, *f*-SHS particles formed from more hydrophobic compounds will decrease in size because the environment is now less polar, while SHS particles formed from less hydrophobic adducts will increase in size for the opposite reasons.

3.3.5. SHS thiol-responsive properties

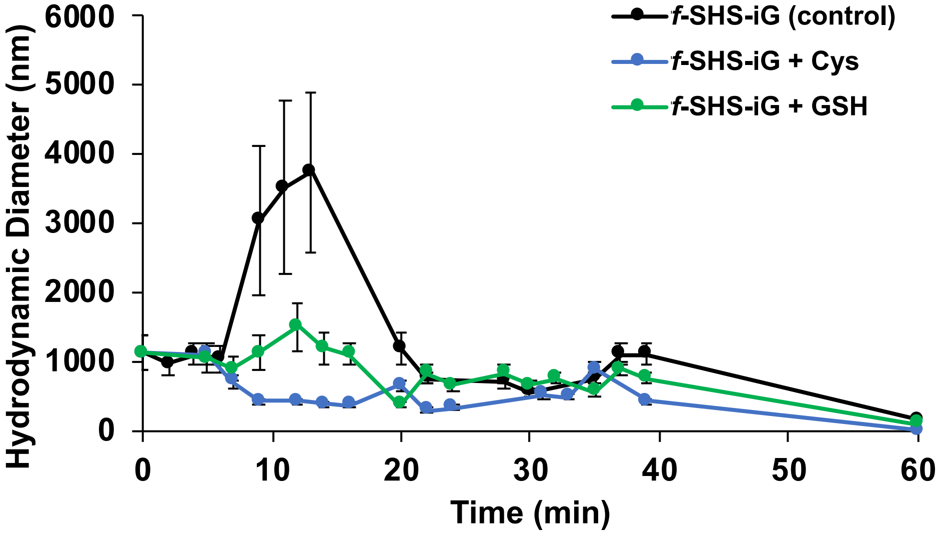

Figure 3.13. Hydrodynamic diameters of 0.45 mM ***f*-SHS-iG** (180 mM KI) in the presence of 5 mM Cys or GSH as a function of time (PBS, pH 7.4, 37 °C). Error bars correspond to polydispersity in size from single measurements (average of ~12 runs) of the same sample.

As we have shown how **iG** is thiol responsive, it's expected for the **SHS-iG** is also thiol responsive. Since these thiol conjugates have a higher cloud point than **iG**, the SHS particles should isothermally disassemble into SGQs given that the temperature is below the cloud point of the resulting SGQ in the SHS particles. This strategy can be used as a stimulus for cargo release from the SHS particle, which can be an application for drug delivery. To test this hypothesis, we measured the size of ***f*-SHS-iG** by DLS in the presence of 5 mM Cys or GSH (Figure 3.13) as GSH is in high concentrations in the cell cytoplasm (1 - 10 mM).[29] We did not see a statistically significant change in the size of ***f*-SHS** after the addition of either thiol compared to control after two hours.

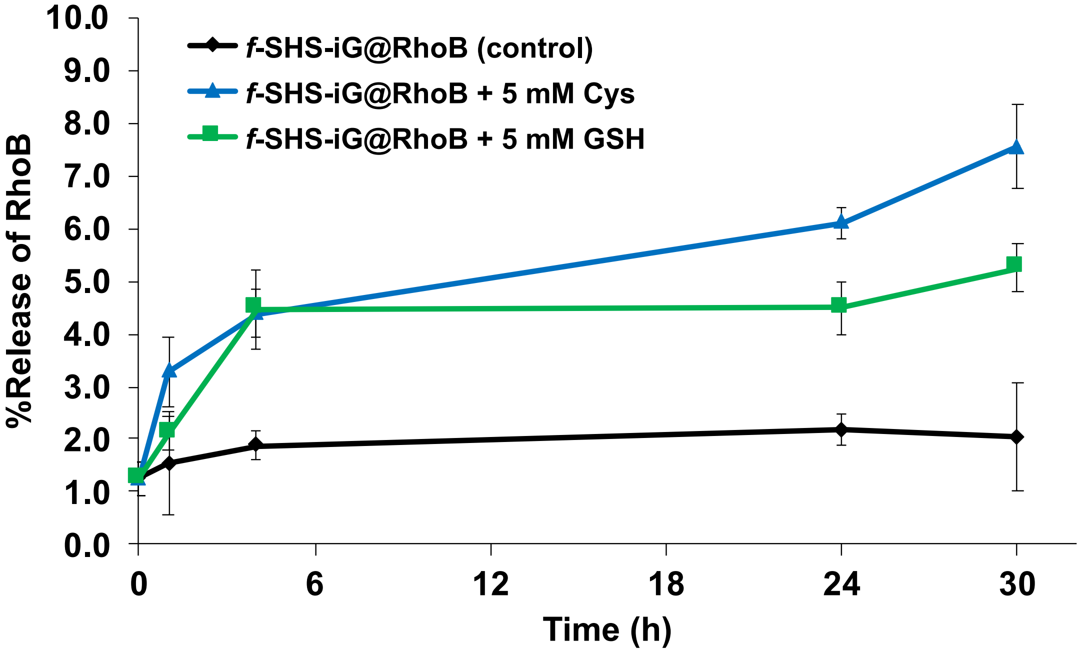

Figure 3.14. Percent release of Rhodamine B from 0.833 mM ***f*-SHS-iG** (333 mM KI) into aqueous phase in the presence of 5 mM Cys or GSH in PBS, pH 7.4.

Nonetheless, we wanted to see if, after encapsulating a cargo molecule such as a dye, an addition of thiol would increase the percent of cargo released from the *f*-SHS. For this, we encapsulate **RhoB** into the SHS particles, and later fix the **SHS-iG@RhoB** into ***f*-SHS-iG@RhoB**. Here we see an enhanced release of **RhoB** from ***f*-SHS-iG** particles upon addition of 5 mM Cys or GSH compared to control with Cys having a more significant effect on release than GSH after the 24 hours (Figure 3.14).

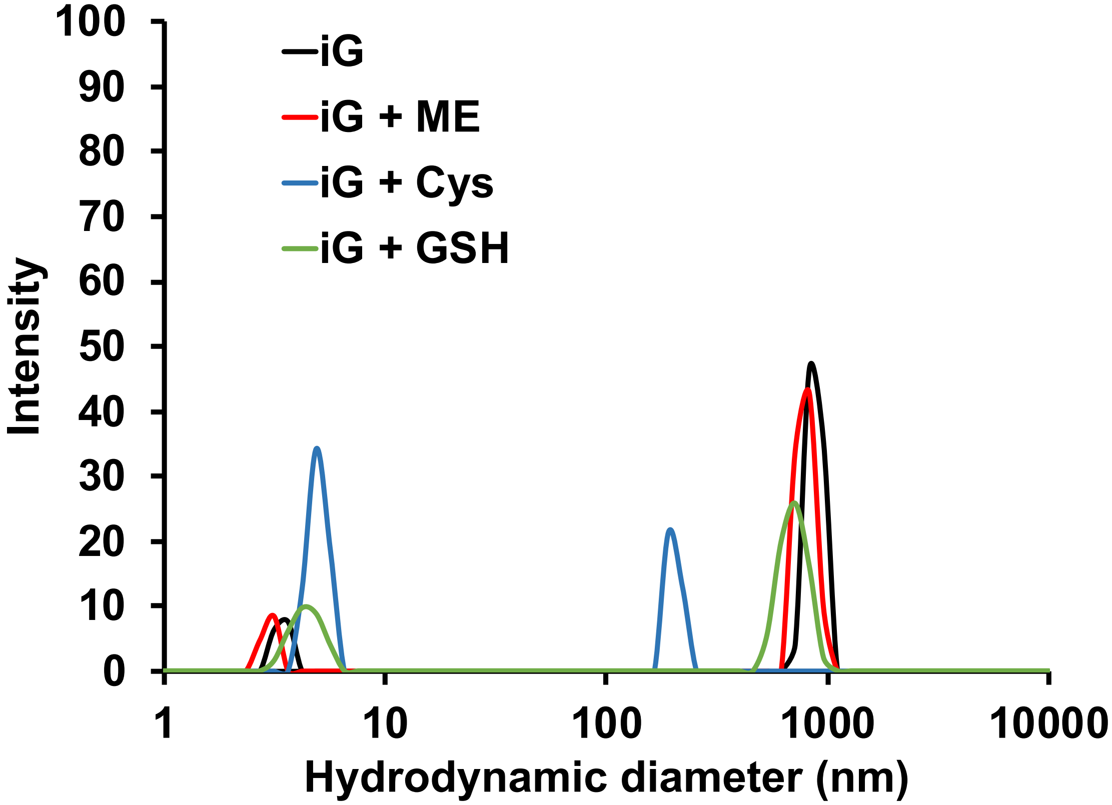

Figure 3.15. Time-dependent dynamic light scattering experiments for **iG** SHS (5 mM, 2 M KI) **a)** no thiol added; with 5 mM **b)** ME, **c)** Cys, **d)** GSH; in PBS, pH 7.4, 40 °C.

Although size measurements did not show a significant decrease in size or disassembly of **SHS-iG** particles in the presence of thiols for exception of GSH (Figure 3.15), we did see an enhanced release of **RhoB** (Figure 3.14). The higher release of **RhoB** achieved 7% of 5 mM of Cys after 30 h. We can understand that the diffusion of these thiols into SHS particles and subsequent reaction with the **iG** subunits might lead to SHS particles porosity. This mechanism explains the lack of change in size and the increased dye release: the thiols could be causing an “internal erosion” of the SHS particles, leading to increased porosity of the particles without changing the size (Figure 3.16). This increased porosity accounts for the enhanced release with thiols. These results highlight the biothiol responsive properties of SHS particles as a trigger for cargo release. In the future, this knowledge could be used to improve cargo release from SHS and use this strategy as a drug delivery stimulus.

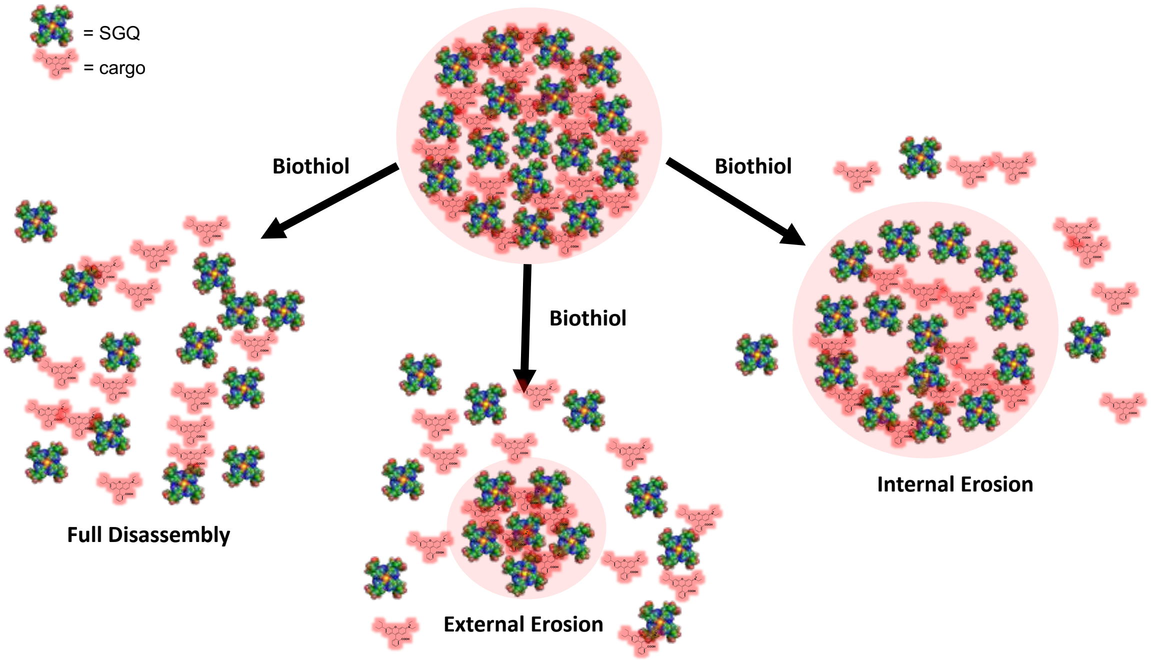

Figure 3.16**.** Possible pathways of SHS particles cargo release in the presence of thiols. These pathways also apply for reaction with GSH.

3.4. Conclusions

G-derivative **iG** has shown significant promise as a molecule responsive to thiols such as ME, Cys, and GSH, as UV-Vis experiments show. Nonetheless, DLS studies demonstrated that *f*-SHS particles do not significantly change in size in the presence of 5 mM Cys or GSH. Nevertheless, despite the lack of the anticipated size reduction, the enhanced release of encapsulated **RhoB** in the presence of biothiols support the responsive behavior. The likely mechanism being one of bulk erosion throughout the SHS particles, which in turn lead to higher release kinetics (Figure 3.16).

The use of the thiol-Michael reaction has the potential for new strategies of drug delivery by expanding the variety of thiol conjugates in SHS particles. For example, the response of **iG** with thiols linked to a drug can lead to covalently-linked trapping of a drug. The guanosine moiety provides the self-assembly into SGQs and then form SHS particles due to the ester chains attached at the O3' and O2' of the sugar.[12] As long as these are present, there is great flexibility in encapsulating different cargoes via in situ methods or via diffusion into previously made SHS particles as we have reported.[11] The thiol-Michael addition has proved to be reversible for **iG**. The thiol-adducts produce unstable and more hydrophilic supramolecular structures than **iG**. This reaction provides a tool for modulating the hydrophobic-hydrophilic interactions of SGQs with water. However, the thiol-adduct with the G-derivative lead to unstable SGQs, which in turn triggers disassembly and cargo release. The introduction of a thiol-responsive SHS particles opens the door for a turn-on fluorescence sensor due to the extended conjugation of an α,β-unsaturated system to prompt self-assembly in isothermal conditions or as a way to expand its biomedical applications such as their use as an HIV-1 vaccine adjuvant.[15]

3.5. Experimental section

3.5.1. General Experimental Procedures.

Unless otherwise specified, all reagents and solvents were obtained from commercial sources and used without further purification. All compounds were purified by column chromatography on silica gel 60 (0.04-0.063 mm) unless otherwise noted. TLC (from Sorbent Technologies) was performed using EMD silica gel 60 F254 glass-backed plates from Sorbent Technologies. Visualization of spots was effected with UV light and iodine. Reactions requiring anhydrous conditions were carried out using flame-dried glassware under argon gas.

3.5.2. Synthesis.

*3.5.2.1. Synthesis of **iG**.*

G-derivative **iG** preparation as previously describes in Scheme 2.1 and previously repoted.[15,20,21] Yield 65 %. δ 10.96 (s, 1H), 8.36 – 8.32 (m, 1H), 8.19 (dt, *J* = 7.9, 1.3 Hz, 1H), 8.07 (d, *J* = 11.5 Hz, 2H), 7.95 (dd, *J* = 7.5, 1.5 Hz, 1H), 7.90 (dd, *J* = 15.1, 3.4 Hz, 1H), 7.75 (t, *J* = 7.7 Hz, 1H), 7.72 – 7.67 (m, 1H), 7.41 (d, *J* = 8.9 Hz, 1H), 7.13 (d, *J* = 19.4 Hz, 1H), 6.66 (d, *J* = 20.4 Hz, 2H), 6.14 (t, *J* = 7.0 Hz, 1H), 5.44 (dt, *J* = 6.9, 3.2 Hz, 1H), 5.09 (d, *J* = 4.0 Hz, 4H), 4.72 (t, *J* = 5.5 Hz, 4H), 4.46 (q, *J* = 7.9 Hz, 2H), 4.37 – 4.24 (m, 5H), 3.84 (d, *J* = 5.9 Hz, 3H), 3.63 (dt, *J* = 14.0, 7.0 Hz, 2H), 3.45 (ddt, *J* = 50.9, 10.0, 4.4 Hz, 7H), 2.39 – 2.29 (m, 4H), 1.83 – 1.73 (m, 4H), 1.49 – 1.40 (m, 4H), 1.03 (d, *J* = 3.7 Hz, 4H).

*3.5.2.2. Synthesis of **iG-ME**.*

iG (5 mg, 0.0051 mmol) was dissolved in 2-mercaptoethanol (ME, 2 mL, 0.028 mmol) and left stirring overnight. Then, ME was removed by rotary evaporation and the resulting yellow oil was washed with diethyl ether three times. The light-yellow solid was left in vacuum to remove any remaining ME. No further purification was performed. Yield: 25 %. δ 10.89 (s, 1H), 8.24 (dd, *J* = 8.1, 2.0 Hz, 1H), 8.11 (d, *J* = 7.9 Hz, 1H), 8.06 (d, *J* = 5.0 Hz, 2H), 7.95 – 7.87 (m, 1H), 7.71 (t, *J* = 7.7 Hz, 1H), 7.12 (s, 1H), 6.76 (s, 1H), 6.56 (s, 2H), 6.10 (td, *J* = 7.0, 3.4 Hz, 1H), 5.46 (qt, *J* = 6.7, 3.6 Hz, 1H), 5.09 (s, 4H), 4.76 – 4.65 (m, 5H), 4.44 (dd, *J* =

11.7, 4.6 Hz, 1H), 4.35 – 4.30 (m, 3H), 4.29 – 4.22 (m, 2H), 4.18 (ddt, *J* = 11.5, 8.0, 4.0 Hz, 1H), 4.03 (q, *J* = 7.1 Hz, 1H), 3.78 – 3.66 (m, 4H), 3.61 (q, *J* = 6.5 Hz, 1H), 3.56 (dq, *J* = 20.9, 6.9 Hz, 1H), 3.49 (dd, *J* = 11.4, 3.3 Hz, 4H), 3.41 (d, *J* = 10.1 Hz, 4H), 3.37 (d, *J* = 5.8 Hz, 2H), 2.79 (t, *J* = 6.6 Hz, 1H), 2.73 – 2.62 (m, 2H), 2.50 (p, *J* = 1.9 Hz, 13H), 2.42 – 2.25 (m, 6H), 2.07 (s, 1H), 1.99 (s, 1H), 1.79 (qt, *J* = 7.2, 5.1, 3.8 Hz, 4H), 1.51 – 1.35 (m, 4H), 1.17 (t, *J* = 7.1 Hz, 2H), 1.03 (d, *J* = 1.9 Hz, 6H).

*3.5.2.3. Synthesis of **iG-Cys** and **iG-GSH**.*

Compound **iG** (5 mg, 0.0051 mmol) was dissolved in 1 mL methanol. Then, 20 equivalents of L-cysteine (Cys, to synthesize **iG-Cys**) or L-glutathione (GSH, to synthesize **iG-GSH**) were added and left stirring. In the case of **iG-Cys**, the reaction is done after one day. For **iG-GSH**, the reaction is left stirring for five days. Afterwards, the liquid crude was centrifuged, and the supernatant filtered through 0.45 µm Nylon filters. Finally, the methanol was removed by rotary evaporation and the light-yellow solids were left in high vacuum. No further purification was performed. **iG-Cys** yield 65 %. δ 8.35 (s, 1H), 8.15 (d, *J* = 7.9 Hz, 1H), 7.98 (dd, *J* = 18.8, 16.4 Hz, 3H), 7.68 (t, *J* = 7.8 Hz, 1H), 7.02 (d, *J* = 17.8 Hz, 1H), 6.84 (d, *J* = 14.3 Hz, 1H), 6.15 (t, *J* = 6.8 Hz, 1H), 5.66 (dt, *J* = 7.8, 4.1 Hz, 1H), 5.22 (d, *J* = 8.2 Hz, 4H), 4.63 (s, 5H), 4.55 (dd, *J* = 11.7, 5.1 Hz, 1H), 4.39 (ddd, *J* = 24.0, 11.7, 6.7 Hz, 4H), 4.26 (q, *J* = 5.2 Hz, 1H), 3.91 – 3.84 (m, 3H), 3.75 (dd, *J* = 6.2, 4.2 Hz, 2H), 3.66 (ddd, *J* = 59.1, 10.9, 2.3 Hz, 8H), 3.51 (p, *J* = 6.8, 6.2 Hz, 1H), 3.19 – 3.08 (m, 2H), 3.07 – 2.98 (m, 2H), 2.93 (dd, *J* = 14.2, 8.4 Hz, 1H), 2.39 (ddd, *J* = 19.0, 15.0, 9.4 Hz, 4H), 1.92 (ddd, *J* = 30.3, 14.6, 7.0 Hz, 4H), 1.59 (tt, *J* = 16.1, 7.7 Hz, 4H), 1.15 (s, 5H). **iG-GSH** yield 61 %. 1H NMR (700 MHz, DMSO-*d*$_6$) δ 11.22 (s, 1H), 8.68 (t, *J* = 5.8 Hz, 2H), 8.36 (d, *J* = 8.3 Hz, 2H), 8.07 (q, *J* = 2.6 Hz, 2H), 7.92 – 7.88 (m, 1H), 7.71 (t, *J* = 7.8 Hz, 1H), 7.07 – 7.02 (m, 1H), 6.72 (d, *J* = 22.0 Hz, 2H), 6.69 – 6.65 (m, 1H), 6.09 (dt, *J* = 11.0, 6.9 Hz, 2H), 5.49 – 5.42 (m, 1H), 5.10 (d, *J* = 1.7 Hz, 3H), 4.66 (ddd, *J* = 35.2, 10.2, 3.9 Hz, 2H), 4.55 – 4.41 (m, 3H), 4.39 – 4.30 (m, 6H), 4.30 – 4.14 (m, 4H), 3.75 – 3.65 (m, 7H), 3.51 – 3.39 (m, 12H), 3.17 (s, 6H), 2.83 (dd, *J* = 13.6, 4.7 Hz, 2H), 2.69 (dd, *J* = 13.6, 8.4 Hz, 2H), 2.42 – 2.27 (m, 9H), 1.89 (ddt, *J* = 55.4, 13.6, 6.6 Hz, 6H), 1.82 – 1.75 (m, 3H), 1.45 (h, *J* = 7.2 Hz, 4H), 1.03 (d, *J* = 2.2 Hz, 4H).

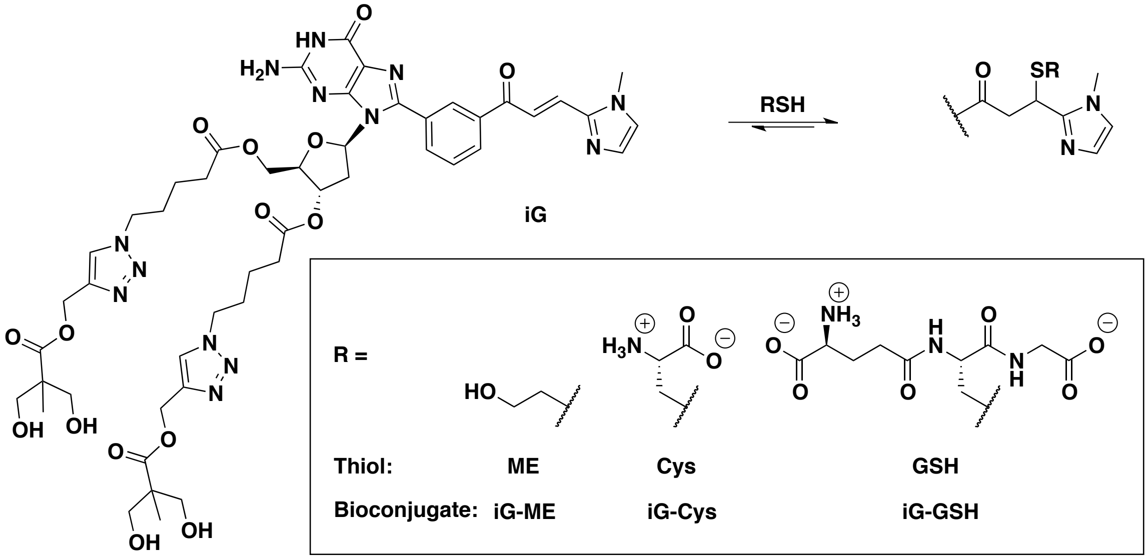

Figure S3.1. Synthetic scheme for thiol adducts (**iG-ME**, **iG-Cys**, and **iG-GSH**). **ME** = 2-mercaptoethanol; **Cys** = L-cysteine; **GSH** = glutathione.

3.5.3. SGQ NMR Characterization

^{1}H and ^{13}C NMR spectra were recorded on a Bruker Ascend Aeon 700 or 500 (TopSpin v 2.0) with nominal frequencies of 700 or 500 MHz for proton and 126 or 90 MHz for carbon, respectively. ^{1}H and ^{13}C NMR chemical shifts are reported in ppm relative to the undeuterated solvent as an internal reference.

Sodium 3-(trimethylsilyl)propionate-2,2,3,3-d_4 (Aldrich) was used as the internal standard for the NMR experiments performed in H_2O:D_2O (9:1). A conventional 1D presaturation pulse sequence with the excitation pulse set over the water peak at 4.7 ppm was used in water. All NMR experiments were performed at 298.2 K unless otherwise stated.

3.5.4. Self-assembly studies

Solutions with 5 mM of monomer (**iG** - **iG-GSH**) and 1 - 2 M KI in PBS, pH 7.4 (650 µL) were prepared and stored at 0 °C for self-assembly into their corresponding SGQ. After the compound was dissolved entirely, NMR experiments were done. Water suppression ^{1}H NMR of these samples show characteristic NH1 peaks corresponding to the molecularity of the resulting SGQ (octamer, hexadecamer, etc.).

3.5.5. SHS particles Preparation, Fixing, and Encapsulation and Release

To form SHS particles, once we had SGQ solutions of **iG** - **iG-GSH**, we heated the solution above the LCST of the corresponding SGQ to form the colloidal SHS particles. For **iG**, we heated to 40 °C; for thiol conjugates, we heated to 65 °C. To have kinetically stable SHS particles at room temperature, we fix them. The fixing process consists of lowering the ionic strength of the solution by dilution with PBS or water. The values of the concentrations of the resulting assemblies of SGQ and *f*-SHS particles are reported based on the **iG** monomer's concentration. For time-release studies of Rhodamine B (**RhoB**), 100 µL of the SGQ solution was transferred to a new vial, and an aliquot of 10 µM **RhoB** was added. The vial was heated in a water bath to 40 °C to form SHS particles and perform an *in-situ* encapsulation of RhoB. The vial with SHS particles was left in the water bath, incubating the **RhoB** added for 5 minutes. Then, using a syringe (without tip), the **SHS@RhoB** (@ indicating that SHS particles encapsulated **RhoB**) particles was transferred to a conical reaction vial with 1.0 mL PBS in the same water bath at 40 °C. Two phases formed: a top, aqueous phase, and a bottom, colloidal phase. Due to dilution, the colloidal phase contains ***f*-SHS@RhoB** particles. A 100 μL aliquot was taken from the aqueous phase and further diluted to 3 mL to generate absorption spectra and quantify the amount of **RhoB** being released.

3.5.6. UV-Vis Kinetics measurements

Experiments were carried out in a Varian Cary 100 Bio UV-Visible Spectrophotometer. Before scanning, the instrument cell changer was calibrated as single beam. The program was set up to do baseline correction and was autozeroed three times without cell and then baseline-corrected with PBS, pH 7.4. PBS, pH 7.4 was used as the primary solvent and blank, except otherwise noted (cosolvents were 0.5% EtOH or 1% MeOH, as indicated) at room temperature.

3.5.7 Turbidimetry measurements

The transmittance experiments were measured at 500 nm using a Varian UV-visible spectrometer, Model Cary Bio-100. The heating rate was adjusted at 2.0 °C/min using the Varian's Cary temperature controller apparatus. PBS was filtered with a 0.45 μm Nylon filter using Fisherbrand 10 mm o.d. glass tubes before the experiments. Unless otherwise stated, samples were dispersed in PBS, pH 7.4. The cloud-point temperature was determined using the first derivative.

3.5.8 Dynamic Light Scattering (DLS) measurements

Experiments were carried out in a Malvern Zetasizer Nano ZS (model ZEN3600) with a 4 mW laser of 632.8 nm wavelength and a backscatter angle of 173°. The results were extracted from the Malvern Zetasizer Software version 7.10 to construct the graphs using Excel. PBS was filtered with a 0.45 μm Nylon filter using Fisherbrand 10 mm o.d. glass tubes before the experiments. Samples containing SHS or *f*-SHS particles were left tumbling in-between measurements to minimize sedimentation. Unless otherwise stated, samples were dispersed in PBS, pH 7.4.

3.5.9 Molecular modeling studies

The molecular model representations were minimized using: OPLS_2005 (MacroModel), Version Maestro 9.3.5; Schrödinger, LLC: New York, 2007, representing the water as continuum. The SGQ models presented were built upon previously published models. The SGQ was minimized by freezing the three K^+ ions and the guanine core up to the 1’ carbon of the sugar, allowing free movement of the side chains.

3.5.10. Mass Spectrometry measurements

Mass spectrometric analysis was performed using the ABSCIEX 4800 Plus MALDI TOF/TOF™ Analyzer. To spot the samples a mixture 1 μl of 5 pmol/μl sample 1 μl of 5 mg/ml gentisic acid dissolved in methanol MS was used.

3.5.11. UV-Vis Kinetics Experiments

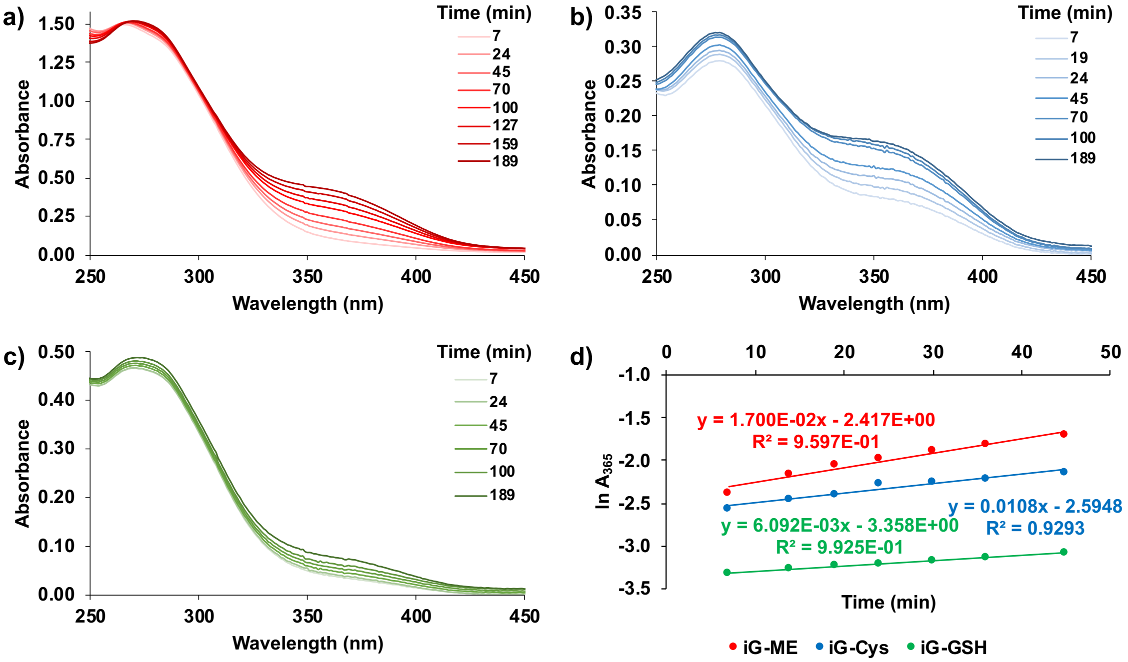

Figure S3.2. Reversibility studies of **a) iG-ME**, **b) iG-Cys**, **c) iG-GSH**. Panel **d)** shows the first order kinetic plots for **iG-ME**, **iG-Cys**, **iG-GSH**. From the slopes we get first order rate constants, and from these we get the hal*f*-lives of elimination. Starting concentration: 50 μM; Solvent: 1% MeOH in PBS, pH 7.4.

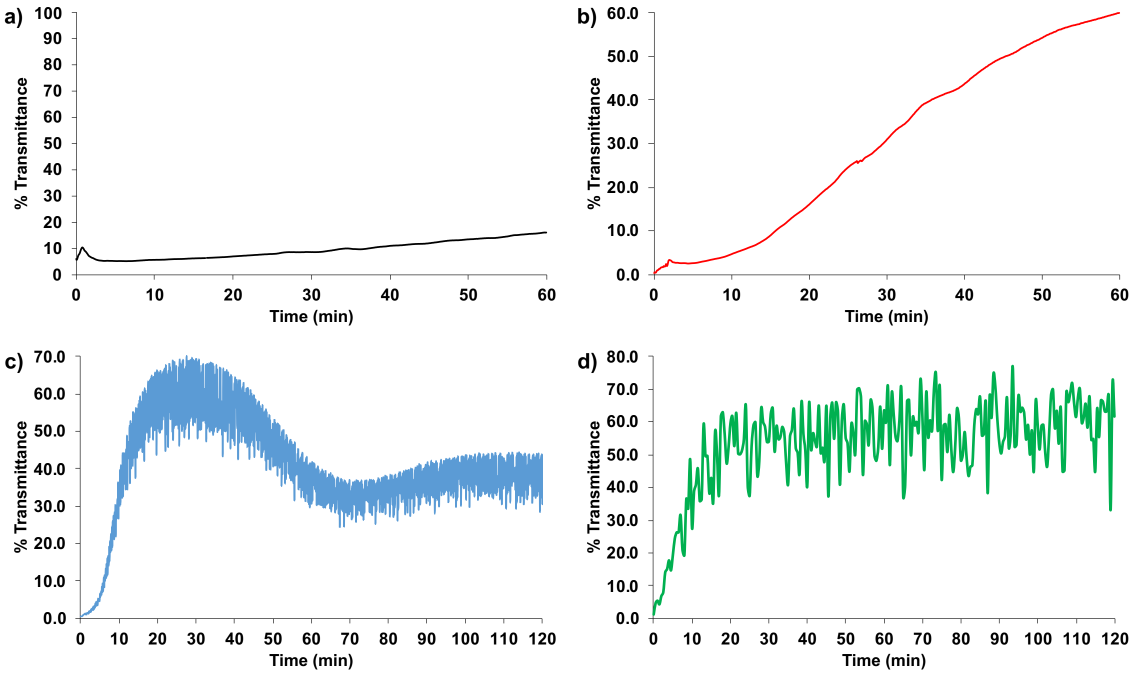

Figure S3.3. Kinetic experiments of **iG** SHS particle (5 mM, 2 M KI) at 40 °C (PBS, pH 7.4) with different thiols. a) Control (**SHS-iG**), b) **SHS-iG** + **ME** (5 mM); c) **SHS-iG** + **Cys** (5 mM); d) **SHS-iG** + **GSH** (5 mM).

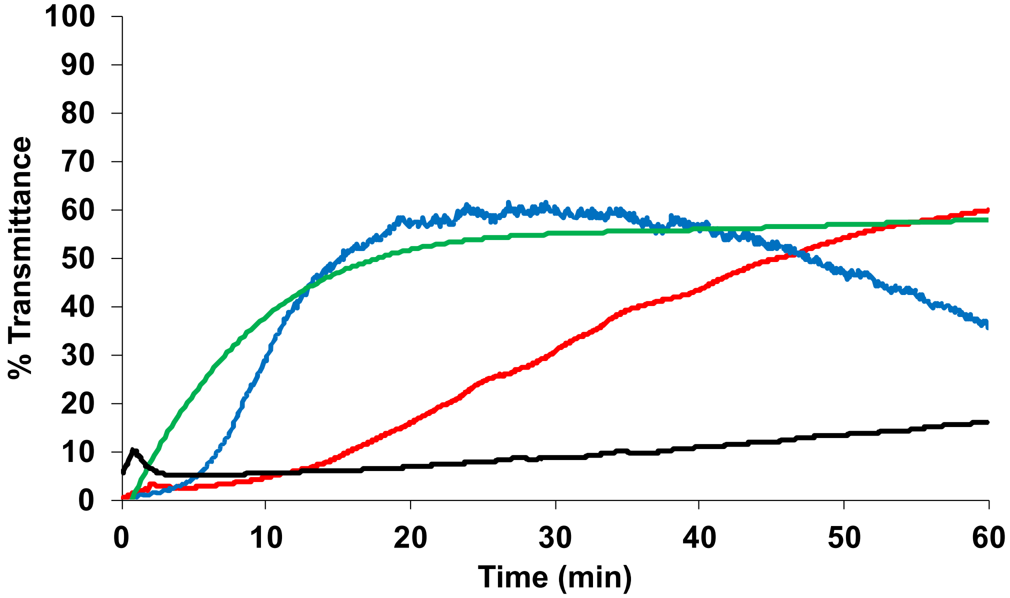

`

Figure S3.4. Curve fitting of kinetic traces for **iG** SHS (5 mM, 2 M KI) particle kinetic experiments with different thiols (40 °C, PBS, pH 7.4).

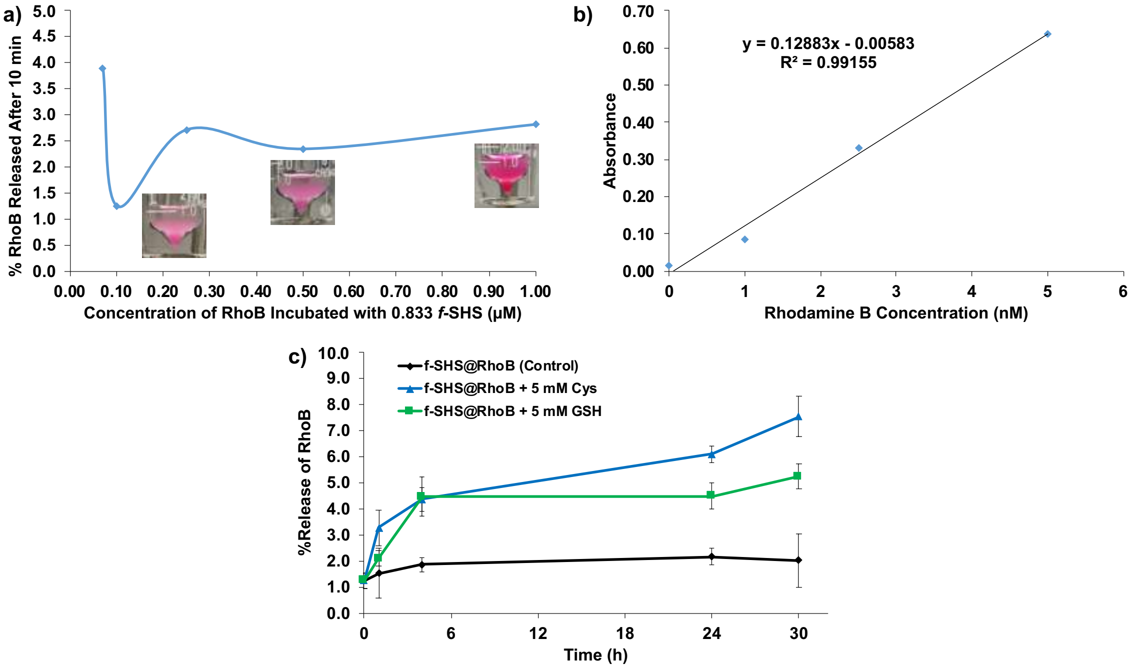

Figure S3.5. **a)** Percent RhoB released into aqueous phase after 10 minutes of in situ incubation of 0.833 ***f*-SHS-iG** (333 mM KI) particles with 0.07, 0.10, 0.50, and 1.0 μM RhoB. Inset: from left to right, ***f*-SHS-iG** particles incubated with 0.10, 0.50 μM and 1.0 μM RhoB. **b)** Calibration curve for RhoB in PBS, pH 7.4 before it reached saturation. **c)** Percent release of Rhodamine B from 0.833 *f*-SHS (333 mM KI) particles into aqueous phase in the presence of 5 mM Cys or GSH in PBS, pH 7.4.

3.6. References

(1) Kim, G.-J.; Lee, K.; Kwon, H.; Kim, H.-J. Ratiometric Fluorescence Imaging of Cellular Glutathione. *Org. Lett.* **2011**, *13* (11), 2799–2801. https://doi.org/10.1021/ol200967w.

(2) Jiang, X.; Yu, Y.; Chen, J.; Zhao, M.; Chen, H.; Song, X.; Matzuk, A. J.; Carroll, S. L.; Tan, X.; Sizovs, A.; Cheng, N.; Wang, M. C.; Wang, J. Quantitative Imaging of Glutathione in Live Cells Using a Reversible Reaction-Based Ratiometric Fluorescent Probe. *ACS Chem. Biol.* **2015**, *10* (3), 864–874. https://doi.org/10.1021/cb500986w.

(3) Nair, D. P.; Podgórski, M.; Chatani, S.; Gong, T.; Xi, W.; Fenoli, C. R.; Bowman, C. N. The Thiol-Michael Addition Click Reaction: A Powerful and Widely Used Tool in Materials Chemistry. *Chem. Mater.* **2014**, *26* (1), 724–744. https://doi.org/10.1021/cm402180t.

(4) Isokawa, M.; Kanamori, T.; Funatsu, T.; Tsunoda, M. Analytical Methods Involving Separation Techniques for Determination of Low-Molecular-Weight Biothiols in Human Plasma and Blood. *J. Chromatogr. B* **2014**, *964*, 103–115. https://doi.org/https://doi.org/10.1016/j.jchromb.2013.12.041.

(5) Tedja, R.; Soeriyadi, A. H.; Whittaker, M. R.; Lim, M.; Marquis, C.; Boyer, C.; Davis, T. P.; Amal, R. Effect of TiO2 Nanoparticle Surface Functionalization on Protein Adsorption, Cellular Uptake and Cytotoxicity: The Attachment of PEG Comb Polymers Using Catalytic Chain Transfer and Thiol–Ene Chemistry. *Polym. Chem.* **2012**, *3* (10), 2743. https://doi.org/10.1039/c2py20450a.

(6) Boutureira, O.; Bernardes, G. J. L. Advances in Chemical Protein Modification. *Chem. Rev.* **2015**, *115* (5), 2174–2195. https://doi.org/10.1021/cr500399p.

(7) McKay, C. S.; Finn, M. G. Click Chemistry in Complex Mixtures: Bioorthogonal Bioconjugation. *Chem. Biol.* **2014**, *21* (9), 1075–1101. https://doi.org/http://dx.doi.org/10.1016/j.chembiol.2014.09.002.

(8) Hoyle, C. E.; Lowe, A. B.; Bowman, C. N. Thiol-Click Chemistry: A Multifaceted Toolbox for Small Molecule and Polymer Synthesis. *Chem. Soc. Rev.* **2010**, *39* (4), 1355–1387. https://doi.org/10.1039/B901979K.

(9) Krenske, E. H.; Petter, R. C.; Houk, K. N. Kinetics and Thermodynamics of Reversible Thiol Additions to Mono- and Diactivated Michael Acceptors: Implications for the Design of Drugs That Bind Covalently to Cysteines. *J. Org. Chem.* **2016**, *81* (23), 11726–11733. https://doi.org/10.1021/acs.joc.6b02188.

(10) Chan, J. W.; Hoyle, C. E.; Lowe, A. B.; Bowman, M. Nucleophile-Initiated Thiol-Michael Reactions: Effect of Organocatalyst, Thiol, and Ene. *Macromolecules* **2010**, *43* (15), 6381–6388. https://doi.org/10.1021/ma101069c.

(11) Negrón, L. M.; Díaz, T. L.; Ortiz-Quiles, E. O.; Dieppa-Matos, D.; Madera-Soto, B.; Rivera, J. M. Organic Nanoflowers from a Wide Variety of Molecules Templated by a Hierarchical Supramolecular Scaffold. *Langmuir* **2016**, 2283–2290. https://doi.org/10.1021/acs.langmuir.5b03946.

(12) Betancourt, J. E.; Rivera, J. M. Nonpolymeric Thermosensitive Supramolecules. *J. Am. Chem. Soc.* **2009**, *131* (46), 16666–16668. https://doi.org/10.1021/ja9070927.

(13) Betancourt, J. E.; Subramani, C.; Serrano-Velez, J. L.; Rosa-Molinar, E.; Rotello, V. M.; Rivera, J. M. Drug Encapsulation within Self-Assembled Microglobules Formed by Thermoresponsive Supramolecules. *Chem. Commun.* **2010**, *46* (45), 8537. https://doi.org/10.1039/c0cc04063k.

(14) Betancourt, J. E.; Rivera, J. M. Tuning Thermoresponsive Supramolecular G-Quadruplexes. *Langmuir* **2015**, *31* (7), 2095–2103. https://doi.org/10.1021/la504446k.

(15) Santos, S.; Ramírez, M.; Miranda, E.; Reyes, N.; Martínez, O.; Acosta-Santiago, M.; Rivera, J.; Otero, M. Enhancement of Immune Responses by Guanosine-Based Particles in DNA Plasmid Formulations against Infectious Diseases. *J. Immunol. Res.* **2019**, *2019*, 15. https://doi.org/10.1155/2019/3409371.

(16) Gubala, V.; Betancourt, J. E.; Rivera, J. M. Expanding the Hoogsteen Edge of 2‘-Deoxyguanosine: Consequences for G-Quadruplex Formation. *Org. Lett.* **2004**, *6* (25), 4735–4738. https://doi.org/10.1021/ol048013v.

(17) Kyte, J.; Doolittle, R. F. A Simple Method for Displaying the Hydropathic Character of a Protein. *J. Mol. Biol.* **1982**, *157* (1), 105–132. https://doi.org/https://doi.org/10.1016/0022-2836(82)90515-0.

(18) Amslinger, S.; Al-Rifai, N.; Winter, K.; Wormann, K.; Scholz, R.; Baumeister, P.; Wild, M. Reactivity Assessment of Chalcones by a Kinetic Thiol Assay. *Org. Biomol. Chem.* **2013**, *11* (4), 549–554. https://doi.org/10.1039/C2OB27163J.

(19) Chen, J.; Jiang, X.; Carroll, S. L.; Huang, J.; Wang, J. Theoretical and Experimental Investigation of Thermodynamics and Kinetics of Thiol-Michael Addition Reactions: A Case Study of Reversible Fluorescent Probes for Glutathione Imaging in Single Cells. *Org. Lett.* **2015**, *17* (24), 5978–5981. https://doi.org/10.1021/acs.orglett.5b02910.

(20) Negrón, L. M. Synthesis and Characterization of Thermo/PH-Responsive Supramolecular G-Quadruplexes for the Construction of Supramolecular Hacky Sacks for Biorelevant Applications, University of Puerto Rico, Rio Piedras Campus, 2014.

(21) Rivera, J. M.; Negrón, L. M. Supramolecular Hacky Sacks (SHS), Method of Synthesis and Applications Thereof. 10106572, 2018.

(22) Rivera-Sánchez, M. del C.; García-Arriaga, M.; Hobley, G.; Morales-de-Echegaray, A. V; Rivera, J. M. Small-Molecule-Based Self-Assembled Ligands for G-Quadruplex DNA Surface Recognition. *ACS Omega* **2017**, *2* (10), 6619–6627. https://doi.org/10.1021/acsomega.7b01255.

(23) García-Arriaga, M.; Hobley, G.; Rivera, J. M. Structural Studies of Supramolecular G-Quadruplexes Formed from 8-Aryl-2′-Deoxyguanosine Derivatives. *J. Org. Chem.* **2016**, *81* (14), 6026–6035. https://doi.org/10.1021/acs.joc.6b01113.

(24) Maestro. version 9. Scrödinger LLC: New York 2007.

(25) MacroModel. version 8. Schrödinger, LLC: New York 2007.

(26) Dalgakiran, E.; Tatlipinar, H. The Role of Hydrophobic Hydration in the LCST Behaviour of POEGMA300 by All-Atom Molecular Dynamics Simulations. *Phys. Chem. Chem. Phys.* **2018**, *20* (22), 15389–15399. https://doi.org/10.1039/C8CP02026D.

(27) Kurzbach, D.; Hassouneh, W.; McDaniel, J. R.; Jaumann, E. A.; Chilkoti, A.; Hinderberger, D. Hydration Layer Coupling and Cooperativity in Phase Behavior of Stimulus Responsive Peptide Polymers. *J. Am. Chem. Soc.* **2013**, *135* (30), 11299–11308. https://doi.org/10.1021/ja4047872.

(28) Bizmark, N.; Ioannidis, M. A. Effects of Ionic Strength on the Colloidal Stability and Interfacial Assembly of Hydrophobic Ethyl Cellulose Nanoparticles. *Langmuir* **2015**, *31* (34), 9282–9289. https://doi.org/10.1021/acs.langmuir.5b01857.

(29) Schafer, F. Q.; Buettner, G. R. Redox Environment of the Cell as Viewed through the Redox State of the Glutathione Disulfide/Glutathione Couple. *Free Radic. Biol. Med.* **2001**, *30* (11), 1191–1212. https://doi.org/https://doi.org/10.1016/S0891-5849(01)00480-4.

Chapter 4. Effects of Thiazolidine Formation on Guanine Based Supramolecular Structures

4.1. Abstract

One way to make a biothiol responsive materials is through the formation of thiazolidines. Materials such as a particles can use the reaction of formyl moieties with thiols such as cysteine to form thiazolidines. Here we show the development of formyl containing particles termed Supramolecular Hacky Sacks (SHS). Formyl-containing SHS particles were reacted with varying amounts of cysteine and the process was monitored via turbidity experiments. These showed cysteine concentration-dependent kinetics as 10 equiv of cystine lead to a 50% transmittance change by 80 minutes. Kinetics studies were followed by studying the SHS particles' constituents supramolecular G-quadruplex (SGQ) structures. NMR studies reveal that thiazolidine formation leads to the disassembly of the SGQ structures. Molecular modeling studies suggest that steric and repulsive electrostatic interactions of the anionic carboxylates destabilize the SGQ structures, which in turn leads to its disassembly. Successful encapsulation of rhodamine B in the SHS particles enabled the study of the release kinetics, were the addition of cysteine enhanced the release rhodamine B. This phenomenon is consistent with thiazolidine formation increasing the disassembly of the SHS particles and its constituent SGQs. This strategy shows some similarities to the one described in Chapter 3 where a conjugate addition of cysteine and other biothiols also lead to enhanced release of the corresponding SHS particles.

However, given the difference in the kinetics of the thiazolidine formation, the current strategy should find applications that are complementary to that strategy.

4.2. Introduction

Biothiols as L-cysteine (Cys), homocysteine, or glutathione (GSH) play a significant role in biological processes.[1] Biothiols' primary function is their involvement in various RedOx reactions. Specifically, in the immune system, biothiols play a vital role in the inflammation process.[1] This interest in biothiols arises because they are being discovered to play roles in different medical afflictions.[2] Biothiols play roles in HIV, cancer, Alzheimer's, among other medical conditions.[2–4] Scientists decided to explore this field as biothiols are seen in microenvironments like Cys concentrations of 30 - 500 μM or GSH in concentrations of 1 – 5 mM in cells.[5] Researchers have developed an interest in these microenvironments as a way to design thiol-responsive particles. These particles are to be used for drug or gene delivery, tissue engineering, imaging, or theragnostic, among others.[6] Thiol-responsive materials have been developed to detect cysteine, homocysteine, and glutathione.[7,8] Biothiol responsive materials can use disulfide bonds, chalcones, or alkynes as chemoselective reactive moieties.[6,9–12]

Cysteine is the only one of the biothiols involved in the construction of proteins, peptides (as GSH) construction, enzymes active sites, and cofactors.[13] It is highly involved in cellular processes such as immune system regulation, therefore, in-situ detection of this molecule is an attractive research endeavour.[6] Cysteine responsive systems can be developed by controlling their reactivity, reversibility, and accessibility of the reactive moieties.[14,15] One way to obtain a cysteine responsive particle is through the formation of thiazolidines in the presence of formyl groups (Scheme 4.1).[6] Cysteine reaction with formyl groups leads to a thiazolidine-4-carboxylate moiety formation (Scheme 4.1). The reaction occurs via a pH-dependent mechanism of intermolecular addition followed by cyclization.[16,17] This approach has been used for antibody solid-phase extraction techniques, antibody-drug conjugation, and sensing strategies for cysteine and homocysteine detection.[18–22] The formation of thiazolidines is also widely used in polymer chemistry for hydrogel formulations and 3D cell culture scaffolds.[23–26]

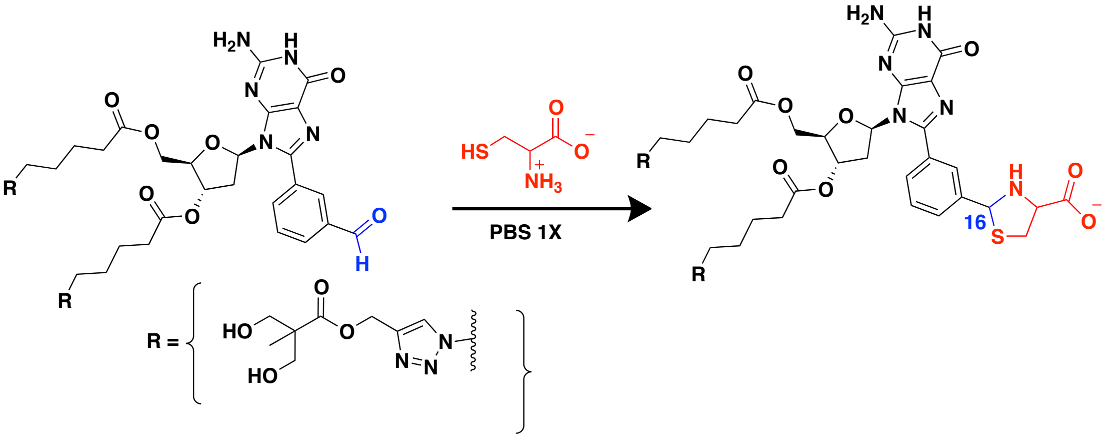

Scheme 4.1. Reaction of the formyl moiety (blue) in **fG** with Cys (red) in PBS, pH 7.4 (pH 7.5) leads to the formation of the thiazolidine-containing G-derivative (**tG**).

As we work on the fine-tuning of particles termed Supramolecular Hacky Sacks (SHS) particles, we produced a formyl containing SHS (**SHS-fG**) particles. SHS are the product of thermal responsive supramolecular guanine quadruplexes (SGQ) via lower critical solution temperature (LCST). The LCST of the formyl containing SGQ (**SGQ-fG**) is 10 °C. The SGQ itself is the self-assembly via a salting-in process of G-derivative **fG** seen in Scheme 4.1.

In this research we aim to magnify the utility of SHS particles via the expansion of responsive properties. Producing **fG** has allowed the expansion of biothiol responsive SHS particles in addition to its thermal responsive properties. Here we focus on how the formation of thiazolidine affects the different supramolecular structures. To study the SHS particles, we started looking at how turbidity is affected by varying the amount of cysteine. Turbidity studies accompanied by dynamic light scattering (DLS) experiments to the mechanism of the reaction. For a molecular understanding of the thiazolidine formation, we turned to NMR and molecular modeling of the **SGQ-fG**. We then decided to see how **SHS-fG** can encapsulate and release Rhodamine B (**RhoB**) by forming the thiazolidine. We characterized the **SHS-fG** encapsulating **RhoB** via DLS and laser scanning confocal microscopy (LSCM). The release was followed by absorbance studies and LSCM also.

4.3. Results and Discussion

4.3.1. SHS particles kinetics and mechanism.

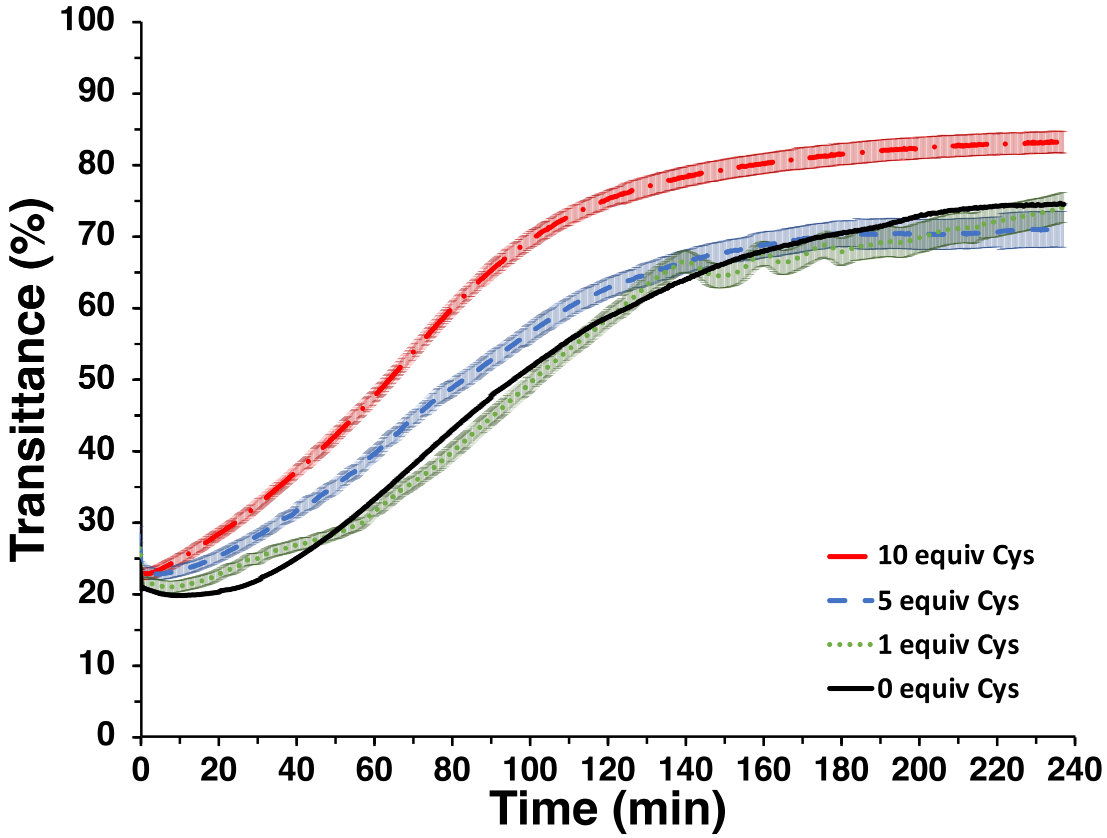

Figure 4.1. Kinetic experiments measured using **SHS-fG** 1 mM, 100 mM of KSCN in PBS, pH 7.4. The **SHS-fG** was stabilized at 37 °C before varying equiv of Cys was added before the measurement started.

To understand how the **SHS-fG** is affected by the presence of Cys we study the formed by the particle itself. As the Formyl based SGQ's LCST is below 37 °C, we explore this reaction in said bio-relevant temperature. These studies were made **SHS-fG** with 1, 5, and 10 equiv of Cys (Figure 4.1). Here we can observe that the transmittance for all samples increases, yet we can see different trends. We expected the rise of transmittance for the sample with no cysteine. The systems' upper critical solution temperature (As we previously showed in Chapter 2) transitions starts around 40 °C and sedimentation is possible due to cell size.

DLS data shows a 60 % decrease in the SHS particle population at 90 minutes (Table 4.1). Said population kept the same particle average size.

Table 4.1. Effects of thiazolidine formation on the dissolution kinetics, size and abundance of the **SHS-fG** particles.

Time	[Cys] (equiv)	T_{50} (min)	D_H (nm)*	DCR (kcps)*
0 min	0	NA	843	7162
90 min	0	125	843	2854
	1	123	–	–
	5	110	570	2192
	10	80	728	1807

* DLS experiments were performed 90 min after adding Cys. T_{50} = time required to reach 50% transmittance. D_H: hydrodynamic diameter. DCR: Derived count rate

The transmittance of **SHS-fG** particles with 1 and 5 equiv of Cys are very similar to the one with 0 equiv after 140 minutes. To see the difference between samples we look at the time it takes for each sample to change 50% of its original transmittance to the PBS, pH 7.4 blank with 100 mM of KSCN (98% T). Samples with 0 and 1 equiv of Cys reach 50% change of transmittance at 125 and 123 minutes. The difference is dismissible when taking into consideration the measurement's error. The thiazolidine formation using 1 equiv of Cys is not fast enough to overtake previously explained phenomena. For this reason, samples with 1 equiv of Cys were not further studied. **SHS-fG** particles reaction with 5 or 10 equiv of Cys showed a 50% change at 110 and 80 minutes. DLS data (Table 4.1) here also indicates a population decrease of 70% and 75%, at 90 minutes.

Because we study the particle, transmittance does not give us concentration or molecular information of the reaction taking place. As the measured population of SHS particles via DLS and transmittance provides us with an understanding of which phenomena take the responsive particle's driving force. With experiments done with 5 and 10 equiv of Cys, we can understand that SHS particle integrity is affected further than the **SHS**-**fG** upper critical solution temperature (UCST) properties. **SHS**-**fG** full thermal properties characterization can be found on chapter 2. The thiazolidine formation is a second-order reaction as it is a two-step second-order reaction with a rate-limiting intermediate formation step.[16] It is reasonable to say that a higher concentration of thiol leads to a higher reaction rate. Turbidity and DLS experiments of **SHS-fG** particles with 5 and 10 equiv of Cys prove that thiazolidine formation affects the particle.

4.3.2. SGQ thiazolidine reaction

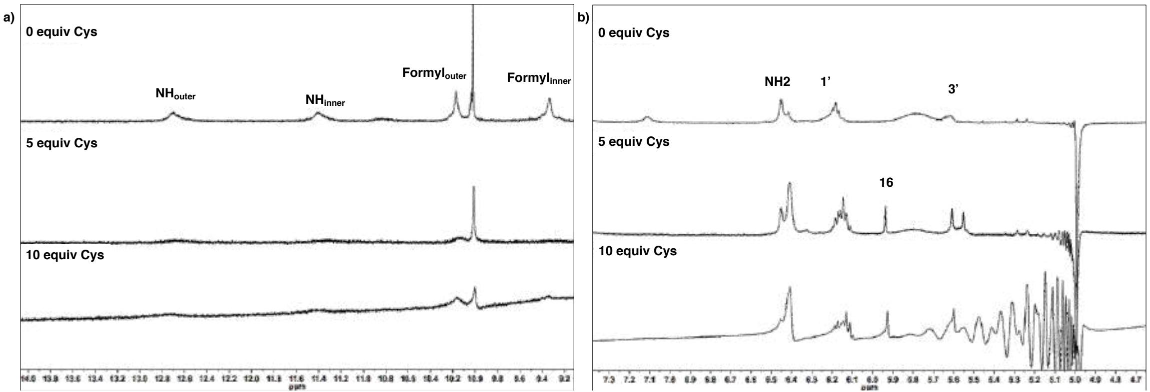

Figure 4.2. Partial ^{1}H NMR (500 MHz) of **SGQ-fG** with varying equiv of Cys after 90 min. Chemical shift windows correspond to (a) 9.2 – 10 ppm, and (b) 4.7 - 7.3 ppm. Relative magnifications for 0, 5, and 10 equiv are 17X, 25X, and 55X, respectively. Conditions: **fG** (1 mM) in PBS, pH 7.4 with 2% D_2O at 5 °C done on a 1 mM, 100 mM of KSCN.

We look into the molecular information given by water suppression ^{1}H NMR (Figure 4.2). For that, we look into how the reaction of the **SGQ-fG** in the presence of the Cys. We focus on the N1H SGQ signature peaks attesting to the tetrad hydrogen bonding (11.45 and 12.70 ppm), and formyl peaks (at around 10.10). Because the SGQ core has a D_4 symmetry, all peaks show doubled and overlapping.[27] This symmetry comes from the inner and outer tetrads having two distinct chemical environments. The outer tetrads have an exposed face to the solvents and another into the inner tetrad. In contrast, the inner tetrads maintain a tetrad-tetrad interaction on each face.[27,28] Peaks with higher chemical shifts correspond to the exposed protons to the solvent.[28]

Formyl signals decreased significantly when using 5 equiv of Cys when compared to samples with no Cys. Both formyls show the same behavior at 10 equiv with this information, we can understand that solvent-exposed formyl groups are prone to react first rather than later as expected. As we look at the NMR of Figure 4.2a we can also identify that 5 equiv of Cys affect the N-H signals. Both N-H signals have decreased significantly at 5 and 10 equiv of Cys Figure 4.2a. The decrease of said signals means that SGQ disassembly is prone to the thiazolidine formation. As for the NMR shifts around 5.9 ppm we can see the appearance of a singlet signal Figure 4.2b. This signal can be identified as the C16 proton (identified in Scheme 4.1).[22] This signal can be used to confirm the thiazolidine formation. Two main behaviors could explain that we see only one proton from C16. The arise of this peak could signify that only one type of formyl is reaction (inner or outer). Yet by following the peaks in Figure 4.2a we can understand that both formyls are reacting and disassembly is probable.

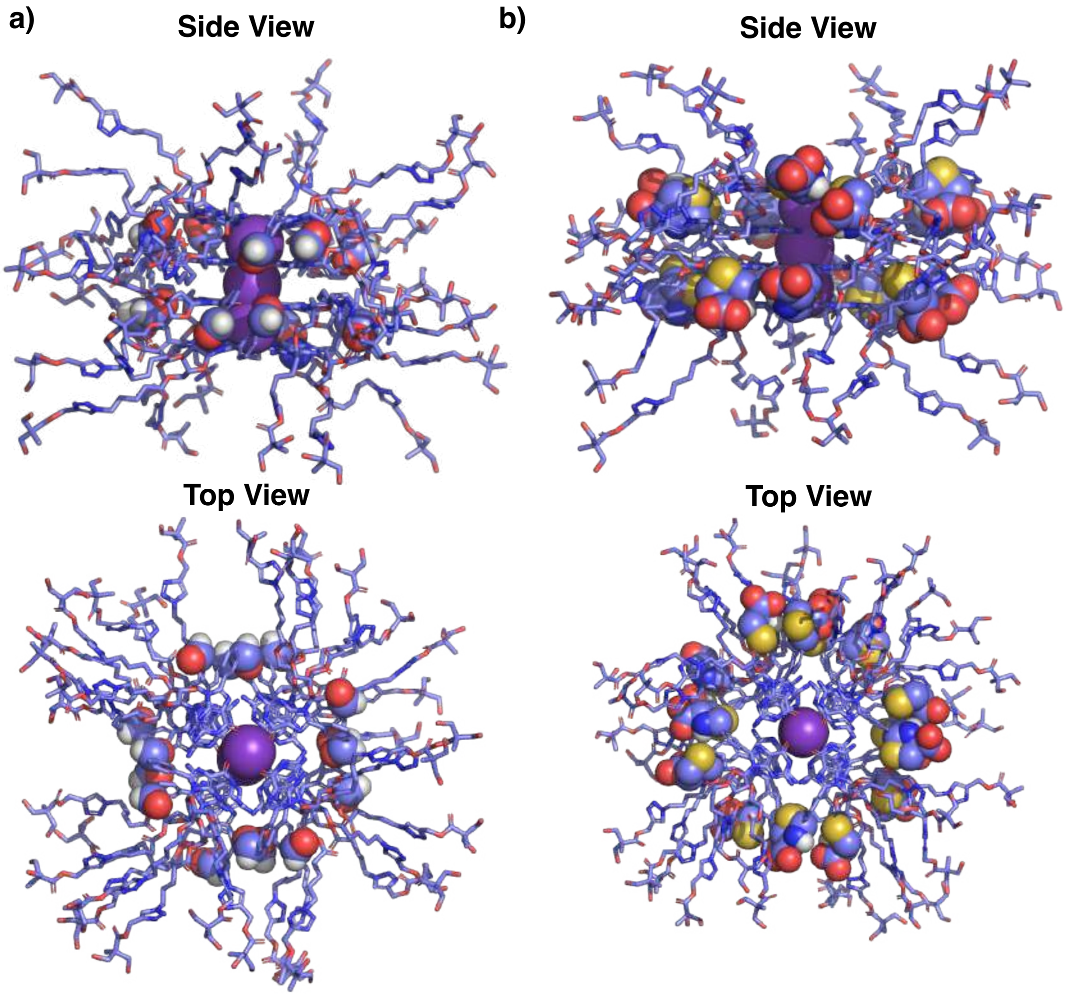

Figure 4.3. Molecular models of (a) **SGQ-fG** and (b) **SGQ-tG**. Formyl and thiazolidine moieties are represented as space-filling spheres. The molecular model representations were minimized using: OPLS_2005 (MacroModel), Version Maestro 9.3.5; Schrödinger, LLC: New York, 2007, representing the water as continuum.

As we look at the molecular models, we can understand what is seen via NMR in more depth. Figure 4.3a shows that formyl moiety serves as an additional H-bond acceptor for the tetrad H-bonding network in **SGQ-fG**. As previously mentioned, this acts as a stabilizer for the supramolecular system core.[27,28] For the SGQ including the thiazolidine moiety (**SGQ-tG**, Figure 4.3b), random H-bonding was seen by the introduced amine and some sulfides with neighboring tetrads.

Although these introduced H-bonds can assist random aggregates, they are not sufficient to their counteract the resulting repulsive interactions. The introduced thiazolidine adds major electrostatic repulsion to the arranged structure. The resulting cyclic system adds neighboring sulfides, detrimental to the SGQ core. The thiazolidine formation with cysteine also results in an array of carboxylate groups close to the SGQ core. These groups mount to a higher repulsive electrostatic interaction on the area shown in Figure 4.3b. These interactions prove detrimental to said core and explain the detriment of the SGQ shown on the NMR studies. By studying the implication of the thiazolidine formation using cysteine, we can understand the particle's behaviors. As more thiazolidine are formed in the SGQ, the SHS particle's building block, it is confirmed that the particle's loss of integrity is based on the SHS participating in this reaction.

4.3.3. Encapsulation and release of cargo

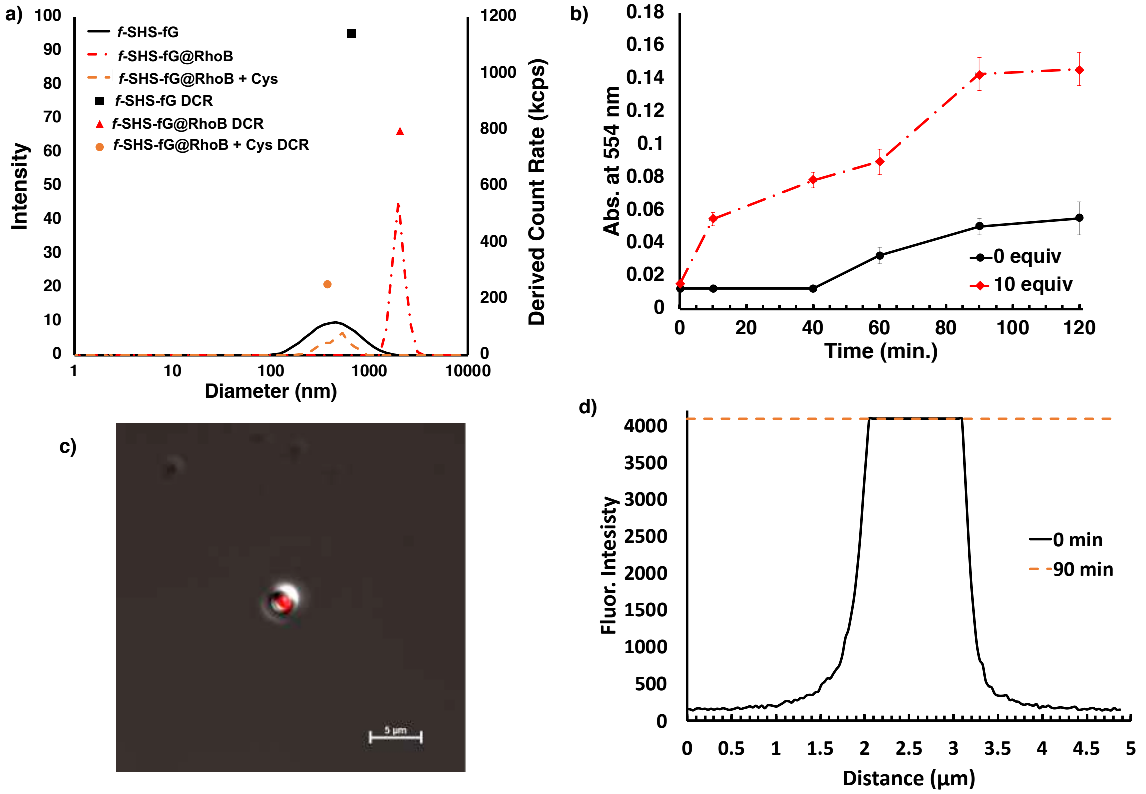

Figure 4.4. Structural features of ***f*-SHS-fG** and ***f*-SHS-fG@RhoB** as before and after Cys addition and **RhoB** release profile as a function of Cys concentration. (a) Distribution of hydrodynamic diameterrs and relative abundance of ***f*-SHS-fG**, ***f*-SHS-fG@RhoB** particles and ***f*-SHS-fG@RhoB** + 10 equiv of Cys after 90 minutes. (b) Release profile of **RhoB** from ***f*-SHS-fG@RhoB** after addition of 0 and 10 equiv of Cys. (c) LSCM image and (d) fluorescence intensity line scan for of a **f-SHS-fG@RhoB** particle at 0 min and 90 mins after the addition of Cys (10 equiv) (scale bar = 5 µm). Conditions: All samples contained 75 µM of SHS particles dissolved in PBS, pH 7.4 with KSCN (7.5 mM); samples of ***f*-SHS-fG@RhoB** have contained 1 µM of **RhoB**; all reactions were performed at 37 °C.

As previously mentioned, SHS particles serve as small molecule encapsulator.[29] Understanding that the thiazolidine formation disassembles the **SHS-fG** particles, we conducted encapsulation and release studies. The encapsulation process itself follows as an in-situ behavior. The desired concentration of cargo is added to the SGQ solution to form SHS particles. Then we decided to use **RhoB** as cargo using ‘fixed’ SHS (*f*-SHS) particles. The fixing process provides stable SHS particles where reversibility to the SGQ below LCST or UCST takes place. We achieved fixing by lowering the ionic strength of the solution after the SHS particles are formed. We used the *f*-SHS at 75 µM of SHS, and 7.5 mM of KSCN (***f*-SHS-fG** particles) and encapsulating a final concentration of 1 µM of **RhoB** (***f*-SHS-fG@RhoB**) particle.

We followed the encapsulation process via DLS and LSCM (Figure 4.4a and c). Both concur that the encapsulation of RhoB increases the diameter of the *f*-SHS particles to 2 µm (Figure 4.4a). By DLS we can see that the SHS particle population decreases. Yet cargo is seen in the LSCM image (Figure 4.4c). Analysis of said image shows the encapsulated payload identified in red, and SHS particles as the globular structure. We took fluorescence intensity of the ***f*-SHS-fG@RhoB** particles via LSCM imaging (Figure 4.4d). We can see that fluorescence intensity increases as we move into the center of the ***f*-SHS-fG@RhoB** particle over the detection threshold. The intensity decreases as we measure said fluorescence moving away from the particle’s center. DLS data shows that the process of encapsulation takes a higher concentration of SGQ to contain the cargo. Ergo the encapsulation produces fewer SHS particles. Said SHS particles encapsulates the desired payload effectively. Confocal image data confirms the **RhoB** encapsulated within the SHS particles and still being able to fluoresce.

From the encapsulation, we turn into the release of RhoB. We added 10 equiv of Cys to the prepared ***f*-SHS-fG@RhoB** particles, or no Cys. We used 10 equiv of Cys as it is effective by 90 minutes comparably to other Cys concentrations. As we follow the absorbance at 554 nm through time (Figure 4.4b), we can observe an increase of **RhoB** in each sample's supernatant. A higher absorbance for the samples with Cys was consistent compare to the ones without Cys. The absorbance reached stabilization after 90 minutes. By 120 min a 0.6 μM of **RhoB** was released. We detected few ***f*-SHS-fG@RhoB** particles via DLS (Figure 4.4a), and none were found on the confocal studies after 90 min. The LSCM confocal studies (Figure 4.4d) also confirms the release of RhoB after 90 minutes as no particles were found, yet RhoB was detected. Fluorescence intensity measurement after 90 min also is over the detection threshold. The low derived count rate of 252 kcps seen by DLS of ***f*-SHS-fG@RhoB** particles after 90 min reacting 10 equiv of Cys (Figure 4.4a) explains no particle seen on the confocal studies at this stage.

4.4. Conclusion

As we focused our studies on how Cys affected the SHS particle, we observed different phenomena. The kinetic studies revealed that the second order reaction of thiazolidine formation is competing with the particle's UCST. But, the UCST of **SHS-fG** particle being at 42 °C, by 37 °C the process has begun (see Chapter 2). Therefore, it is expected that the transmittance will be affected even when no Cys is present. Yet we were able to show that with 5 equiv of Cys and over, the change in transmittance at 37 °C can be modulated. The 50% transmittance change demonstrated this modulation. The use 10 equiv of Cys showed the fastest 50% change in transmittance in around 80 minutes. This consolidates the generation of a SHS particle responsive to cysteine and thermal changes in the same formulation.

Further molecular studies confirmed the cause of the particle's building block SGQ was reacting with Cys. The formation of the thiazolidine forced SGQ disassembly. The SGQ disassembly explained the particle size and population decrease. We saw fewer SHS particles as the SGQ disassembled. As we have previously published that SHS particles encapsulate cargo, we decided to use ***f*-SHS-fG** particles to encapsulate **RhoB**.[29] Characterization via DLS showed an increase in size as expected. LSCM showed the particle encapsulated dye. We decided to use 10 eq of Cys to release encapsulated RhoB. We followed these experiments by UV-Vis absorbance and LSCM studies. Release studies showed a 60% release of the dye by 120 min.

These studies confirm the addition of a biothiol responsive SHS particles through a new mechanism. As previously mentioned, the use of thiazolidine formation is primarily done to construct polymeric scaffolds or recombination of drugs.[18,25] To our knowledge this is the first time that the formation of thiazolidine moiety is directly used to promote the delivery of encapsulated cargo of a colloidal particle. With this study, we have introduced a thermal and thiol responsive nanoparticle to the field. By introducing a dual responsive SHS particle, we can further explore and fine-tune the particle for future studies of cysteine or homocysteine detection, and drug or pDNA delivery.

4.5. Experimental Procedures

4.5.1. Reagents

The L-Cysteine was purchased from Sigma-Aldrich. Silica gel 60, 0.04-0.063 mm and TLC plates with EMD silica gel 60 F254 glass-backed from Sorbent Technologies. Visualization in TLC plated was done using UV light and iodine. PBS 1x was purchased from Fisher Scientific. All other reagents were also from commercial sources and used without further purification.

4.5.2. 8ArG Synthesis

fG followed synthesis was published in 2013.[30,31] For the formyl derivative Bromination reaction and Suzuki-Miyaura coupling were done as previously reported with the corresponding boronic acid.[32] The following steps of esterification, nucleophilic substitution 2, and click reaction followed as previously published.[30]

4.5.3. Protocols for the preparation of SGQ solutions

The KSCN was added from a highly concentrated solution in distilled water for the desired concentration for a final volume of 1 mL. Then the water evaporated in an oven for 60 °C for over 12 hr. Then, the G-derivatives was added from a MeOH for a final concentration of 1 mM in 1 mL to the KSCN. Then the MeOH was evaporated in an oven at 35 °C for 12 hr. Then 1 mL of PBS, pH 7.4 was added and let for over 12 hr. at 2 °C for the SGQ to stabilize. This procedure was done to have exact amounts of the desired compound.

4.5.4. NMR Studies

NMR studies were done using a Bruker Ascend Aeon 700 or 500 equipped with a CPP BBO 500S1 BB-H&*F*-D-05 Z probe. Samples of the G-derivatives were measured at a concentration of 5 mM using DMSO-d_6 at a temperature of 298 K, unless otherwise stated. Studies of SGQs were performed using solutions of 1 mM of G-derivatives in PBS with KSCN (100 mM), pH 7.4 with 2% of H_2O-D_2O (9:1) at a temperature of 278 K, unless otherwise stated. Sodium 3-(trimethylsilyl)propionate-2,2,3,3-d_4 (Aldrich) was used as the internal standard for the NMR experiments performed in H_2O-D_2O (9:1). SGQs were studied using excitation sculpting water suppression experiments.

4.5.5. Molecular Models

The molecular model representations were minimized using: OPLS_2005 (MacroModel), Version Maestro 9.3.5; Schrödinger, LLC: New York, 2007, representing water as a continuum solvent.[33,34] The SGQ models presented were minimized by freezing the three potassium cations and the guanine core up to the C1' of the sugar, allowing free movement of the ester chains.

4.5.6. Turbidity Experiments

All UV-Vis experiments were done in a Cary temperature controller UV-Vis spectrophotometer Varian instrument (Cary Bio-100) at the UPR's MSRC. For the kinetics experiments the samples were inserted after the temperature stabilized at 10 minutes of the instrument stabilized at 37 °C. Then the sample was left stabilizing at 37 °C for five minutes. After said 5 minutes L-cysteine was added for sample to have final equiv of 0, 1, 5, and 10. Then sample was left funning for 4 hours. Turbidity experiments ran in a ramp of 3 °C to 75 °C at average time of 1 second with 0.3 minutes of cycle time. Measured wavelength at 650 nm.

4.5.7. Release kinetics experiments

A calibration curve was constructed from measurements of 750 µM of L-cysteine and 7.5 mM of KSCN in PBS, pH 7.4 with varying concentrations of rhodamine-b. Encapsulation was done by transferring Rhodamine-B into an SGQ containing vial at 5 °C. Temperature then was increasing at 37 °C for 2-3 minutes for the formation of the SHS particles. Later an aliquot of said soliton was transferred to a conical interior bottoms vial with PBS, pH 7.4 at 37 °C for a final concentration of 75 µM of the SHS particles and 1 µM of rhodamine-b. After 5 minutes, 10 eq (750 µM) of L-cysteine were added. Solutions were prepared for each time-point of absorbance taken at 554 nm.

4.5.8. SHS particle characterization

We measured the hydrodynamic diameter of SHS particles at varying temperatures. A Malvern Zetasizer Nano Zs (ZEN3600) with a low-volume quartz batch cuvette (ZEN2112) were used.

4.5.9. Confocal microscopy experiments

Confocal microscopy images were done Nikon Eclipse Ti-E Inverted microscope of the Neuroimaging and Electrophysiology Facility (NIEF) at the UPR MSRC (NIH award number P20GM103642). The camera type used for all SHS particle samples was Nikon A1plus. Laser wavelength at 561.7 nm with 0.8 power. Using a Plan Apo λ 60X with oil optic.

4.6. Supporting Information

4.6.1. Dynamic light scattering data.

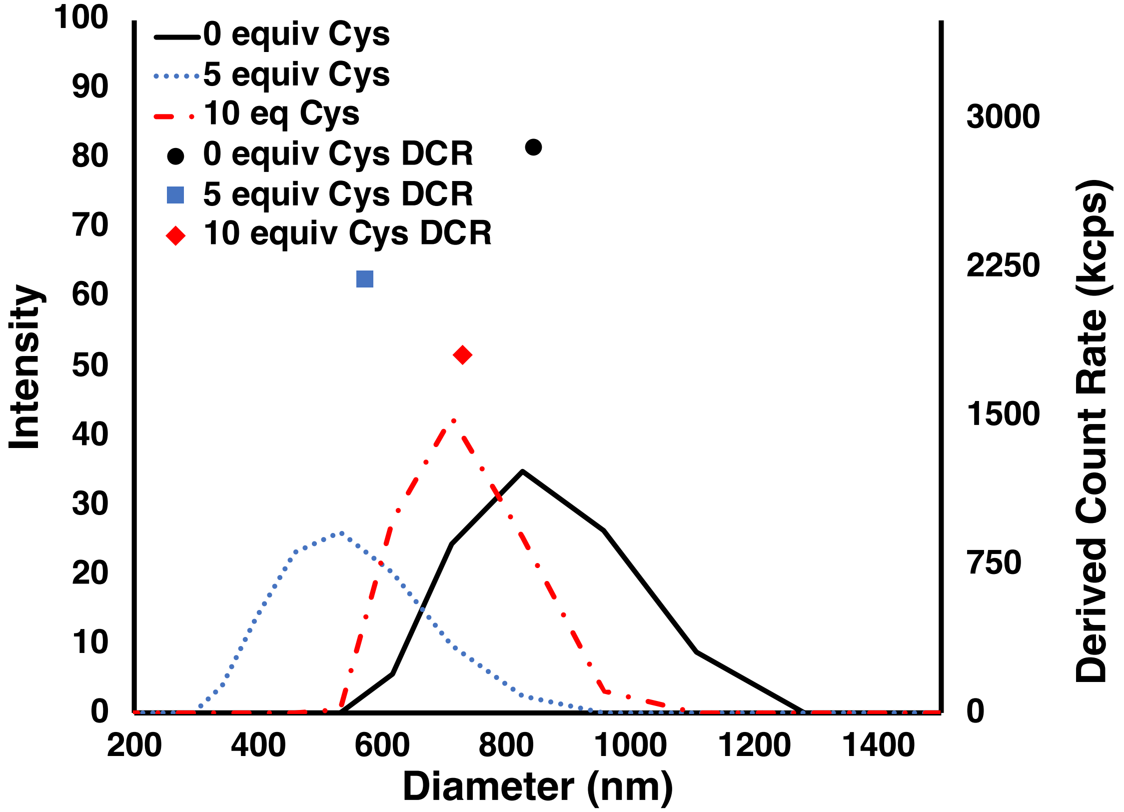

Figure S4.1. Hydrodynamic ratio and derived count rate of 1mM of G-derivatives with 100 mM of KSCN in PBS, pH 7.4 at 37 °C after 90 minutes of varying equiv of Cys.

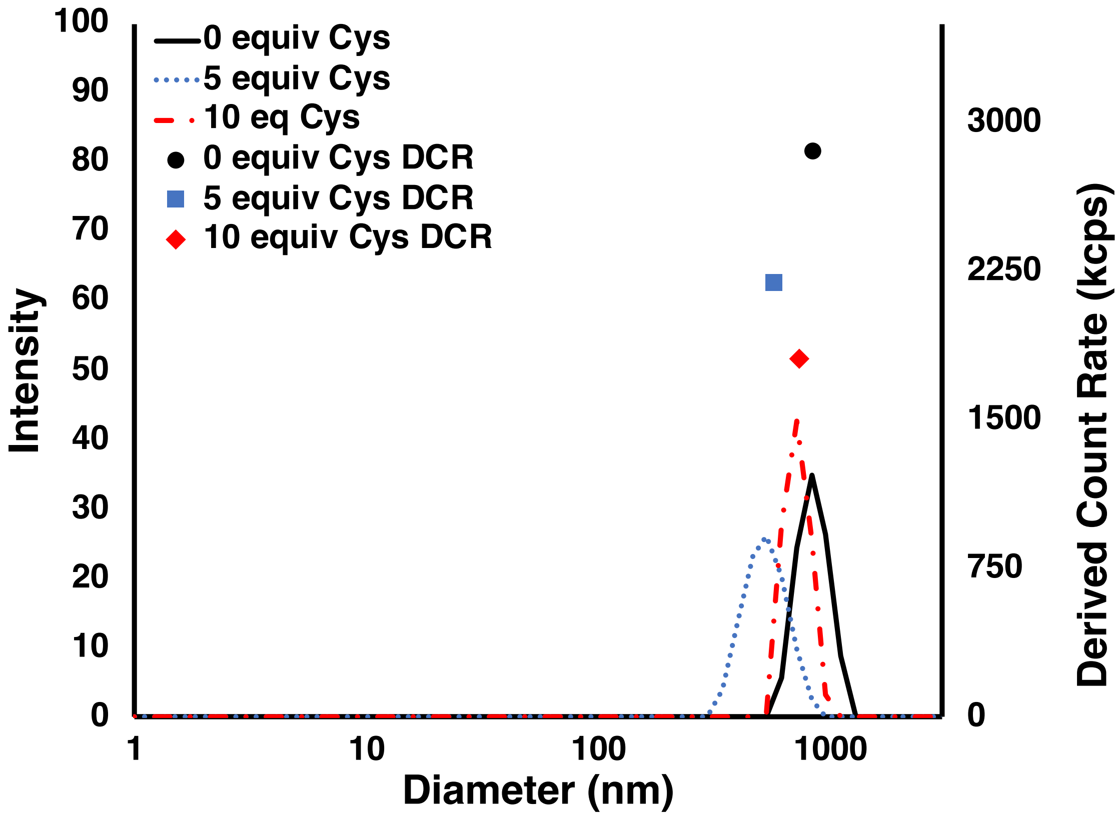

Figure S4.2. Complete scale of hydrodynamic ratio and derived count rate of 1mM of G-derivatives with 100 mM of KSCN in PBS, pH 7.4 at 37 °C after 90 minutes of varying equiv of Cys.

Table S4.1. DLS data of encapsulation and released

Sample	Time (min)	Cys (equiv)	Size (nm)	DCR (kcps)
f-SHS-fG	0	0	658	1145
f-SHS-fG@RhoB	0	0	2033	800
f-SHS-fG@RhoB	90	10	376	252

DCR: Derived count rate

4.6.2. NMR experiments

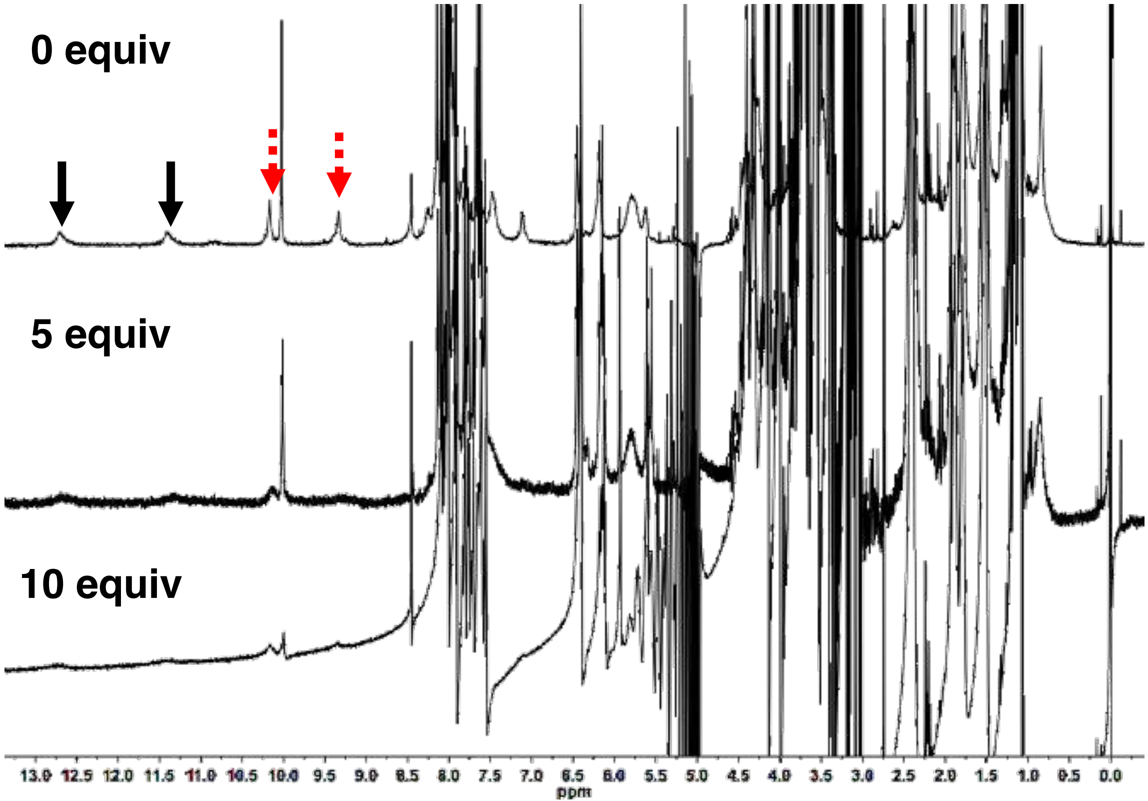

Figure S4.3. ^{1}H NMR (500 MHz) of **SGQ-fG** with varying amounts of Cys. N1H SGQ signals highlighted with solid line arrows and formyl moiety peaks highlighted using red dotted line arrows. Conditions: **fG** (1 mM) was dissolved in 100 mM of KSCN, in PBS, pH 7.4 with 2% D_2O at 5 °C; measurements were performed 90 min after adding Cys.

4.6.3. Turbidity experiments

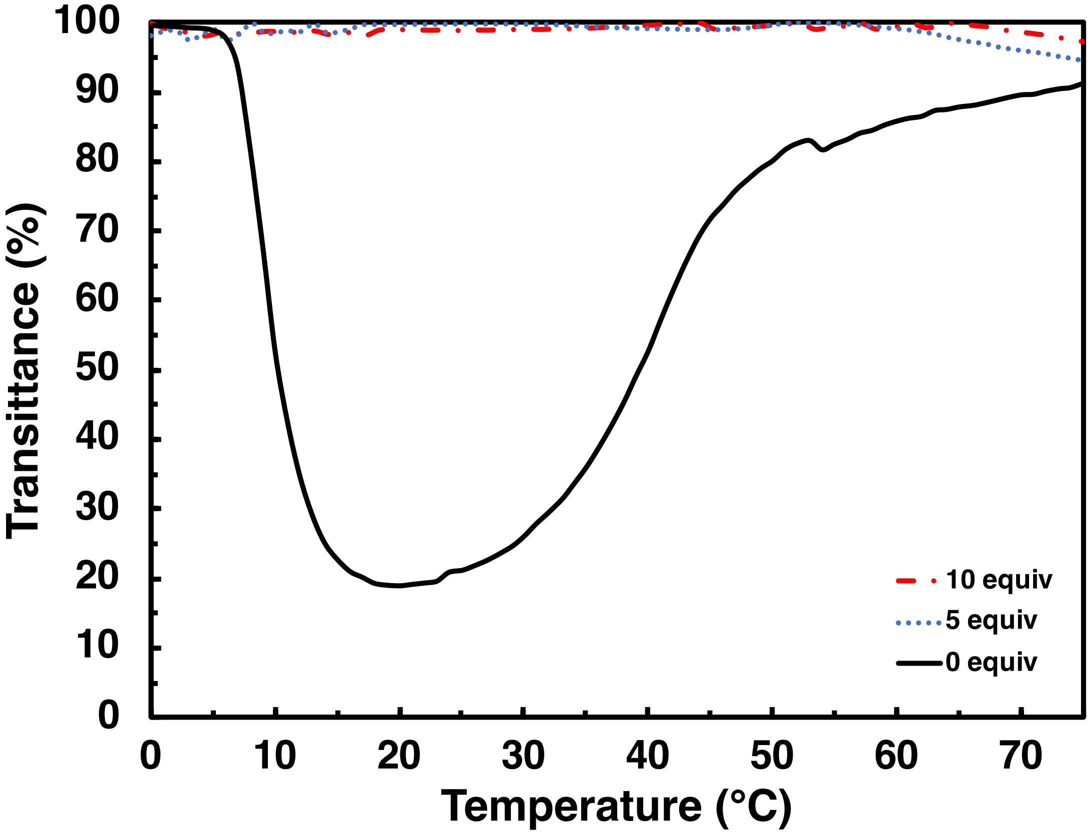

Figure S4.4. Turbidity as a function of temperature for solutions of **SGQ-fG** (1 mM in **fG**) after incubation (for 24 h) with different concentrations of Cys. Conditions: PBS, pH 7.4 containing KSCN (100 mM) and increasing amounts of cysteine as indicated by the legend.

4.6.4. Absorbance data

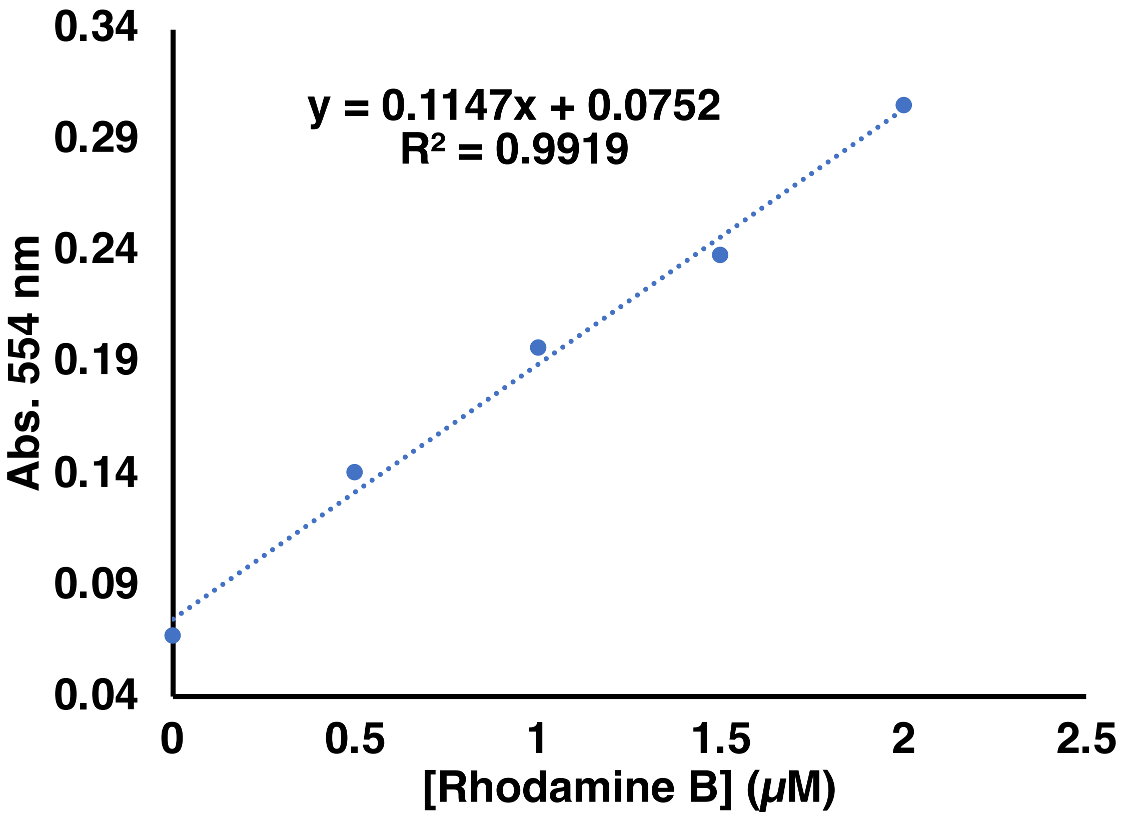

Figure S4.5. Calibration curve for Rhodamine B in PBS, pH 7.4 containing KSCN (100 mM) and cysteine (750 μM).

4.7. References

(1) Poole, L. B. The Basics of Thiols and Cysteines in Redox Biology and Chemistry. *Free Radic. Biol. Med.* **2015**, *80*, 148–157. https://doi.org/https://doi.org/10.1016/j.freeradbiomed.2014.11.013.

(2) Isokawa, M.; Kanamori, T.; Funatsu, T.; Tsunoda, M. Analytical Methods Involving Separation Techniques for Determination of Low-Molecular-Weight Biothiols in Human Plasma and Blood. *J. Chromatogr. B* **2014**, *964*, 103–115. https://doi.org/https://doi.org/10.1016/j.jchromb.2013.12.041.

(3) Hamley, I. W. The Amyloid Beta Peptide: A Chemist's Perspective. Role in Alzheimer's and Fibrillization. *Chem. Rev.* **2012**, *112* (10), 5147–5192. https://doi.org/10.1021/cr3000994.

(4) Borges-Santos, M. D.; Moreto, F.; Pereira, P. C. M.; Ming-Yu, Y.; Burini, R. C. Plasma Glutathione of HIV+ Patients Responded Positively and Differently to Dietary Supplementation with Cysteine or Glutamine. *Nutrition* **2012**, *28* (7), 753–756. https://doi.org/https://doi.org/10.1016/j.nut.2011.10.014.

(5) Tian, M.; Guo, F.; Sun, Y.; Zhang, W.; Miao, F.; Liu, Y.; Song, G.; Ho, C.-L.; Yu, X.; Sun, J. Z.; Wong, W.-Y. A Fluorescent Probe for Intracellular Cysteine Overcoming the Interference by Glutathione. *Org. Biomol. Chem.* **2014**, *12* (32), 6128–6133. https://doi.org/10.1039/C4OB00382A.

(6) Zhang, R.; Yong, J.; Yuan, J.; Ping Xu, Z. Recent Advances in the Development of Responsive Probes for Selective Detection of Cysteine. *Coord. Chem. Rev.* **2020**, *408*, 213182. https://doi.org/https://doi.org/10.1016/j.ccr.2020.213182.

(7) Tedja, R.; Soeriyadi, A. H.; Whittaker, M. R.; Lim, M.; Marquis, C.; Boyer, C.; Davis, T. P.; Amal, R. Effect of TiO2 Nanoparticle Surface Functionalization on Protein Adsorption, Cellular Uptake and Cytotoxicity: The Attachment of PEG Comb Polymers Using Catalytic Chain Transfer and Thiol–Ene Chemistry. *Polym. Chem.* **2012**, *3* (10), 2743. https://doi.org/10.1039/c2py20450a.

(8) Stuart, M. A. C.; Huck, W. T. S.; Genzer, J.; Müller, M.; Ober, C.; Stamm, M.; Sukhorukov, G. B.; Szleifer, I.; Tsukruk, V. V; Urban, M.; Winnik, F.; Zauscher, S.; Luzinov, I.; Minko, S. Emerging Applications of Stimuli-Responsive Polymer Materials. *Nat. Mater.* **2010**, *9* (2), 101–113. https://doi.org/10.1038/nmat2614.

(9) Schattling, P.; Jochum, F. D.; Theato, P. Multi-Stimuli Responsive Polymers - the All-in-One Talents. *Polym. Chem.* **2014**, *5* (1), 25–36. https://doi.org/10.1039/C3PY00880K.

(10) Fu, X.; Hosta-Rigau, L.; Chandrawati, R.; Cui, J. Multi-Stimuli-Responsive Polymer Particles, Films, and Hydrogels for Drug Delivery. *Chem* **2018**, *4* (9), 2084–2107. https://doi.org/https://doi.org/10.1016/j.chempr.2018.07.002.

(11) Cheng, R.; Meng, F.; Deng, C.; Klok, H.-A.; Zhong, Z. Dual and Multi-Stimuli Responsive Polymeric Nanoparticles for Programmed Site-Specific Drug Delivery. *Biomaterials* **2013**, *34* (14), 3647–3657. https://doi.org/https://doi.org/10.1016/j.biomaterials.2013.01.084.

(12) Cheng, R.; Feng, F.; Meng, F.; Deng, C.; Feijen, J.; Zhong, Z. Glutathione-Responsive Nano-Vehicles as a Promising Platform for Targeted Intracellular Drug and Gene Delivery. *J. Control. Release* **2011**, *152* (1), 2–12. https://doi.org/10.1016/j.jconrel.2011.01.030.

(13) Marino, S. M.; Gladyshev, V. N. Cysteine Function Governs Its Conservation and Degeneration and Restricts Its Utilization on Protein Surfaces. *J. Mol. Biol.* **2010**, *404* (5), 902–916. https://doi.org/10.1016/j.jmb.2010.09.027.

(14) Nair, D. P.; Podgórski, M.; Chatani, S.; Gong, T.; Xi, W.; Fenoli, C. R.; Bowman, C. N. The Thiol-Michael Addition Click Reaction: A Powerful and Widely Used Tool in Materials Chemistry. *Chem. Mater.* **2014**, *26* (1), 724–744. https://doi.org/10.1021/cm402180t.

(15) Lowe, A. B. Thiol-Ene “Click” Reactions and Recent Applications in Polymer and Materials Synthesis. *Polym. Chem.* **2010**, *1* (1), 17–36. https://doi.org/10.1039/B9PY00216B.

(16) Esterbauer, H.; Ertl, A.; Scholz, N. The Reaction of Cysteine with α,β-Unsaturated Aldehydes. *Tetrahedron* **1976**, *32* (2), 285–289. https://doi.org/10.1016/0040-4020(76)87015-9.

(17) Ratner, S.; Clarke, H. T. The Action of Formaldehyde upon Cysteine. *J. Am. Chem. Soc.* **1937**, *59* (1), 200–206. https://doi.org/10.1021/ja01280a050.

(18) Casi, G.; Huguenin-Dezot, N.; Zuberbühler, K.; Scheuermann, J.; Neri, D. Site-Specific Traceless Coupling of Potent Cytotoxic Drugs to Recombinant Antibodies for Pharmacodelivery. *J. Am. Chem. Soc.* **2012**, *134* (13), 5887–5892. https://doi.org/10.1021/ja211589m.

(19) Cai, Y.; Zhang, Y.; Yuan, W.; Yao, J.; Yan, G.; Lu, H. A Thiazolidine Formation-Based Approach for Ultrafast and Highly Efficient Solid-Phase Extraction of N-Glycoproteome. *Anal. Chim. Acta* **2020**, *1100*, 174–181. https://doi.org/https://doi.org/10.1016/j.aca.2019.12.001.

(20) Ma, Y.; Liu, S.; Yang, H.; Wu, Y.; Sun, H.; Wang, J.; Zhao, Q.; Li, F.; Huang, W. A Water-Soluble Phosphorescent Polymer for Time-Resolved Assay and Bioimaging of Cysteine/Homocysteine. *J. Mater. Chem. B* **2013**, *1* (3), 319–329. https://doi.org/10.1039/C2TB00259K.

(21) Duan, L.; Xu, Y.; Qian, X.; Wang, F.; Liu, J.; Cheng, T. Highly Selective Fluorescent Chemosensor with Red Shift for Cysteine in Buffer Solution and Its Bioimage: Symmetrical Naphthalimide Aldehyde. *Tetrahedron Lett.* **2008**, *49* (47), 6624–6627. https://doi.org/https://doi.org/10.1016/j.tetlet.2008.09.021.

(22) Poirel, A.; De Nicola, A.; Ziessel, R. Thiazolidine Derivatives from Fluorescent Dithienyl-BODIPY-Carboxaldehydes and Cysteine. *J. Org. Chem.* **2014**, *79* (23), 11463–11472. https://doi.org/10.1021/jo502068u.

(23) Ghobril, C.; Rodriguez, E. K.; Nazarian, A.; Grinstaff, M. W. Recent Advances in Dendritic Macromonomers for Hydrogel Formation and Their Medical Applications. *Biomacromolecules* **2016**, *17* (4), 1235–1252. https://doi.org/10.1021/acs.biomac.6b00004.

(24) Kubo, T.; Swartz, J. L.; Scheutz, G. M.; Sumerlin, B. S. Synthesis of Multifunctional Homopolymers through Using Thiazolidine Chemistry and Post-Polymerization Modification. *Macromol. Rapid Commun.* **2019**, *40* (1), 1800590. https://doi.org/10.1002/marc.201800590.

(25) Chen, Q.; Lv, Y.; Zhang, D.; Zhang, G.; Liu, C.; Zhu, D. Cysteine and PH-Responsive Hydrogel Based on a Saccharide Derivative with an Aldehyde Group. *Langmuir* **2010**, *26* (5), 3165–3168. https://doi.org/10.1021/la903102z.

(26) Yamada, Y.; Yoshida, C.; Hamada, K.; Kikkawa, Y.; Nomizu, M. Development of Three-Dimensional Cell Culture Scaffolds Using Laminin Peptide-Conjugated Agarose Microgels. *Biomacromolecules* **2020**, *21* (9), 3765–3771. https://doi.org/10.1021/acs.biomac.0c00871.

(27) García-Arriaga, M.; Acosta-Santiago, M.; Cruz, A.; Rivera-Rivera, J. M.; López, G. E.; Rivera, J. M. Probing the Limits of Supramolecular G-Quadruplexes Using Atomistic Molecular Dynamics Simulations. *Inorganica Chim. Acta* **2017**, *468* (Supplement C), 209–222. https://doi.org/https://doi.org/10.1016/j.ica.2017.08.051.

(28) Gubala, V.; Betancourt, J. E.; Rivera, J. M. Expanding the Hoogsteen Edge of 2‘-Deoxyguanosine: Consequences for G-Quadruplex Formation. *Org. Lett.* **2004**, *6* (25), 4735–4738. https://doi.org/10.1021/ol048013v.

(29) Negrón, L. M.; Díaz, T. L.; Ortiz-Quiles, E. O.; Dieppa-Matos, D.; Madera-Soto, B.; Rivera, J. M. Organic Nanoflowers from a Wide Variety of Molecules Templated by a Hierarchical Supramolecular Scaffold. *Langmuir* **2016**, 2283–2290. https://doi.org/10.1021/acs.langmuir.5b03946.

(30) Negrón, L. M.; Meléndez-Contés, Y.; Rivera, J. M. Patchy Supramolecules as Versatile Tools To Probe Hydrophobicity in Nanoglobular Systems. *J. Am. Chem. Soc.* **2013**, *135* (10), 3815–3817. https://doi.org/10.1021/ja401373h.

(31) Negrón, L. M. Synthesis and Characterization of Thermo/PH-Responsive Supramolecular G-Quadruplexes for the Construction of Supramolecular Hacky Sacks for Biorelevant Applications, University of Puerto Rico, Rio Piedras Campus, 2014.

(32) Gubala, V. Self-Assembly and Molecular Recognition of 8-Aryl-2’-Deoxyguanosine Analogues, University of Puerto Rico, Rio Piedras, 2006. https://doi.org/CN 547.7 G921S.

(33) Maestro. version 9. Schrödinger LLC: New York 2007.

(34) MacroModel. version 8. Schrödinger, LLC: New York 2007.

Chapter 5. Concluding remarks and outlook

In our endeavor, we aimed to produce more sophisticated biocompatible Supramolecular Hacky Sacks (SHS) particles for applications in biology as immune system applications. For this, we had to embark on different projects. To develop more biocompatible systems, we decided to explore the SHS particle formulations. We changed the formulations of the SHS particles by using a more chaotropic anion. We were able to decrease amount of salt added to the PBS buffer by a factor of 20 to assemble stable supramolecular G-quadruplexes. In the long term, we aim to self-assemble supramolecular systems with little or no salts added to the PBS. Yet, the simple change resulted in the thermal responsive properties' modulation lower critical solution temperature and studied of the SHS particle's upper critical solution temperature.

Here we got to explore the different intrinsic and extrinsic parameters in chapter 2. These changes resulted in the expansion of fundamental self-assembly parameters of supramolecular guanosine quadruplexes. These fundamental studies give the opportunity to further work in the restrictive parameters of biological conditions.[1–3] Usual particle formulation involves crosslinkers, non-biocompatible solvents.[2,4] Particle formulations may also include complex and not cost-effective procedures.[4] These issues lead to very few drug or vaccine formulations using particles.[1,2] Therefore, the expansion of the SHS library and simplification of formulations can shorten the gap for particles' future clinical use.

After expanding the SHS library, we focused on the responsive properties of the SHS particles already used as an HIV-1 vaccine adjuvant.[5] This exploration showed the successful responsiveness to biothiols. The intrinsic (i.e., structural) changes of the SHS particle building block included the α,β-unsaturated carbonyl, which participated in a thiol-Michael click reaction in chapter 3. Studies in chapter 3 revealed the controlled release of the encapsulated cargo in the presence of cysteine and glutathione at varying rates. We opened the door to explore this system even further for future biomedical applications. Taking what was earlier learned of thermal modulations, we applied it to expand on our biothiol responsive properties. This was done by using a formyl containing SHS particle's building block. These SHS particles were able to react with cysteine resulting in the formation of thiazolidine. This reaction resulted in the release of its non-covalently encapsulated cargo. By this, we furthermore expanded the different possible biological applications of the SHS particles.

The introduction of different biothiol responsive mechanisms furthers the endeavor to design supramolecular systems to address biomedical applications for cancer treatments or vaccine development.[6] Yet SHS have still a long way to go. We have already produced a biothiol reactive SHS used as a vaccine adjuvant.[5] Further studies of biothiol reactivity need to be addressed by including homocysteine. Competition studies based on the kinetics of biothiol reactive SHS with cysteine, homocysteine, and glutathione are required. These studies can help us understand which particle is suitable for each biothiol detection. Those studies will become the fundament for future controlled delivery systems. By having a deeper understanding of SHS reactivity, we can fine-tune the library to shorten the gap in the development of functional biocompatible particles for immune system modulation applications as vaccines.

5.1. References

(1) Anselmo, A. C.; Mitragotri, S. Nanoparticles in the Clinic. *Bioeng. Transl. Med.* **2016**, *1* (1), 10–29. https://doi.org/10.1002/btm2.10003.

(2) Hua, S.; de Matos, M. B. C.; Metselaar, J. M.; Storm, G. Current Trends and Challenges in the Clinical Translation of Nanoparticulate Nanomedicines: Pathways for Translational Development and Commercialization. *Front. Pharmacol.* **2018**, *9*. https://doi.org/10.3389/fphar.2018.00790.

(3) Wolfram, J.; Zhu, M.; Yang, Y.; Shen, J.; Gentile, E.; Paolino, D.; Fresta, M.; Nie, G.; Chen, C.; Shen, H.; Zhao, M. F. and Y. Safety of Nanoparticles in Medicine. *Current Drug Targets*. 2015, pp 1671–1681. https://doi.org/http://dx.doi.org/10.2174/1389450115666140804124808.

(4) Crucho, C. I. C.; Barros, M. T. Polymeric Nanoparticles: A Study on the Preparation Variables and Characterization Methods. *Mater. Sci. Eng. C* **2017**, *80*, 771–784. https://doi.org/https://doi.org/10.1016/j.msec.2017.06.004.

(5) Santos, S.; Ramírez, M.; Miranda, E.; Reyes, N.; Martínez, O.; Acosta-Santiago, M.; Rivera, J.; Otero, M. Enhancement of Immune Responses by Guanosine-Based Particles in DNA Plasmid Formulations against Infectious Diseases. *J. Immunol. Res.* **2019**, *2019*, 15. https://doi.org/10.1155/2019/3409371.

(6) Isokawa, M.; Kanamori, T.; Funatsu, T.; Tsunoda, M. Analytical Methods Involving Separation Techniques for Determination of Low-Molecular-Weight Biothiols in Human Plasma and Blood. *J. Chromatogr. B* **2014**, *964*, 103–115. https://doi.org/https://doi.org/10.1016/j.jchromb.2013.12.041.